R-06-88

T-H-M couplings in rock

Overview of results of importance to the SR-Can safety assessment

Harald Hökmark, Billy Fälth, Clay Technology AB

Thomas Wallroth, BERGAB

September 2006

Svensk Kärnbränslehantering AB
Swedish Nuclear Fuel
and Waste Management Co
Box 5864
SE-102 40 Stockholm Sweden
Tel 08-459 84 00
+46 8 459 84 00
Fax 08-661 57 19
+46 8 661 57 19

ISSN 1402-3091
SKB Rapport R-06-88

T-H-M couplings in rock

Overview of results of importance to the SR-Can safety assessment

Harald Hökmark, Billy Fälth, Clay Technology AB

Thomas Wallroth, BERGAB

September 2006

Abstract

This report deals with THM processes in rock hosting a KBS-3 nuclear waste repository. The issues addressed are mechanically and thermo-mechanically induced changes of the hydraulic conditions in the near-field and in the far-field, and the risk of stress-induced failure, spalling, in the walls of deposition holes. These changes are examined for the construction and operational phases, the initial temperate period and a subsequent glacial cycle.

The report was compiled to be used as reference and background for corresponding parts of the safety report SR-Can.

The near-field is analyzed using thermo-mechanical 3DEC models. There are a number of models for each of the three sites Forsmark, Simpevarp and Laxemar. Parameter values of intact rock and rock mass mechanical and thermo-mechanical properties were obtained from the site descriptive models. Layout data, i.e. the number of canisters, the geometry of the repository openings, the tunnel spacing and the canister spacing are in accordance with rules and guidelines given in general design- and layout documents. Heat generation data, i.e. the initial canister power and the canister power decay are in accordance with data given in the SR-Can main report.

The effects of changes in nearfield stresses during the different phases of the repository's life-time are evaluated by comparing numerically obtained stresses and deformations on a number of explicitly modelled near-field fractures with empirical and theoretical stress-transmissivity laws and with empirically based slip-transmissivity estimates. For the near-field it is concluded that substantial transmissivity increases are found only very close to the repository openings. Bounding estimates, judged to be valid for the entire load sequence, are made of the extent and magnitude of the hydraulic disturbance. At distances larger than about 1.5 m from the tunnel periphery, transmissivity increases are concluded to be too small and unsystematic to be of any concern.

The hydraulic significance of the Excavation Damaged Zone (EDZ) is assessed from experiences and observations made during different tunnelling projects at the Äspö Hard Rock laboratory and from conclusions of topical overviews. Previously, the general view was that an EDZ would form an independent and fast pathway along the drift. This is recognized to be an oversimplification. Rather, the EDZ is more likely to be discontinuous. In addition, it will be possible to reduce the damage by applying improved drill and blast procedures.

The impacts of heat generation and glacial load on the hydraulic conditions in the far-field are analyzed using results from large-scale 3DEC thermo-mechanical models and preliminary results from on-going simulations of the ice-crust-mantle interaction during the most recent glaciation.

Spalling in the walls of deposition holes as a result of excavation is concluded to be unlikely at all sites, but almost certain to occur after a few years of heating in dry deposition holes where the bentonite buffer has not taken up sufficient amounts of water to establish any support pressure.

There are many uncertainties. The most important one is probably that of the development of stresses and pore pressures at repository depth during a glacial cycle. The ice-crust-mantle interaction analyses used to calculate the stresses assumed in this report are based on an earth model that appears to be too simplistic for this particular purpose. New analyses, with more realistic earth models and with updated ice load data, are underway and will be used to revise the results given here. Also some of the stress-transmissivity relations are uncertain, in particular when it comes to estimating effects of deformations of large fractures.

Other uncertainties, for instance in site data such as the magnitudes and orientations of in situ stresses and rock properties data, are large but not larger than corresponding differences between the different sites, and do not appear to be of similar importance to the general conclusions.

Contents

1 Introduction and background

1.1 General

Mechanical and thermo-mechanical processes in the geosphere can potentially be important to performance and long-term safety. There can be direct mechanical damage to the canister/buffer system and there can be changes in the hydrological conditions, i.e. in the transmissivity of individual fractures and in the permeability of the rock mass.

Direct mechanical damage has been found to be an issue that is relevant only to earthquakes unless very large fractures, on the order of 700 m in diameter, are allowed to intersect canister positions. This has been demonstrated numerically for the thermal phase by /Hakami et al. 1998, Hakami and Olofsson 2002/ and for ice-loads by, for instance, /Rosengren and Stephansson 1990/ and /Hansson et al. 1995/. For all realistic static load cases, this follows from general relations between the size of a fracture and the maximum shear displacement /SKB 1999/. The problem of possible direct earthquake-induced canister damage is treated in specific reports (e.g. /La Pointe et al. 1999, Bäckblom and Munier 2002, Munier and Hökmark 2004, Fälth and Hökmark 2006a/). The present report relates to possible effects of mechanical and thermo-hydro-mechanical processes on the hydrological host rock conditions.

1.2 Thermo-hydro-mechanical evolution

The mechanical evolution of the repository host rock starts with the transition from the pre-mining undisturbed initial state to a state characterized by the mechanical impact of the excavation activities, i.e. formation of Excavation Disturbed Zones (EDZs), and by stress redistribution effects around the repository openings. The groundwater pressure will be reduced from an initial value of about 5 MPa to atmospheric at the peripheries of the openings. The pressure reduction will increase the effective normal stress acting across fractures and increase the fracture shear strength.

After deposition, backfilling and closure, the mechanical evolution is controlled by the heat generation from the spent fuel, by the swelling pressure of the bentonite buffer in the deposition holes and by the gradual restoration of the groundwater pressure, which will reduce the effective stress and the fracture shear strength. The timescale for the thermal effects can be predicted in detail as demonstrated in numerous analyses of the thermal development of the repository /Thunvik and Braester 1980, Probert and Claesson 1997a, Ageskog and Jansson 1999, Ikonen 2003, Hökmark and Claesson 2005/. The time-scale for the development of the swelling pressure depends on the local permeability conditions around the individual deposition holes and on the general repository-scale restoration of the groundwater pressure.

After the thermal pulse, when the host rock temperatures have returned to, or approach, the natural geothermal values, the continued mechanical evolution of the repository is controlled by climate variations with projected glaciation/deglaciation cycles and periods of permafrost. During periods of glaciation, tectonic stress may accumulate under the ice cover and add to the stresses caused by direct ice-load and by crust bending. The scope, extent, time-scale and duration of future loads are much more uncertain than the repository-driven thermal load. In addition to the mechanical effects of the ice loading and unloading, there will be changes in temperature and changes in groundwater pressure.

1.3 Relevant couplings

Figure 1-1 (left) shows the principles of THM couplings in a jointed rock mass. For the repository rock mass, the different interactions are not equally important.

/Löfman 2005/ simulated the disturbances caused by heat to the hydraulic conditions around the Olkiluoto repository in Finland. He concluded that after the closure of the tunnels, the temperature rise induces an increasing upward groundwater flow, which for hundreds of years delays the recovery of the flow conditions towards the natural state and raises the salinity of groundwater in the vicinity of the repository. These T-H simulations did not address the question of thermally or chemically induced long term effects on the host rock permeability. The thermal disturbance was significant, but of relatively short duration in the safety assessment time perspective. Buoyancy and convection do contribute to the water transport and to heat transport, but the contributions are small compared with the contributions from the natural isothermal groundwater flow and from conductive heat transport, respectively.

Similarly, the energy expended on, for instance, friction work is too small to have any measurable influence on the temperature. Figure 1-1 (right) shows the couplings considered in this report.

1.4 Scope

An overview of models for estimation of aperture and transmissivity changes caused by mechanical processes is given in Chapter 2. Different relations between stress changes and transmissivity are then used in subsequent chapters to evaluate excavation effects and future load effects on fractures intersecting the near-field, in particular fractures intersecting deposition holes (i.e. escape route Q1 fractures /SKB 2004a/, cf Figure 1-2).

Potentially important aspects of fracturing are the formation of an EDZ around tunnels and the possibility of spalling in the walls of deposition holes. An overview of EDZ work is given in Chapter 3. The axial permeability and the width together determine the transport capacity of escape route Q2 /SKB 2004a, cf Figure 1-2/. The potential for spalling is estimated in Chapter 6.

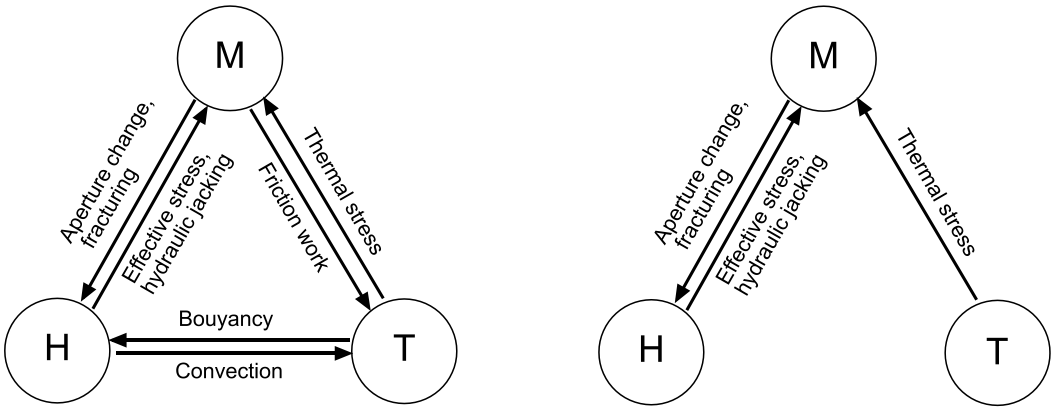

Figure 1-1. *Jointed rock mass THM couplings in general (left), and couplings relevant to the safety assessment (right).*

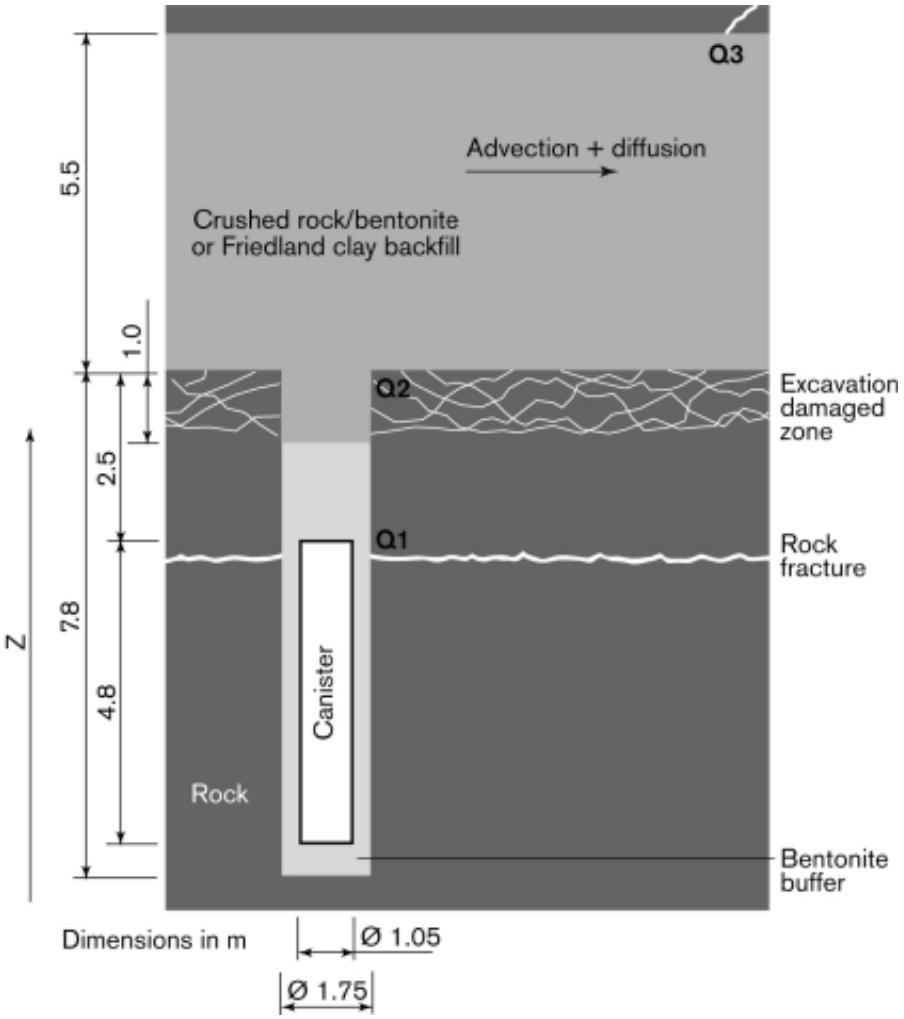

Figure 1-2. *Schematics of near-field with escape routes Q1, Q2 and Q3 (from /SKB 2004a/.*

The main body of the findings presented here is based on result of recent thermo-mechanical numerical analyses of 3DEC near-field Forsmark, Simpevarp and Laxemar site models. There are also corresponding, but more schematic, large-scale Forsmark site models. All 3DEC analyses are presented in detail in a separate report /Fälth and Hökmark 2006b/. Here the main features of the models are presented in Chapter 4. Examples of results are presented in Chapter 5 (effects on near-field permeability) and Chapter 6 (scope and extent of intact rock failure in the walls of deposition holes).

Thermal load effects and glacial load effects on the transmissivity of steeply dipping large-scale fractures are estimated in Chapter 7. For the thermal load, the estimate is based on the thermal stresses calculated by use of the Forsmark large-scale 3DEC model (and on stress-transmissivity relations derived from Chapter 2). For the glacial load cycle, the estimates are based on crust stress data obtained from ongoing ice-crust-mantle Finite Element Model (FEM) analyses. All transmissivity estimates are based on one-way M→H interactions.

The possibilities of two-way Hydro-Mechanical interactions, e.g. pore pressure driven deformations with consequent changes in permeability during glacial cycles, are discussed in Chapter 8. Conclusions from the study are presented in Chapter 9.

2 Models for estimating permeability changes

2.1 General

The host rock permeability depends on the geometrical properties of the fracture network and on the transmissivity of the individual fractures within the network. The EDZ's are primarily created during construction and are not part of the fracture networks described in the site models. Mechanically, thermo-mechanically and hydro-mechanically induced changes in the network geometry, in the transmissivity of individual fractures and in EDZ properties, may potentially change the host rock permeability.

The EDZ permeability is strongly dependent on the tunnelling method. No future loads are likely to have effects similar to the drill and blast damage done during the excavation. Future loads will cause additional disturbances, but without extensive additional fracturing, meaning that their relative effects are small. Therefore values of EDZ permeabilities relevant for input in hydro-models do not have to change because of the mechanical evolution after excavation. Estimates of fixed values, based on case studies of tunnelling experiments will be adequate (see following chapter).

The geometry of the fracture networks, as described by site-specific Discrete Fracture Network (DFN) models, i.e. the fracture frequency, the size and orientation of individual fractures and the connectivity between individual fractures, may theoretically change because of fracture propagation and coalescence when the rock stresses change as a result of mechanical and thermo-mechanical loads. Fracture propagation and coalescence may occur close to the openings, but require high stress levels and high values of the major/minor remote principal stress ratio σ_1/σ_3. /Shen and Stephansson 1996/ analyzed effects of a number of loading events using the Displacement Discontinuity Method and found propagation and coalescence close to tunnels and deposition holes only if that stress ratio was 400% or larger, i.e. if $\sigma_1/\sigma_3 \geq 4$. The local and modest changes of the fracture network geometry found in their study are too small to be of importance to the DFN models and to the overall rock mass permeability.

The existing fractures will be subject to small or large stress changes during the different loading events. In addition to formation of EDZ's, the effects on existing fractures, i.e. transmissivity changes because of normal and shear displacements, are likely to be the main mechanisms by which the present-day hydrological conditions in the host rock may change.

2.2 Effects on single fractures

2.2.1 Normal displacements

When the normal stress on an individual fracture changes as a result of loading or un-loading of the rock containing the fracture, the hydraulic aperture will change, leading to decreased or increased transmissivity of the individual fracture. Stress-deformation relations are non-linear with stiffnesses that increase sharply with increasing compression /Goodman 1976, Bandis 1980/. Two independent models are presented below.

Stripa granite fractures; continuously-yielding joint model

Figure 2-1 shows a fit of stress-stiffness data, derived from results given by /Vik and Barton 1988/ to the power law used in the continuously-yielding joint model /Itasca 2003/.

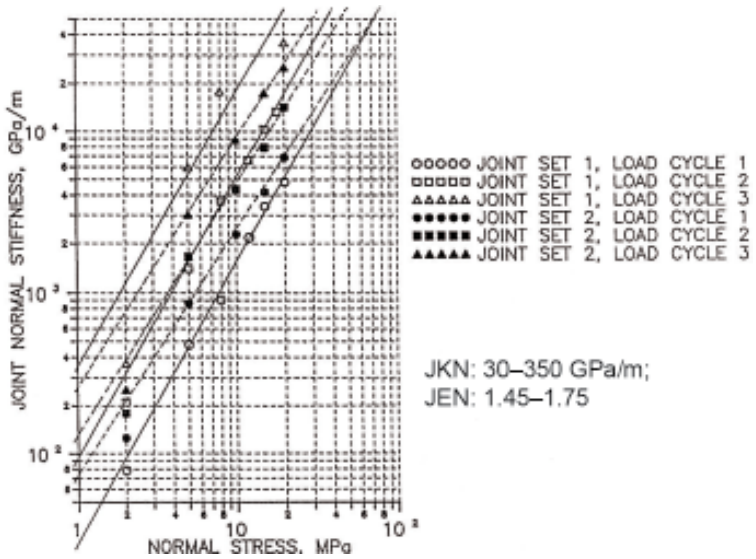

Figure 2-1. *Discrete plot symbols show data derived from /Vik and Barton 1988/, who determined parameter values of Barton-Bandis joint model for two sets of Stripa granite joints and generated stress-displacement relations by use of that model. The straight lines are fits of Equation 2-1 to the results. JEN is obtained as the slope of the straight lines and JKN as the intercept with the vertical axis. From /Hökmark 1990/.*

$$K_n = JKN\sigma_n^{JEN} \tag{2-1}$$

Here, K_n is the joint normal stiffness, σ_n the joint normal stress, and *JKN* and *JEN* model parameters. The continuously-yielding joint model simulates continuous weakening behaviour as a function of accumulated plastic shear displacement. Equation 2-1 describes the joint normal behaviour in that model.

If the initial aperture at the normal stress σ_0 is u_0, then Equation 2-1 gives the aperture u at stress σ as:

$$u = u_0 - \frac{1}{JKN}\int_{\sigma_0}^{\sigma} \sigma'^{-JEN} d\sigma' \tag{2-2}$$

This mechanical model does not address any relations between hydraulic and mechanical apertures. The calculated mechanical joint closure/opening should be added to the assumed initial hydraulic aperture to find the resulting hydraulic aperture. For purely normal loading/unloading conditions this is probably a good approximation (a similar assumption is made in the stress-aperture model presented in the following section). If u_0 is the value assumed for the undisturbed hydraulic aperture at stress σ_0, then u is the hydraulic aperture at stress σ. (For shear loading, relations between mechanical and hydraulic apertures are more complicated).

Sellafield fractures; empirical law

/Liu et al. 2003/ fitted aperture – stress measurements made on Sellafield rock joint samples by

$$b = b_r + b_m = b_r + b_{\max} \exp(-\alpha'\sigma) \tag{2-3}$$

Here, b is the total hydraulic aperture, b_r the residual aperture, b_m the mechanical aperture and b_{max} the maximum mechanical aperture. σ is the normal stress acting across the fracture and α is a model parameter. Figure 2-2 shows examples of the Sellafield relations.

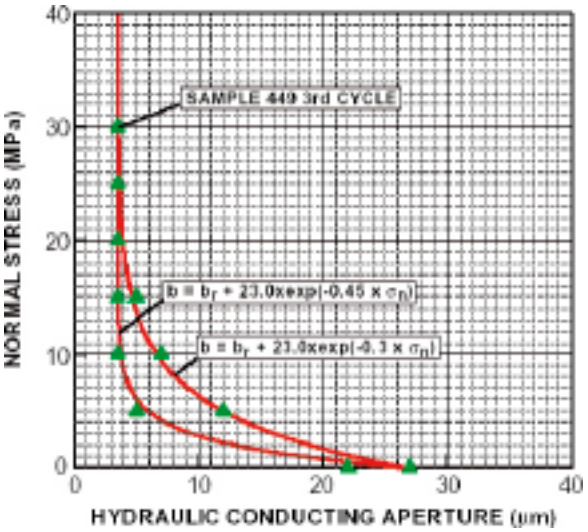

Figure 2-2. *Stress-aperture relations. From /Liu et al. 2003/.*

Stress-aperture law comparison

Figure 2-3 shows stress-aperture relations for both models for two assumptions regarding the residual aperture b_r and the initial aperture u_0. For the CY model (Stripa) the initial stress was set at 10 MPa.

2.2.2 Shear displacements

During fracture shear movements, the mechanical aperture will change due to dilation, i.e. the two fracture surfaces are forced to separate because of surface irregularities. Dilation is not an easily calculated quantity. Depending on the magnitude of the normal stress and on the joint wall strength, asperities can be sheared through or overridden. A compilation of models and concepts relevant to the problem of normal deformations and aperture changes during shear is given by /Olsson 1998/. Equation 2-4 below, for instance, is an approximation of the peak dilation angle d_n suggested by /Barton and Choubey 1977/ to be valid at low normal stresses.

$$d_n = JRC \cdot \log(JCS / \sigma_n) \qquad (2\text{-}4)$$

Here, σ_n is the joint normal stress. *JRC* is the Joint Roughness Coefficient and *JCS* the effective Joint wall Compressive Strength (see e.g. /Barton and Choubey 1977, Bandis et al. 1983/). Here, "low normal stress" relates to the value of *JCS*. For *Ävrö granite* fractures, /Olsson 1998/ found that the equation reproduced peak dilation angles measured at normal stresses of 2–4 MPa.

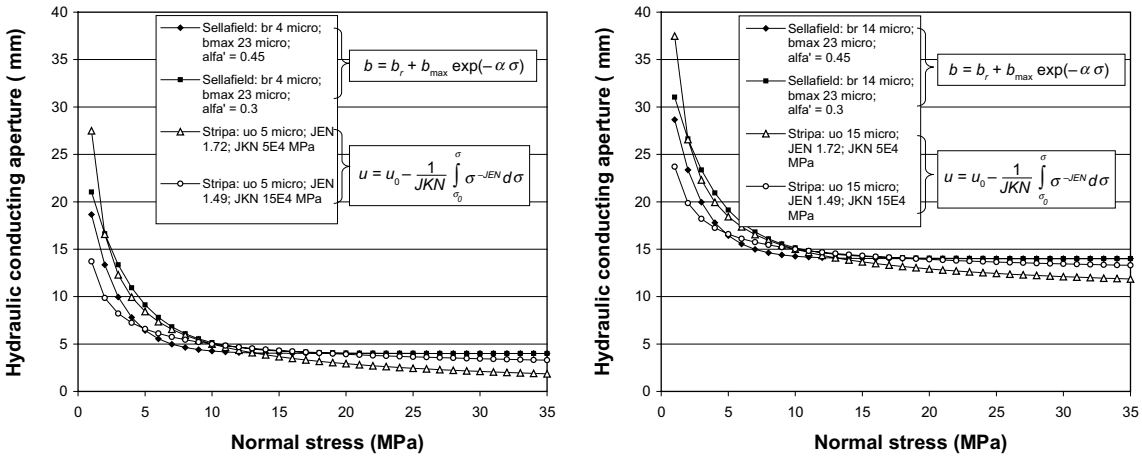

Figure 2-3*. Stress-aperture relations.*

Figure 2-4 shows results of actual mechanical closure-opening measurements performed in shear box experiments on joint samples of *Ävrö granite* /Olsson 1998/. The hydraulic apertures, calculated from actual flow measurements, are shown along with the mechanical results. Note that an increase in mechanical opening of about 0.7 mm results in 0.3 mm increase in hydraulic aperture in this shear test. This is in contrast to the behaviour described for normal loading/unloading in the previous section.

The shear tests pictured in Figure 2-4 were conducted under constant stiffness with a low (2 MPa) initial normal load.

2.2.3 Single fracture transmissivities

Behaviour under normal stress variations

Figure 2-5 shows relative transmissivities T/T_0 for fractures obeying the stress-aperture laws described above and assuming the cubic flow law to apply, i.e.:

$$T / T_0 = (\alpha / \alpha_0)^3 \tag{2-5}$$

For the absolute transmissivity T, the cubic flow law reads:

$$T = \frac{\rho g}{12\mu} a^3, \tag{2-6}$$

where g is the gravitational acceleration, ρ the fluid density, μ the dynamic viscosity of the fluid and a the hydraulic aperture. For a fracture of 5 µm hydraulic aperture this gives a transmissivity of $1 \cdot 10^{-10}$ m²/s and for a 15 µm fracture 2.8 10^{-9} m²/s. Note that the highly transmissive 15 µm fracture is much less sensitive to stress changes than the 5 µm aperture fracture.

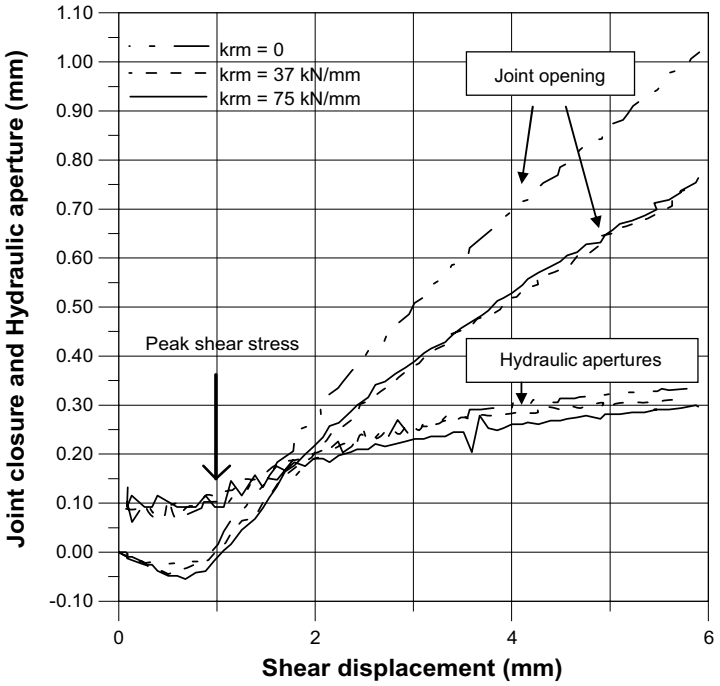

Figure 2-4. *Left: Measured mechanical displacements (openings) and calculated hydraulic apertures. Constant stiffness values were 0 GPa/m, 1 GPa/m and 2 GPa/m, respectively for the three experiments (spring constants krm 0, 37 and 75 kN/mm). From /Olsson 1998/.*

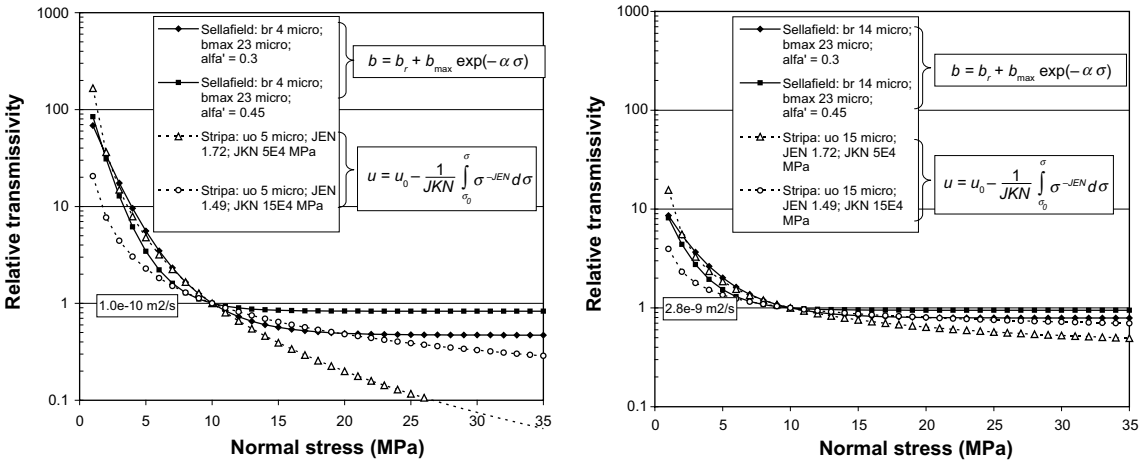

Figure 2-5. *Relative fracture transmissivities for two cases of the residual, or initial, aperture. Both stress-aperture models described above are included.*

The transmissivity results above are based on stress-aperture laws and on the cubic flow law. The hydraulic aperture is assumed to change by an amount given by the mechanical joint closure/separation. For real fractures this is not necessarily true. /Barton 1982/ suggested that the ratio between mechanical and hydraulic apertures depends on the Joint Roughness Coefficient (*JRC*). For high values of *JRC*, the increase in hydraulic aperture, and the transmissivity increase, would be less than suggested in Figure 2-5. Figure 2-6 shows empirical relations between the mechanical aperture *E* and the hydraulic smooth wall aperture *e*.

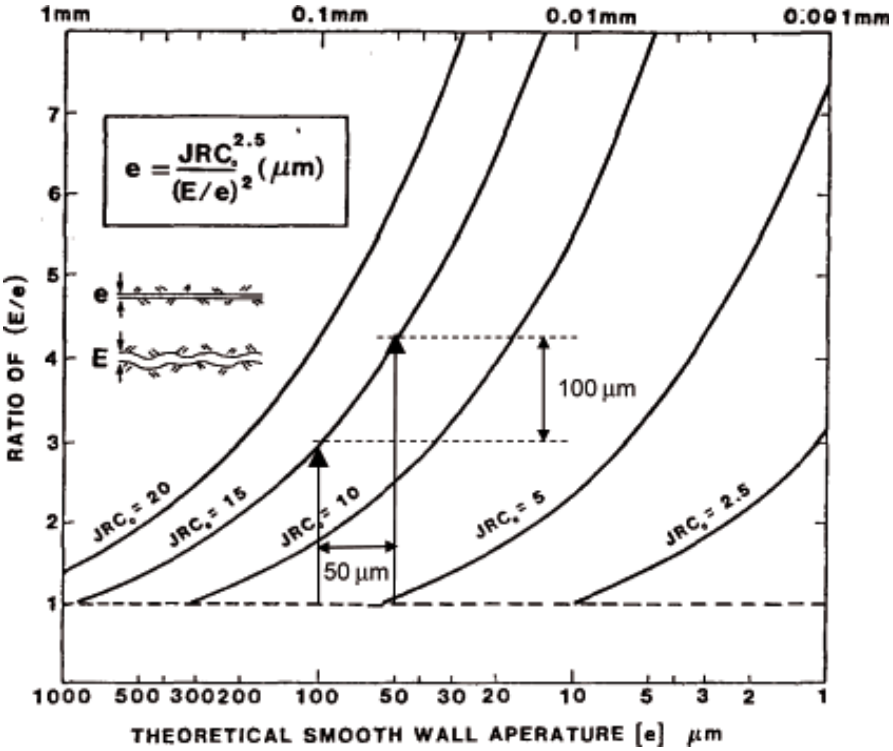

Figure 2-6. *Empirical relation between aperture ratio E/e and smooth wall aperture e for different values of the Joint Roughness Coefficient JRC. For the example indicated by the arrows, a 50 mm increase in hydraulic aperture would require a mechanical opening of approximately 100 µm. Based on figure from /Barton 1992/.*

Equation 2-7 below is a direct, empirical stress-transmissivity law proposed by /Raven and Gale 1985/ and /Derschowitz et al. 1991/.

$$T / T_0 = (\sigma / \sigma_0)^{-\beta} \qquad (2\text{-}7)$$

T and T_0 are the transmissivities at normal stresses σ and σ_0, respectively, and β is a model parameter. For rock joints samples of Stripa granite, /Dershowitz et al. 1991/ found that $\beta = 1$ would reproduce the measured results reasonably well. Figure 2-7 shows relative transmissivities calculated by use of Equation 2-7 compared with results from the two stress-aperture relations described above (assuming the cubic flow law to apply). For the two models based on aperture changes and the cubic flow law, the absolute transmissivity at the point of departure (10 MPa of normal stress, cf Figure 2-5) is $1 \cdot 10^{-10}$ m^2/s in the left figure and 2.8 10^{-9} m^2/s in the right one.

In following sections, the Sellafield model is used as reference. The other models are not conditioned for large stress increases and are likely to overpredict joint closure and overestimate transmissivity reductions. For low normal stresses, i.e. for normal stress relaxations, the three types of relations give similar results, provided that reasonable parameter values are chosen.

For the stress-transmissivity models tried here, Figure 2-7 shows that the fracture normal stress must drop below 3–4 MPa for the transmissivity to increase by more than one order of magnitude.

Figure 2-7 also points to the importance of the residual, or initial, aperture. For high-transmissivity fractures, the sensitivity to stress changes is less than for less important low-transmissivity fractures. In the following chapters a value of 10 µm, corresponding to a residual or initial transmissivity of $8 \cdot 10^{-10}$ m^2/s is used as reference.

Note that the above relations were developed to account for effects of normal stress variations without explicit account of the true nature of fracture flow, i.e. without account of, for instance, aperture variations, flow channels and effects of mineralization. These concepts are important for a physically correct description of fracture flow and the way solutes are transported (cf e.g. /SKB 2001/). For the purpose of this study, i.e. to make order-of-magnitude estimates of effects of significant normal stress variations on fracture transmissivities, the type of relations pictured in Figure 2-7 are judged to be sufficient.

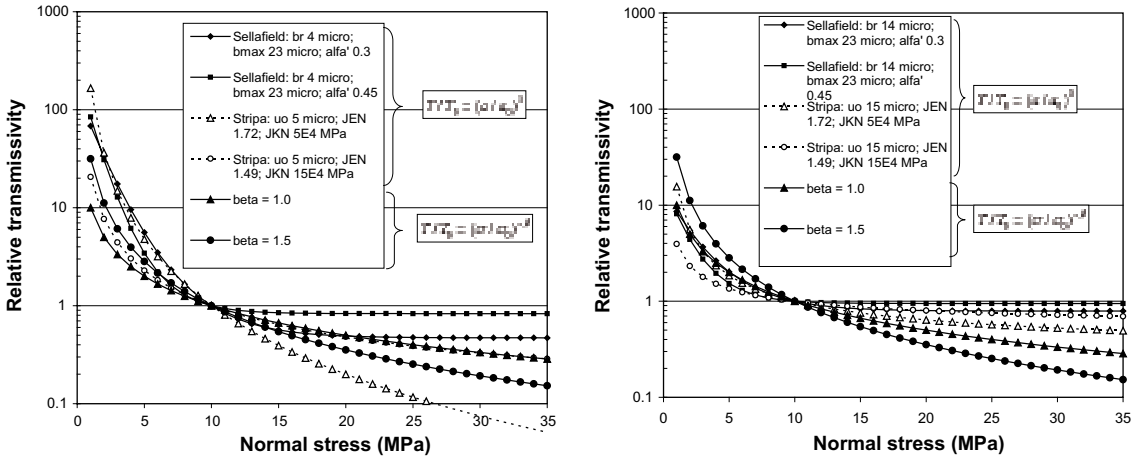

Figure 2-7. *Stress-transmissivity relations obtained from the three stress-transmissivity models described in the text.*

Behaviour under shear deformations

For shear movements, changes in transmissivity are determined not only by changes in the mechanical apertures, but also by possible gouge production. For high normal stresses, there will be more asperity damage and less dilation. Figure 2-8 shows results of hydro-mechanical constant stiffness shear tests performed on samples of *Ävrö granite* fractures /Olsson 1998/.

There are two sets of results: one for 2 MPa of initial normal stress and one for 4 MPa. For the tests conducted at 4 MPa of initial normal stress, it took between 3 and 4 mm of shear displacement to arrive at any significant transmissivity increase, whereas the 2 MPa tests all showed transmissivity increases after one mm of shear displacement. For the 4 MPa experiment, the transmissivity increased by a factor of about 20 after 5 mm of shear displacement and by two orders of magnitude after 15 mm.

It is difficult to estimate corresponding transmissivity effects of shear displacements that take place at significantly higher normal stresses. Increasing the normal stress from 2 MPa to 4 MPa appeared to suppress the increase in transmissivity very efficiently. At a distance of a few metres from the repository openings, effective normal stresses will be even larger: typically 10 MPa or more (cf Chapter 5). The dilation, or mechanical joint separation, will be less than for low-stress fractures (such as those examined by /Olsson 1998/, cf Figure 2-4) and the gouge production will influence the flow conditions such that the resulting effective transmissivity increase is likely to be very modest. Close to the repository openings where normal stresses may be low, at least locally, shear displacements exceeding about 4 mm may result in local transmissivity increases of between one and two orders of magnitude.

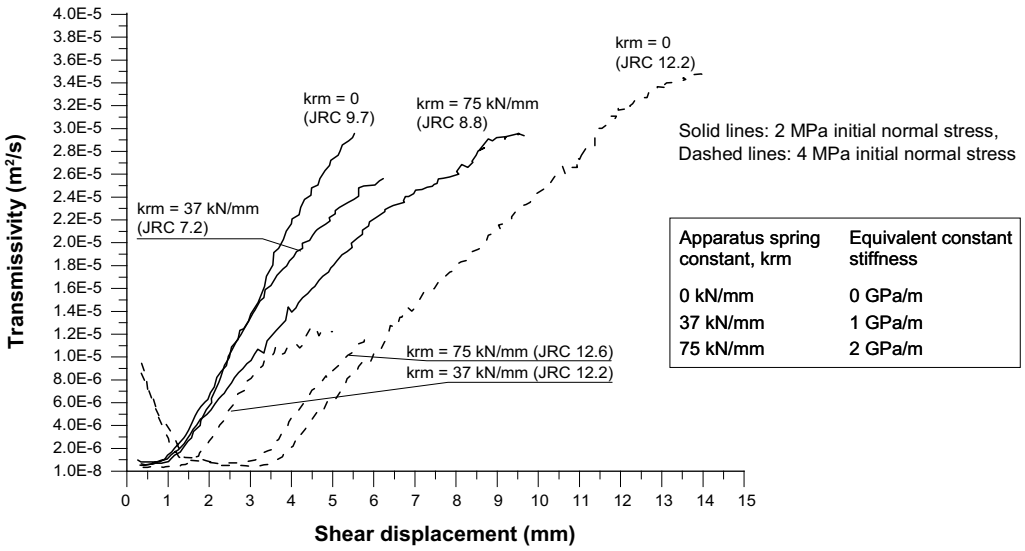

Figure 2-8. *Measured transmissivities of Ävrö granite fractures as function of shear displacement. The hydro-mechanical shear tests were conducted under different normal stiffnesses. From /Olsson 1998/.*

3 EDZ

3.1 General

The possibility that the damage done to the rock during excavation will result in zones of increased axial permeability has long been considered. The question has been addressed in topical overviews, e.g. /Winberg 1991, Tsang et al. 2005/, and in various conceptual studies /Pusch, 1990, Pusch and Stanfors 1992/. The Zone of Excavation Disturbance Experiment (ZEDEX) conducted at the 420 m level in the Äspö HRL was specifically designed to compare drill and blast damage with damage found in a nearby and parallel tunnel excavated with a tunnel boring machine /Emsley et al. 1997/. This experiment was conducted to examine the integrated effects of disturbances caused by stress redistribution and direct excavation damage, whereas the EDZ definition used here relates only to direct damage. Stress redistribution effects, which will always be found independently of the excavation method, are treated separately in Chapter 5.

For the safety analysis, the issue is to estimate the width of the EDZ and assign relevant hydraulic properties to it.

In addition to the important question of the permeability conditions in the EDZ, there are also mechanical aspects to consider, i.e. the possibility of stress relaxation and changed mechanical properties. Below the tunnel floor, for instance, the EDZ may limit the development of stress concentrations around the upper parts of deposition holes and contribute to reducing the risk and extent of stress-induced failure (cf Chapter 6).

3.2 Previous work

/Case and Kelsall 1987/ proposed a model for modification of the permeability around shafts in welded tuff based on case histories of blast damage in tunnels in different rock types. The model considered the combined effects of stress redistribution and blast damage. Blast damage was assumed to increase the fracture frequency by a factor of three, while stress redistribution effects were estimated from stress-permeability relationships obtained from combinations of results from laboratory and field tests. For the most conservative set of assumptions regarding in situ stresses, rock strength and depth of damage, the axial permeability was increased by a factor of 80 in a 1.0 m wide annular zone around a 4.4 m diameter shaft.

/Winberg 1991/ suggested that the axial EDZ hydraulic conductivity should be as high 10^{-6} m/s in the floor and roof regions and about 10^{-8} m/s in the walls for drill and blast tunnels. The zone width should be between 0.1 m and 1 m, depending on the site conditions and on the drill and blast technique.

/Pusch 1990/ and /Pusch and Stanfors 1992/ suggested similar models, i.e. with axial conductivities of around 10^{-8} m/s in about 1 m wide zones around the peripheries of drill and blast tunnels.

In a more recent topical overview, /Tsang et al. 2005/ summarized key processes, parameters and technical issues for different rock types including crystalline rocks, rock salt, indurated clays and plastic clays. The overview was a synthesis of issues emerged at the European Commission EDZ CLUSTER conference /EC 2004/. For the excavation damage in crystalline rock, they suggested permeability increases of between 2 and 3 orders of magnitude and zone thicknesses between 0.1 m and 1.5 m. Contrary to the other rock type EDZ's, crystalline rock EDZ's should be considered to be mechanically stable, i.e. rock creep would not be a concern. As for the safety assessment aspect, Tsang et al. concluded that the assumption that the presence of an EDZ provides a fast radionuclide escape route is now recognized to be an

oversimplification. The EDZ permeability may be relatively high, but an evaluation of the total flow system is required to find out whether flow can take advantage of it to transport solutes to the environment. Tsang et al. did not explicitly address the question of the EDZ continuity along the drift or the significance of the backfill permeability. They pointed to different possibilities of improving the repository performance, for instance by optimizing the excavation methods (cf TASQ tunnelling experience below) or by installing seals and EDZ cut-offs.

3.3 Experience from ZEDEX

The ZEDEX experiment was conducted particularly to examine the integrated effects of disturbances caused by stress redistribution and direct excavation damage. Two nearby and parallel tunnels were used for the study. One of the tunnels was excavated with different drill and blast techniques (D&B), while the other one was excavated mechanically with a tunnel boring machine (TBM).

The main evaluation method was analysis of Acoustic Emission data (AE). Also different seismic techniques and micro-crack analysis of rock samples and dye penetration tests were used. As expected, the depth of damage was found to be much less in the TBM tunnel (about 0.03 m) than in the D&B tunnel (0.3 m in the roof and wall regions and 0.8 m in the floor). Also the nature of the damage was different in the two tunnels. In the TBM tunnel, there was modest induced micro-fracturing, whereas there was evidence of induced macro-cracks in the D&B tunnel. The majority of the AE events were, however, concluded to fit shear-slip mechanisms on existing cracks. Much of the direct damage found in the D&B tunnel was concluded to be caused by misfires and reblasting required for failed rounds /Emsley et al. 1997/ and consequently of local extent.

The evaluation of the ZEDEX experiment did not include direct measurements of the axial conductivity of the damaged zone, meaning that there would still be a lack of knowledge when it comes to the question of assigning relevant values in hydrological models to be used in the safety analysis. Local permeability increases were found, but these could not be shown to represent values relevant along a continuous zone of connected rock fractures. They may rather have been the result of fractures (pre-existing or created during excavation) connecting to the open tunnel. /Emsley et al. 1997/ consequently concluded that evidence supporting the hypothesis of significantly increased permeability along the drift was still limited, and that this issue remained to be solved. Emsley et al. also noted that direct and accurate field-scale permeability measurements, relevant for finding tunnel-scale EDZ axial permeability values, are difficult because of flow transients and because of uncertainties in boundary conditions and in the state of saturation. A final conclusion was that, since its hydraulic significance in the large scale depends on the interaction with the backfilled tunnel, it may not be meaningful to assign conductivity values to the EDZ as a pathway of its own.

3.4 TASQ tunnel

The TASQ tunnel at ÄSPÖ HRL was excavated specifically to accommodate the Äspö Pillar Stability Experiment (APSE). This experiment required well-defined conditions in the floor region with a minimum of excavation damage. The D&B technique used for the excavation included a number of procedures to limit the extent of the EDZ /Olsson et al. 2004/. Excavation with top and bench separately, for instance (cf Figure 3-1), meant that smaller specific charges could be used for the floor contour holes.

By distributing the specific charge along the individual rounds it was possible to separate regions of induced cracks, such that the resulting EDZ was discontinuous in the axial direction. Figure 3-2 shows the EDZ as observed in a slot sawed in the tunnel wall.

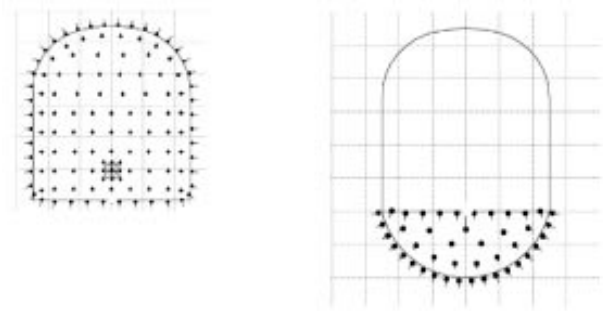

Figure 3-1. *TASQ tunnel with separate excavation of top (left) and bench (right).*

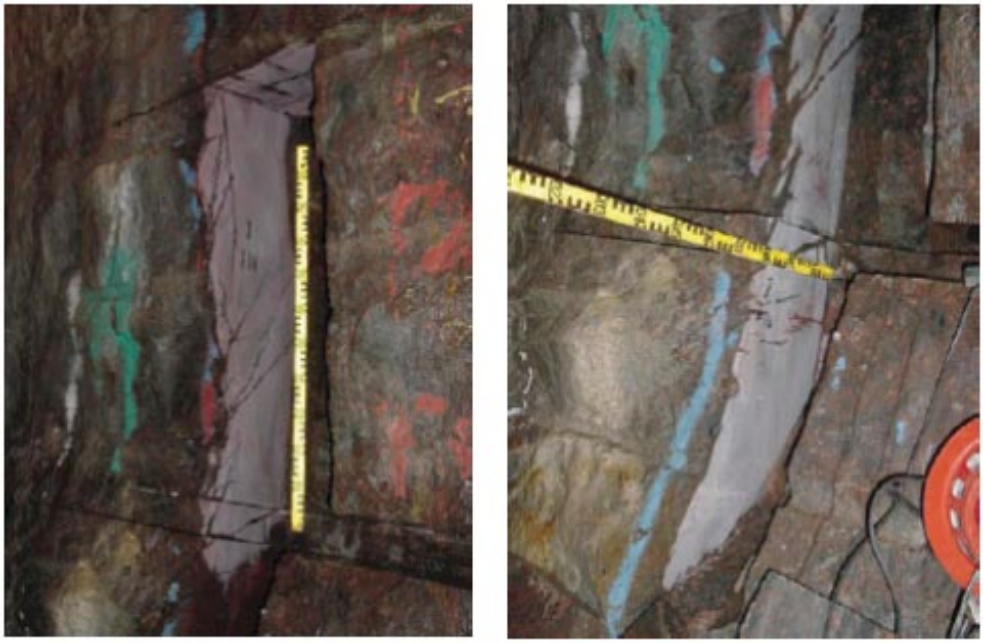

Figure 3-2. *TASQ tunnel EDZ as observed in slot sawed in the left tunnel wall. Left: wall above bench. Right: bench.*

Several conclusions were drawn, including the following:

- Excavating the deposition tunnel in two steps, first a top heading and then the bottom bench, gives significantly less damage in the floor compared with ZEDEX experience; even less than in the roof and walls. This is primarily caused by the difference in the specific charge in the contour holes for the floor. However, further development in blast design is needed to enable similar results to be achieved in terms of a small EDZ in the floor without excavation of a separate bench.
- For "typical" tunnel construction, based on current Swedish practice, the observed excavation damage is similar to that observed in the ZEDEX D&B tunnel.
- The look-out angle and the distribution of specific charge along each round (with more charge in the end of the round) cause the EDZ to be discontinuous along the tunnel. It is therefore concluded that the impact of the EDZ on hydraulic conductivity along the tunnel is very small, because it is manageable through D&B design and Quality Assurance control during excavation.

- The reasons for local significantly larger extension of the EDZ are well understood. They are most likely manageable in a systematic QA program during excavation. To implement appropriate quality plans and ensure their application in the execution of a tunneling project may require special care and training.

A general conclusion drawn by /Olsson et al. 2004/ after evaluation of the TASQ tunnel D&B experience is that the technique can be applied in regular tunnel production, provided that proper QA procedures are established and followed. However, the notion of a hydraulically discontinuous EDZ is not particular to the TASQ tunnelling experience, but a general observation based on the way look-out angles and specific charge distribution influence the crack pattern in regular D&B practice. Figure 3-3 illustrates some of the concepts.

3.5 Hydraulic properties of EDZ in the repository

The actual permeability effects of the damage done during excavation, the relative permeability increase as well as the zone thickness, will depend not only on details in the D&B technique but also on stresses, rock properties, tunnel orientation, existing fracture network, anisotropy etc. Although a high level of understanding of all processes and features is required for confidence, as concluded by /Tsang et al. 2005/, a full scientific evaluation of all conditions is not necessary for the performance assessment. The performance assessment can be based on bounding estimates, scoping calculations and sensitivity analyses without accounting for all details.

Early studies (e.g. /Winberg 1991, Pusch 1990, Pusch and Stanfors 1992/) pointed to the possibility of a substantially increased permeability in the axial direction and suggested that the EDZ would act as an important pathway, possibly short-circuiting the tunnel backfill. The ZEDEX and the TASQ observations and conclusions seem, however, to support the view expressed in /Tsang et al. 2005/, i.e. that this may be an oversimplification.

In summary it can be concluded that the hydraulic significance of the EDZ will vary along the tunnel, depending on the local EDZ permeability and on features of the total flow system (for instance the permeability of the tunnel backfill).

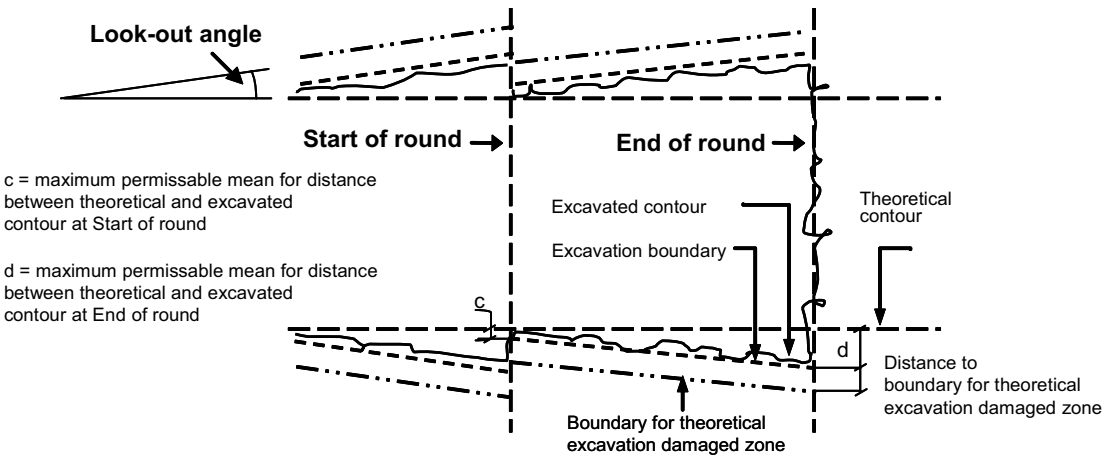

Figure 3-3. *Illustration of some D&B concepts (based on figure from /Bäckblom et al. 2004/).*

For handling of the permeability aspects of the EDZ in the safety assessment, the following bounding cases should be considered:

- Tunnels are excavated with the intent of limiting the EDZ, i.e. using the drill and blast techniques and the QA procedures described in /Olsson et al. 2004/. In this case, the EDZ is likely to be limited in spatial extent and discontinuous. The axial permeability may increase by half an order of magnitude in a zone of 0.3 m radial thickness. There will be 0.5 m breaks of undamaged rock between each blast round, due to uneven charge distribution in the blast design. However, in the flow modeling, the EDZ is cautiously assumed to be continuous, but of low permeability.
- A limiting case is to assume conventional drill-and-blast of the tunnel, without applying any special QA procedures for controlling the EDZ and without account of discontinuities caused by look-out angles and specific charge distribution. The permeability increases by two orders of magnitude in a region corresponding to the zone of damage found in the ZEDEX experiment, i.e. 0.3 m in the roof and walls and 0.8 m in the floor.

4 3DEC analyses

4.1 Near-field model outlines

/Fälth and Hökmark 2006b/ analyzed the near-field of a KBS-3 repository in Forsmark, Simpevarp and Laxemar thermo-mechanically. The design and layout were in accordance with the rules laid down by SKB /SKB 2002, 2004b/. Figure 4-1 (left) shows details of the Forsmark and Simpevarp models. With respect to canister spacing, the Laxemar model is intermediate between the Forsmark and Simpevarp models. Figure 4-2 shows the model outlines.

The canister spacing was set with respect to the predicted mean thermal conductivity. For the Simpevarp and Forsmark models, the spacing values were determined during early stages of the layout work (R Glamheden, FB Engineering AB, personal communication, 2004, M Brantberger, Ramböll Sverige AB, personal communication, 2004), and may differ from the values given in the Layout D1 reports /SKB 2006c, Brantberger et al. 2006/. The spacing defined in the models is, however, consistent with the assumed heat conductivity as prescribed in the general design rules /SKB 2004b/. For the Laxemar model the value was taken from the Layout D1 report /Jansson et al. 2006/.

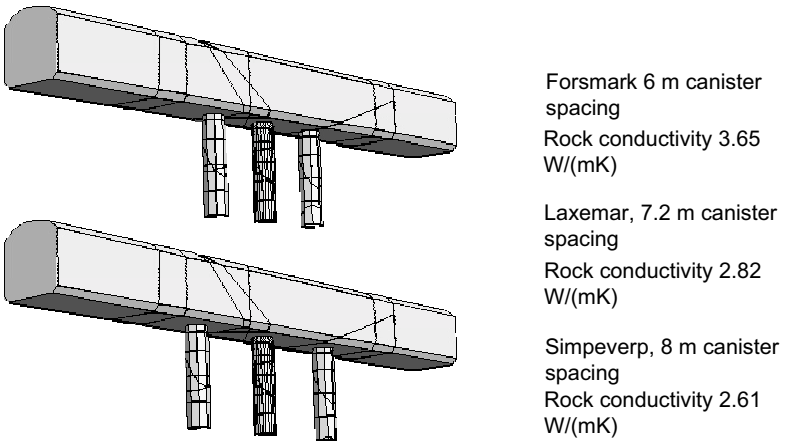

Figure 4-1. *3DEC near-field models: excavated volumes.*

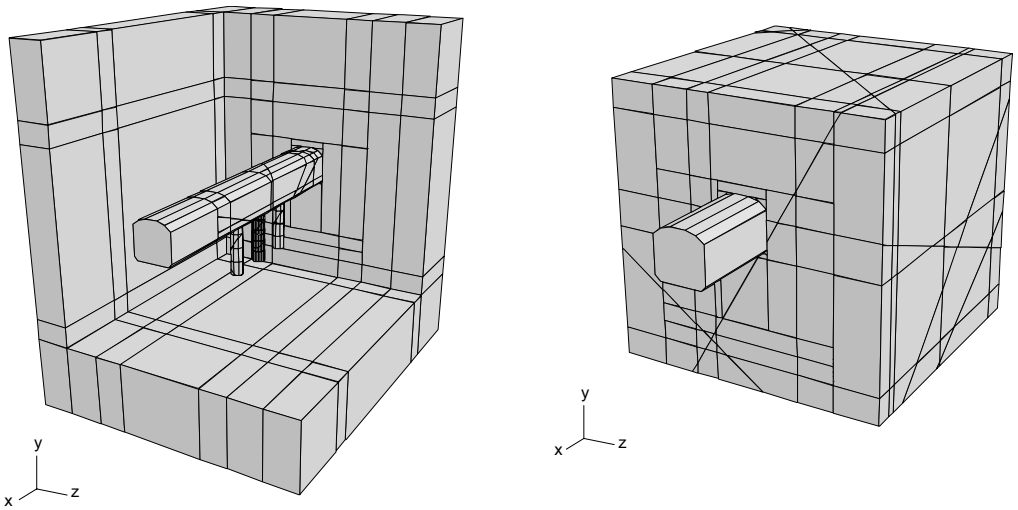

Figure 4-2. *Geometry of mechanical 3DEC model. 3DEC left-hand coordinate system is arranged with the x-axis along the tunnel and the y–axis vertical.*

4.2 Heat generation

The 3DEC near-field models were subjected to thermal loads. Figure 4-3 (left) shows the general KBS-3 repository layout /SKB 2002/ with the tunnel section being analyzed in the 3DEC near-field models located in the central parts. When site adapting the repository during construction the deposition areas may have to be split into subunits because of intersecting fracture zones, but for the 3DEC numerical analyses presented here, the schematic layout was used without modifications. The right part of Figure 4-3 shows the heat generation geometry schematically in a horizontal section through the repository. In 3DEC thermal models, temperatures are calculated analytically, approximating all heat transport to be linear conduction in an isotropic and homogenous medium. This means that 3DEC heat sources do not need to be contained within the rock volume that is analyzed mechanically. In each of the grey rectangles there is grid of heat sources, each representing a canister of 1,700 W of initial heat power and with decay characteristics of 30–40 year old SKB fuel. In total, there are 4,756 canisters.

Figure 4-4 (left) shows the source grid in the vicinity of the mechanical near-field model with different ways of representing nearby and distant heat sources /Hökmark and Fälth 2003/. Canisters are represented by point sources, vertical line sources or compound line sources, depending on the proximity to the region of interest, i.e. the centre of the near-field model.

The compound source (central canister only) consists of two superimposed, differently sized line sources. By calibrating the strength and the length of the two line sources making up the compound source, it is possible to reproduce the heat flow distribution along the height of a real, cylindrical canister realistically /Hökmark and Fälth 2003/. There is more heat output per unit source length in the top and bottom parts (and less at mid-height) than for the simple line source representation. However, the difference does not mean more than a couple of degrees at canister mid-height.

Figure 4-4 (right) shows the decay function /Hökmark and Fälth 2003/.

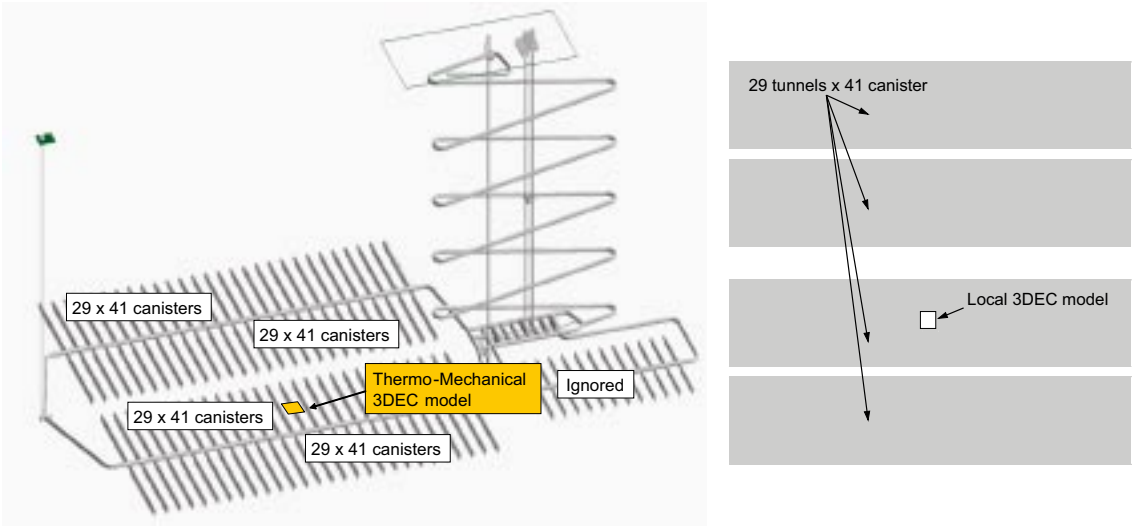

Figure 4-3. *Left: Repository layout. Right: Horizontal section.*

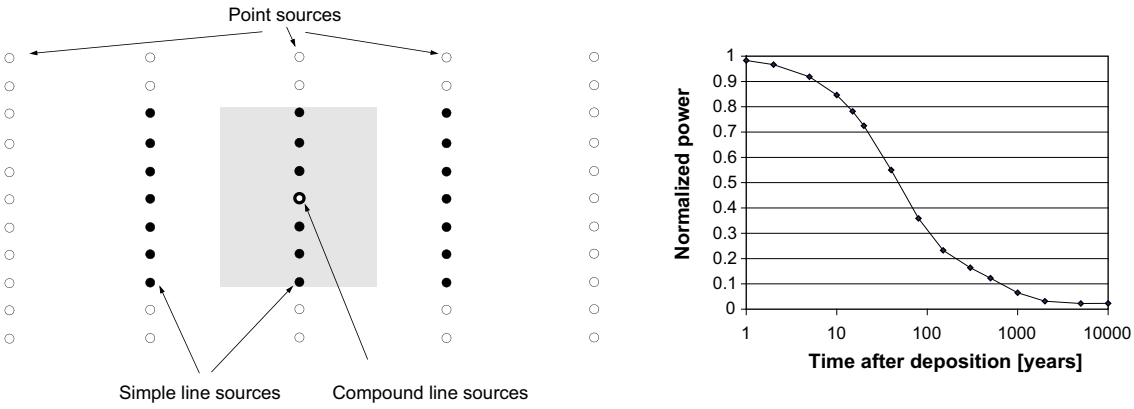

Figure 4-4. *Heat generation. Grid of sources (left) and decay function (right).*

4.3 Input data

Site data, i.e. values of the initial pre-excavation stresses, values of intact rock properties, rock mass properties and fracture properties were obtained or determined at different stages of the development of version 1.2 of the site models. Some of the data will have been modified during the course of the site investigations. The input data are compiled in the SR-Can data report /SKB 2006d/.

4.3.1 Initial stresses

The site-descriptive models give one stress state for the Forsmark site and two each for Laxemar and Simpevarp /SKB 2005ab, 2006a/. For all stress states given in the site descriptions, one principal stress dips 90 degrees, i.e. is aligned with the 3DEC y-axis. There are 3DEC models for both Simpevarp stress domains. Simpevarp Domain 2 is a low-stress domain, where tunnels are perpendicular to the major stress (R Glamheden, FB Engineering AB, personal communication, 2004). In the Forsmark and Simpevarp Domain 1 preliminary layout solutions, tunnels are aligned up to 15 degrees off from the major horizontal stress. (M Brantberger, Ramböll Sverige AB, personal communication, 2004, R Glamheden, FB Engineering AB, personal communication, 2004). In the Laxemar layout, tunnel directions differ between deposition areas /Jansson et al. 2006/. In the Laxemar 3DEC model, the angle between tunnel and major stress orientation is 63 degrees.

Table 4-1 shows the stress magnitudes and the stress orientations assumed in the different 3DEC models. Because of updates and revisions made to the site models, the Forsmark model was analyzed for two different initial stress assumptions:

- Base case at 500 m depth with draft site model value of minor horizontal stress.
- Update at 400 m depth with final site model value /SKB 2005b/ of minor horizontal stress.

The Forsmark base case stresses are given for 500 m depth, applying stress-depth relations given in draft versions of the Forsmark site report. The stress update concerns 400 m depth, applying stress-depth relations given in the final v. 1.2 report /SKB 2005b/.

Table 4-1. Principal stress magnitudes (MPa) and orientation of horizontal stresses.

Forsmark			Simpevarp 1			Simpevarp 2			Laxemar		
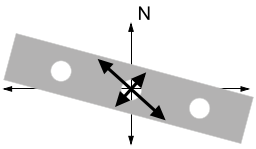			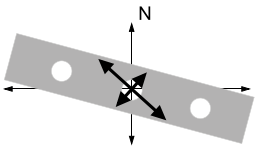			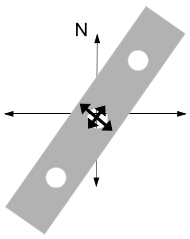			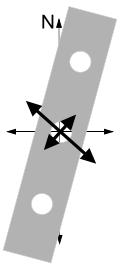		
σ_H	σ_h	σ_v	σ_H	σ_h	σ_v	σ_H	σ_h	σ_v	σ_H	σ_h	σ_v
45	18	13	32	9.5	14	16	5.5	9	34	10	13.5
43*	29*	11*									

*) Stress update.

4.3.2 Fracture system

The fracture system was specified without any real link to the sites. Instead, a small number of fractures intersecting the near-field at different angles and at different positions in relation to the central part of the model were defined (Figure 4-5). All cuts seen in the 3DEC block plots other than the 6 explicitly described fractures correspond to mechanically (and thermally) invisible construction planes. These are used to define the geometry and to facilitate the discretization of the continuum between fractures.

All fractures extend to the boundaries of the inner 30 m × 30 m × 30 m cube. The fracture geometry is identical in all models analyzed here and given relative to the geometry of the tunnel and the central deposition hole, irrespective of the canister spacing and the tunnel orientation.

There are Discrete Fracture Network (DFN) models that describe the fracture system at the sites statistically /SKB 2005ab, 2006a/, but it is not possible to analyze sufficiently many different realizations of the statistical models with 3DEC to make meaningful and general interpretations. For the purpose of the 3DEC near-field study /Fälth and Hökmark 2006b/, i.e. to evaluate the effects of different fracture locations and orientations, it has been deemed expedient to consider a small number of well-defined schematic fractures, identical in all model versions.

Table 4-2. Fractures.

Fracture	Orientation and location
#1	Vertical and perpendicular to tunnel, at 0.4 m distance from the wall of the central deposition hole.
#2	Vertical and parallel to tunnel at 0.75 m distance from the tunnel wall.
#3	Vertical, intersecting tunnel at 45° at 0.54 m distance from the wall of the central deposition hole.
#4	Dipping 20° with strike normal to tunnel.
#5	Dipping 45° with strike normal to tunnel.
#6	Dipping 45° with strike 45° relative to tunnel.

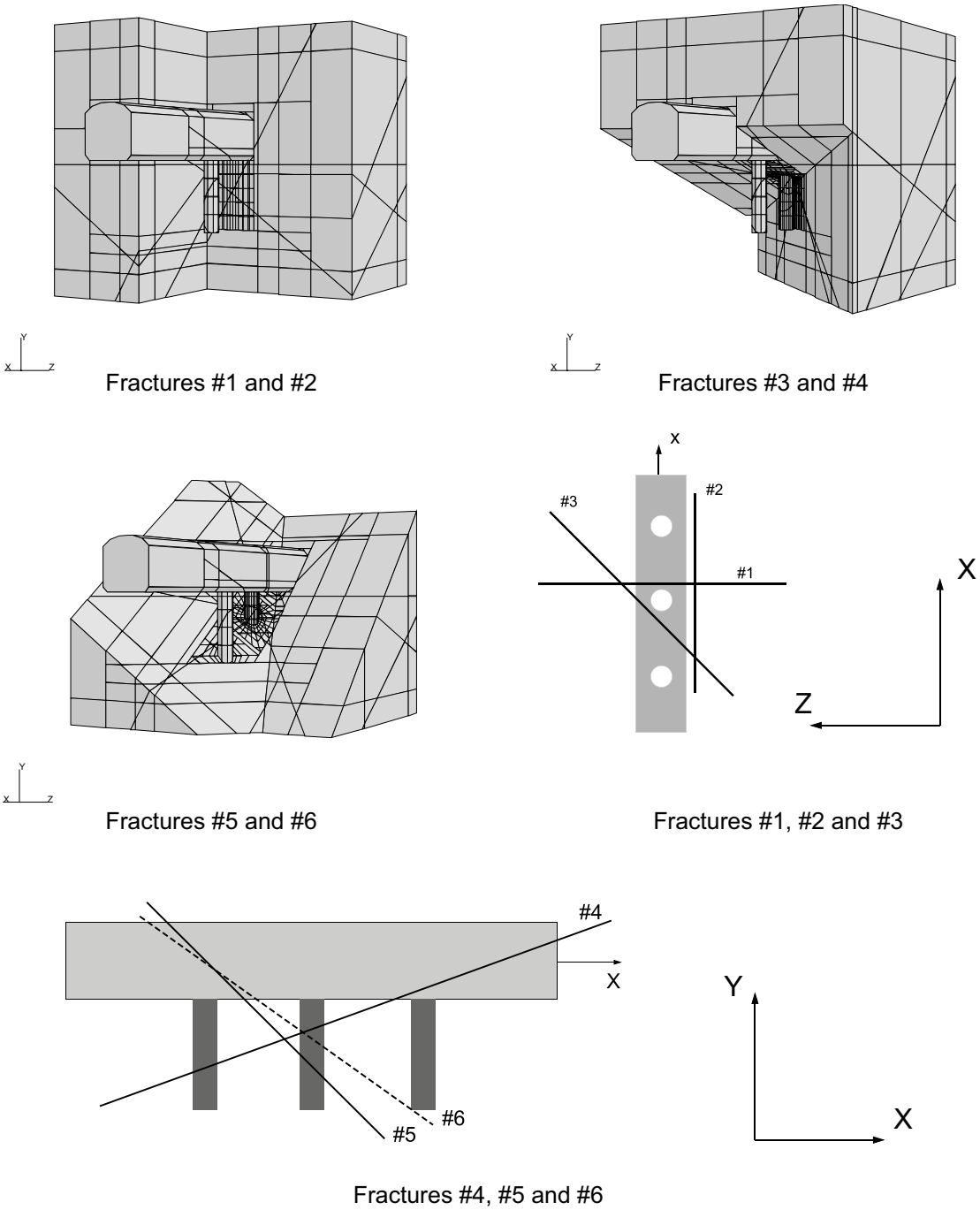

Figure 4-5. *Fractures in inner box. All fractures extend to the box boundaries.*

4.3.3 Material properties

The material parameter values assumed in the different models are shown in Table 4-3. Most input values agree with corresponding data in the site reports, while there are differences for a few; see the notes following the table.

Table 4-3. Base case parameter values.

Component	3DEC parameter	Unit	Forsmark	Simpevarp	Laxemar	Note
Intact rock	Density	kg/m^3	2,600			1
	Young's modulus	GPa	76	80	70	2
	Poisson's ratio	–	0.24	0.27	0.20	2
	Heat conductivity	W/(mK)	3.65	2.61	2.82	3
	Heat diffusivity	m^2/s	$1.75*10^{-6}$	$1.25*10^{-6}$	$1.36*10^{-6}$	3
	Heat expansion coefficient	K^{-1}	$7.7*10^{-6}$	$6.2*10^{-6}$	$7.2*10^{-6}$	4
Fractures	Joint normal stiffness	GPa/m	128	100	220	5
	Joint shear stiffness,	GPa/m	39	29	40	5
	Friction angle	deg	34			6
	Cohesion	MPa	0.6			6
	Dilation angle	deg	10			7
Rock mass	Young's modulus	GPa	68	62	55	8
	Poisson's ratio	–	0.22	0.28	0.28	8

1) Approximate and generic value used in all models.

2) Ver. 1.2 site model data. Values given for rock type *"granite to granodiorite"* (Forsmark), "*quartz monzonite to monzodiorite and Ävrö granite"* (Simpevarp) and "*granite to quartz monzodiorite (Ävrö granite)"* (Laxemar).

3) Values of heat conductivity (Forsmark and Simpevarp models) were obtained from early deliveries of site data to preliminary design projects (R Glamheden, FB Engineering AB, personal communication, 2004, M Brantberger, Ramböll Sverige AB, personal communication, 2004). These data were used to set the canister spacing in pilot layout work and have been kept in the 3DEC models. However, the thermal site models have been updated such that the RFM012 domain mean value is 3.46 W/(mK) rather than 3.65 W/(m·K) /Sundberg et al. 2005b/ and the RSMA01 value is 2.80 W/(m·K) rather than 2.61 W/(m·K) /Sundberg et al. 2005a/. The thermal diffusivities are calculated from generic values of density (2,600 kg/m^3) and specific heat (800 J/(kg·K)). These values correspond to a volumetric heat capacity of 2.08 MJ/m^3, whereas the RFM012 and RSMA01 mean values are 2.15 MJ/m^3 and 2.23 MJ/m^3, respectively /Sundberg et al. 2005ab/. The Laxemar value, which relates to rock domain RMSA, was taken from the Laxemar layout D1 report /Jansson et al. 2006/

4) Values of heat expansion coefficient (Forsmark and Simpevarp) were obtained from draft site model versions. For the Forsmark model, this value agrees with the one given for *granite to granodiorite* and, on the domain level, for domains RFM012 and RFM029 in /SKB 2005b/. For the Simpevarp model, the value now given for *Ävrö granite* is $6.0 \cdot 10^{-6}$ K^{-1}. /SKB 2005a/. For Laxemar, the value relates to *granite to quartz monzodiorite* /SKB 2006a/.

5) Ver. 1.2 site model data. In the site models, there are no differences between fractures belonging to different fracture sets or different domains within the sites. In the 3DEC models mean values are used throughout. For the normal stiffness, the site reports give min-max ranges of 60–230 GPa/m (Forsmark), 49–179 GPa/m (Simpevarp) and 150–310 GPa/m (Laxemar). For the shear stiffness, corresponding ranges are 10–55 GPa/m, 10–49 GPa/m and 18–66 GPa/m, respectively.

6) Values of Coulomb parameters given here are approximated from data in the site reports. As with the stiffness values, the given strength data are not differentiated with regard to borehole or joint set. The data given for the three sites are sufficiently similar that the same (averaged) parameter values are used for all sites.

7) Draft versions of the Forsmark and Simpevarp site reports (and the borehole primary data reports) did not include any values of the dilation angle. For the Simpevarp subarea, there are no values in the final version /SKB 2005a/. Previous investigations of *Ävrö granite* rock joints have indicated that the dilation angle should be about 10 degrees or more /Olsson 1998/, which justifies the value used in the 3DEC models for all sites (cf Figure 4-6). The values now given for the Forsmark and Laxemar areas range between 4° (for fractures in high compression) and 19.5° and 16°, respectively (for fractures in low compression) /SKB 2005b, 2006a/.

8) Ver. 1.2 site model data. Values given for rock domain RFM012 (Forsmark), rock domain A (Simpevarp) and rock domain A (Laxemar).

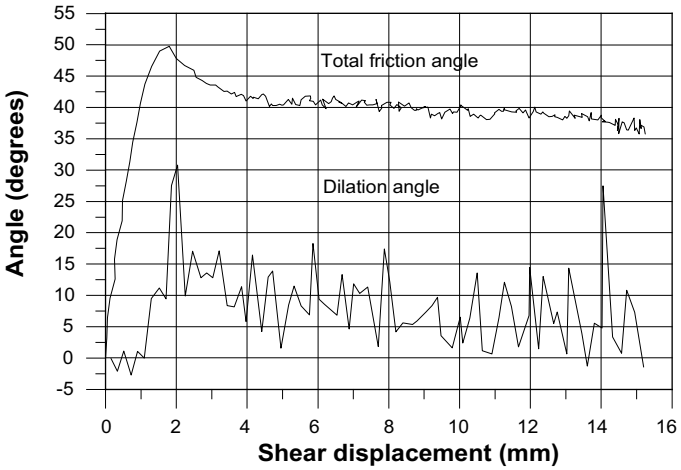

Figure 4-6. *Result of constant, 4 MPa, normal load shear test on Ävrö granite fracture /from Olsson 1998/.*

4.4 Simulation sequences

The simulations included the following:

1. Excavation of tunnel
2. Excavation of deposition holes
3. Development of swelling pressure in the deposition holes
4. Development of pore pressure
5. Thermal load from 4,756 canisters, each generating 1,700 kW of thermal power at the time of deposition and with decay function as specified for SKB reference fuel.
6. Mechanical effects of glacial load with boundary stresses obtained from preliminary results from simulations of mechanical ice-crust-mantle interactions.

The above disturbances were applied in sequence although in reality there will be some overlapping, in particular between 3), 4) and 5). All models, Forsmark, Simpevarp and Laxemar, were analyzed in a number of different versions, (e.g. with and without account of swelling and pore pressure). Item 6, glaciation, was applied only to the Forsmark model. A complete and detailed description of all models and model versions is given in /Fälth and Hökmark 2006b/.

4.5 Large-scale models

Figure 4-7 shows a large-scale 3DEC model of a KBS-3 repository. Parts of the model are made invisible to show the interior of the model, i.e. the deposition areas at 500 m depth. The model was used to simulate the thermo-elastic response only, i.e. without account of the initial stresses and without consideration of fractures, meaning that only one quarter of the problem needed to be modelled. The geometry and heat generation of the deposition areas, as well as the rock mass properties, were set according to the Forsmark near-field model described above.

The main reason for generating and analyzing the large-scale model was to check the validity of the mechanical boundary conditions applied to the near-field model described above (cf following section). The large-scale model is, however, also useful for exploring the way the thermal stresses will vary over time around the repository, particularly in the region between the deposition area and the ground surface. The change in horizontal stresses in this region will indicate the potential scope for, and extent of, transmissivity changes of steeply dipping fractures and fracture zones (cf Chapter 7).

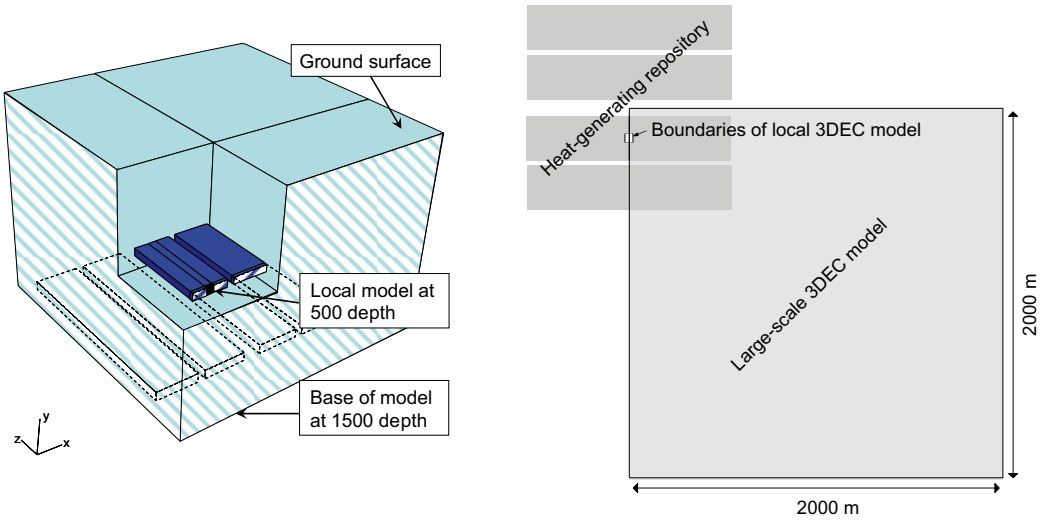

Figure 4-7. *Left: Quarter-symmetry large-scale thermo-mechanical 3DEC model. Right: Horizontal section.*

4.6 Boundary conditions

4.6.1 Near-field models

Construction and operational phase and initial temperate period

The bottom boundary and the vertical boundaries were fixed in the normal direction. A constant stress, corresponding to the in situ vertical stress, was applied to the top.

For the excavation phase, these are relevant conditions. The boundaries are at sufficient distances from the excavated rooms that their effects can be ignored.

For the heated phase, this will induce two errors:

1. In reality there will be a small increase in vertical load. However, this will not amount to more than about 3 MPa /Probert and Claesson 1997b/. Additionally, this increase in vertical load will be different at different positions in the repository, for instance in the central region, in edge regions and in corner regions. The analysis made by Probert and Claesson related to a repository with a square-shaped horizontal cross section and with a uniformly distributed heat load. For the reference layout (cf Figure 4-3) with non-heated areas between rectangular deposition areas the picture is more complicated.
2. In reality there will be horizontal expansion of the modelled volume. That expansion depends on the large-scale rock mass properties and on the large-scale repository layout.

The in situ stress state at repository depth is anisotropic with higher major horizontal than vertical stresses at all sites. Both errors above tend to overestimate the increase in that stress anisotropy. Ignoring the horizontal expansion and the increase of vertical load is therefore conservative and is the main, base case, approach used for the near-field models. Horizontal strains and vertical stresses from relevant parts of the large-scale model (cf Figure 4-7) were translated into more elaborated boundary conditions for a purely thermo-mechanical near-field model to verify the above, i.e. that expansion and vertical stress increase can be ignored. Figure 4-8 shows that the base case approach overestimates the tangential stress by about 4 MPa at the time of maximum stress some 40–100 years after deposition. At later times, however, ignoring expansion of the nearfield gives a tangential stress overestimate of about 10 MPa.

Figure 4-8 is relevant for the particular near-field model considered here (cf Figure 4-3). For models of tunnels located elsewhere, for instance close to the edges of the repository, the effects of ignoring large-scale expansion and large scale vertical stress increase would be slightly different.

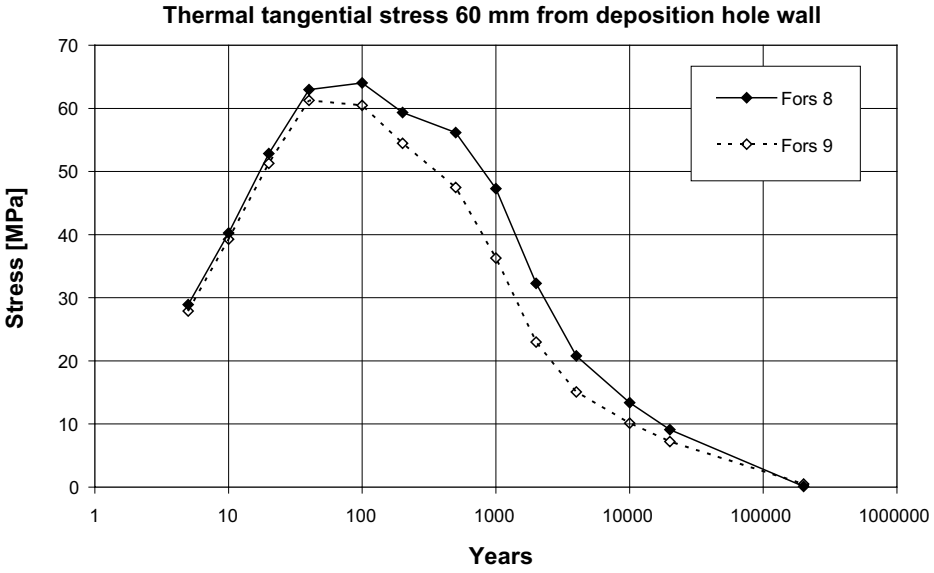

Figure 4-8. *Thermal stress close to deposition hole wall with base case boundary conditions (Fors8) and with boundary conditions extracted from large-scale model (Fors9). From /Fälth and Hökmark 2006b/.*

Glacial cycle

For modelling of the glaciation/deglaciation stage, the results of preliminary 2D FEM ice-crust-mantle analyses were used to specify boundary stresses. The 2D FEM analysis was based on the 1998 version of Lambeck's model of the most recent glaciation /SKB 2006c/, (B Lund, Dep. of Earth Sciences, Uppsala University, personal communication, 2005), assuming the ice-load evolution shown in Figure 4-9 and simplified earth models described in /Lund 2005/. The origin of the NW-SE scan-line was fixed at the point of the maximum North-Western ice sheet extension close to Lofoten, Norway. It should be mentioned here that the reference ice model now considered in the safety assessment /SKB 2006c/ implies that the ice-load should be approximately twice as high.

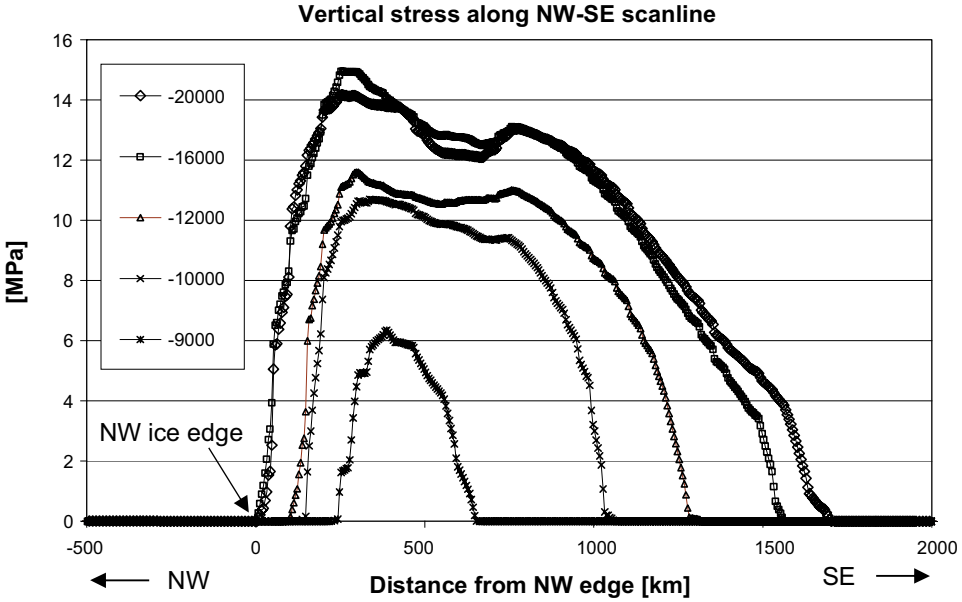

Figure 4-9. *Ice load as function of distance from the north-western ice edge at different times as obtained from 2-D FEM ice-crust-mantle analysis. Data from /Lund 2005b/. The legend gives time before present in years.*

The glaciation/deglaciation cycle was simulated only for the Forsmark models. The Forsmark site is not located directly on the NW-SE scan-line considered in Figure 4-9, however at an approximate distance of 800 km from the scan-line origin. Figure 4-10 shows stresses obtained from the ice-crust-mantle analysis for a point at 500 m depth 800 km southeast of the origin at the NW ice edge. Three sets of stress data corresponding to different stages of the cycle were selected for use as stress boundary conditions of the 3DEC Forsmark near-field model: the stresses during maximum load, the stresses at the time when the retreating ice margin passes the site and the stresses 9,000 years later.

In the Forsmark model, the major initial present-day stress is oriented NW-SE and the tunnel is assumed to be sub-parallel to that stress (cf Table 4-1). Therefore, the glaciation boundary stresses were applied normally to the model boundaries as shown in the right part of Figure 4-10.

Relevance and validity of boundary conditions for the glacial cycle

It is important to note that the stresses used as boundary conditions in the 3DEC near-field model were derived from an ice-crust-mantle model with a very schematic description of the earth /Lund 2005/. The crust was represented by a 100 km thick homogenous elastic, incompressible plate with uniform elastic properties and the mantle by an ideally visco-elastic medium. However, down to a depth of a few kilometres, the rock mass deformation modulus is typically 65–70 GPa, which is about 1/3 of the 192 GPa crustal average used as input in the FEM analysis /SKB 2005ab/. This means that the flexural stresses at repository depth should be about 1/3 of those obtained from the ice-crust-mantle FEM analyses as illustrated schematically in Figure 4-11.

In addition, the real crust is not incompressible, meaning that the Poisson ratio effect on the horizontal stresses will be smaller in reality than in the ice-crust-mantle FEM model. For typical values of Poisson's ratio, the horizontal stress addition should be about 1/3 of the stress addition obtained for the incompressible crust.

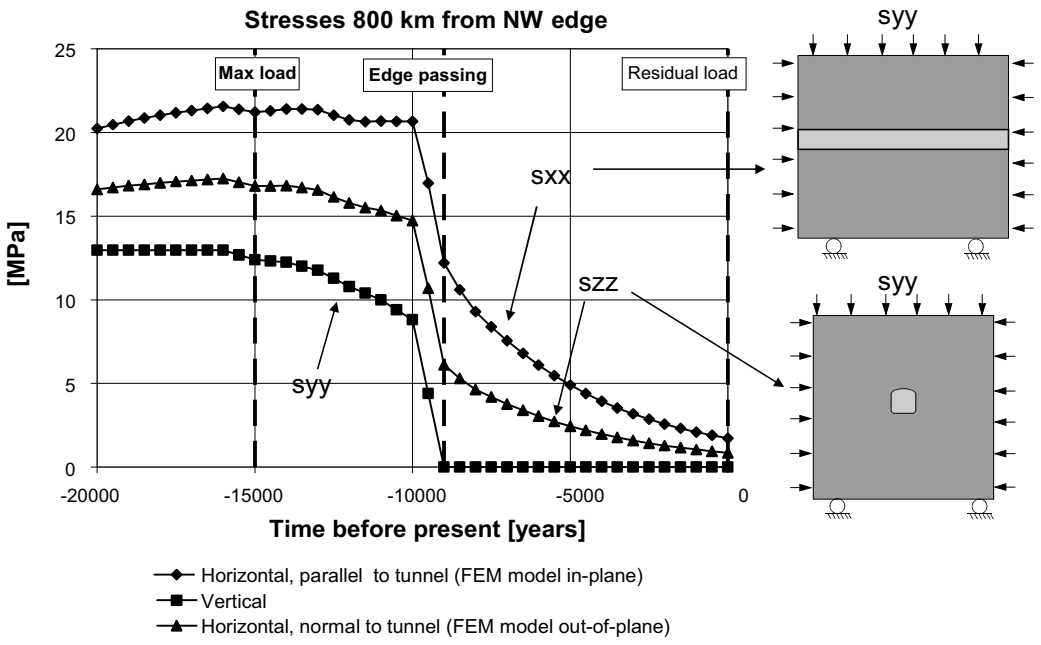

Figure 4-10. *Rock stresses generated by ice-load at 500 m depth as function of time. Stress boundary conditions were extracted for the three indicated instances of time.*

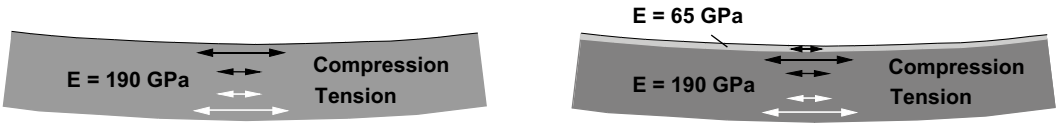

Figure 4-11. *Schematic of flexural stresses generated in homogenous elastic plate (left) and elastic plate with soft top layer (right).*

In summary, the horizontal stress additions should be 1/3 of those shown in Figure 4-10. Figure 4-12 (left) shows the calculated stresses modified accordingly. Figure 4-12 (right) shows corresponding results for a doubled ice-load (which is more relevant for the reference ice now considered in the Climate Report /SKB 2006c/), assuming for simplicity that all stress additions, vertical and horizontal, increase proportionally with the height of the ice sheet, (i.e. ignoring that the crust-mantle interaction will develop differently for different ice-loads).

During the period of actual ice cover, the ice load stresses shown in Figure 4-12 would stabilize the rock at all sites with typical in situ stress fields. Since the vertical stress additions are larger than the horizontal ones, the in situ stress anisotropy (with high horizontal stresses) found for instance at Forsmark would be reduced. Figure 4-13 shows the ice load stresses added to the Forsmark in situ stresses. During the period of ice-cover, the maximum deviatoric stress, as well as the ratio between major and minor stress are significantly lower than at present, giving increased stability. This is true for both ice load assumptions made here.

There is a period of reduced stability when the retreating ice margin passes and a few thousand years afterwards. According to the current understanding /SKB 2005b/, the present-day major/minor stress ratio at Forsmark is about 3.5 and would increase to about 4 at that time (Figure 4-13, right-hand vertical axes). The largest deviatoric stress is about 32 MPa and would increase to 36 MPa (assuming ice-load as in Figure 4-12, left) or 40 MPa (assuming the load shown in Figure 4-12, right).

Figure 4-14 compares Forsmark stresses for two cases: ice-load additions from FEM analysis as in Figure 4-10 and ice load additions adjusted and doubled as in Figure 4-12 (right). The right part shows that the unmodified stress additions used to specify 3DEC near-field boundary conditions give more potential instability than the more realistic ones (modified to account for crust compressibility and for depth dependence of the modulus of elasticity), which means that the mechanical ice-load effects in the near-field may have been overestimated.

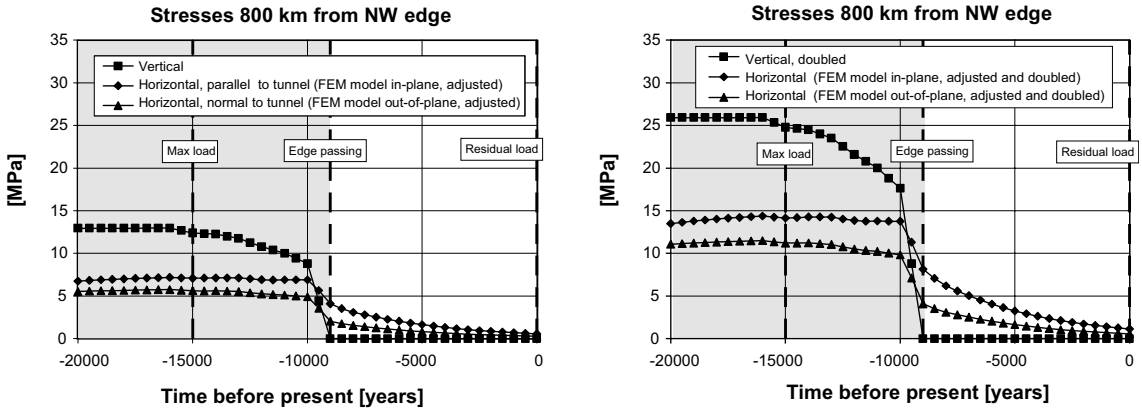

Figure 4-12. *Stresses induced by ice-load at 500 m depth. Grey-shaded parts represent time period of actual ice cover. Left: Results from ice-crust-mantle analysis, but with horizontal components reduced by 2/3. Right: same as left, but all stress components doubled.*

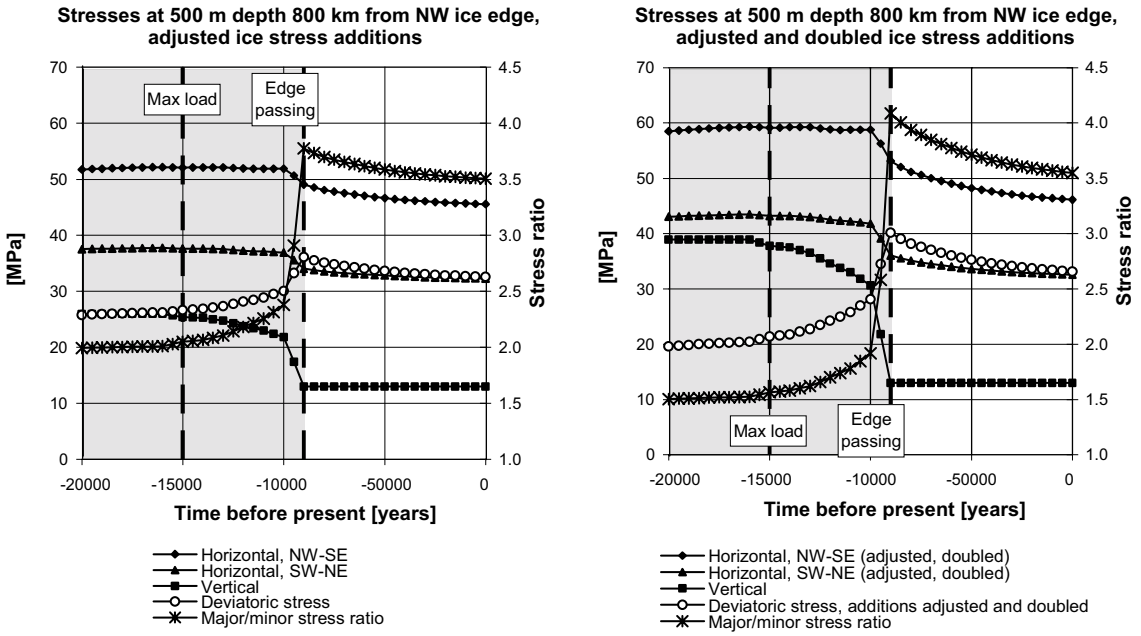

Figure 4-13. *Ice-load stresses added to present day Forsmark in situ stresses.*

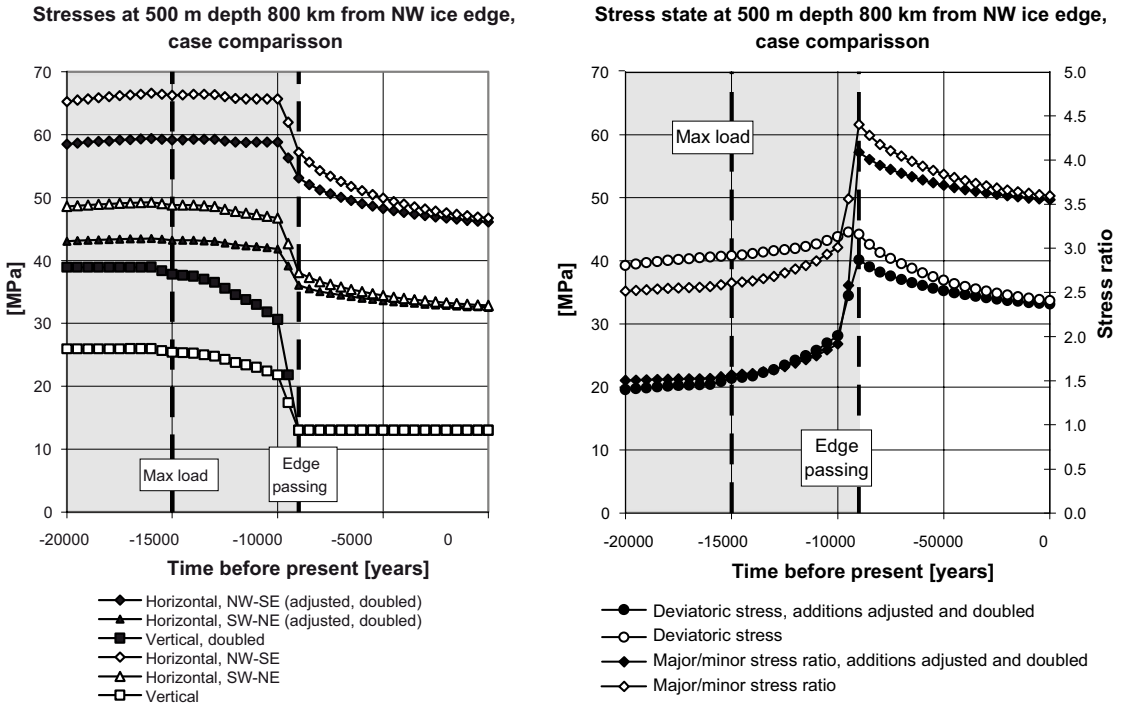

Figure 4-14. *Forsmark stresses under glacial load cycle for two different ice-load assumptions.*

The results focus on the period of instability during unloading. In principle, a similar period could be found during loading, i.e. prior to the arrival of the ice. However, the flexural stresses depend on the crust downwarping, which will be less before and during the arrival of the ice than during and after the retreat because of the time dependent behaviour of the viscous mantle. Therefore, the conditions during the retreat are used here to estimate instability effects close to and outside the ice margin.

Summary

Figure 4-15 shows a schematic summary of the near-field model base case boundary conditions applied in the different phases.

For the excavation/operation and thermal phases, the load on the top boundary equals the in situ vertical stress given in the site reports. The Forsmark near-field model was analyzed also using boundary conditions derived from the Forsmark large-scale model (cf Figure 4-8).

For the glaciation phase, stresses obtained from the ice-crust-mantle analyses are added to the existing boundary reactions as shown in Figure 4-10. The adjusted results (Figure 4-12) are likely to be more realistic, but have not been verified and are less conservative as shown in Figure 4-14 (right). The results shown in Figure 4-12 are, however, used in Chapter 8 to estimate large-scale fracture slip magnitudes (and the potential for slip) during a glacial cycle.

4.6.2 Large-scale model

The large scale thermo-elastic model was analyzed only for the thermal load (cf Figure 4-7), i.e. without regard to initial stresses. Excavation effects were not included. The top boundary (ground surface) was free whereas all other boundaries were fixed in the normal direction.

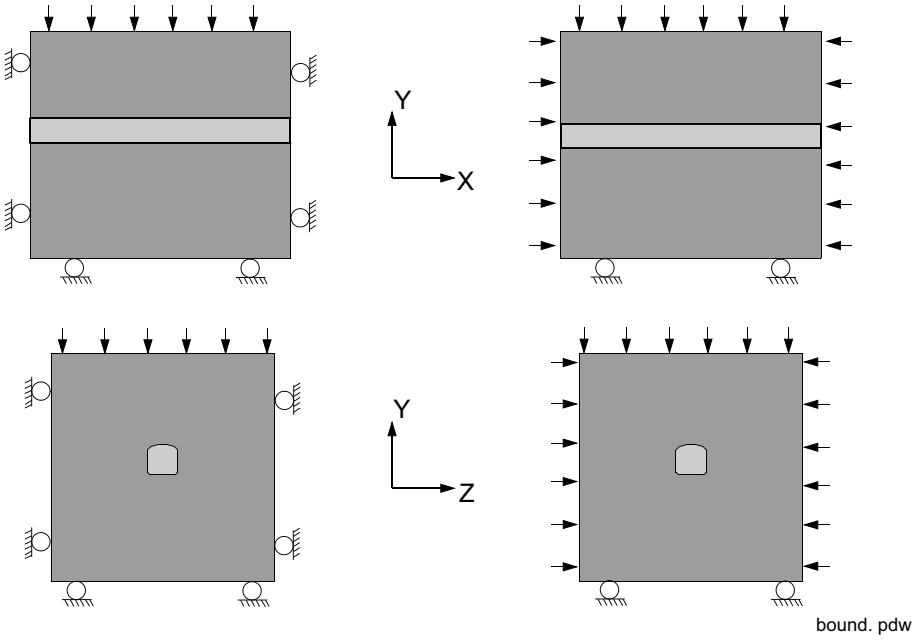

Figure 4-15. *Schematic of boundary condition used for construction/operational phase, and for base case temperate phase (left), and for glaciation cycle (right).*

5 Transmissivity changes of near-field fractures.

5.1 General

The results of 3DEC near-field models are used here, together with the different stress-transmissivity models and experimentally obtained displacement-transmissivity relations discussed in Chapter 2 to explore the effects of fracture movements on the hydraulic conditions in the near-field.

5.2 Fracture normal displacements

Figure 5-1, Figure 5-2, and Figure 5-3 relate to the three fractures that intersect the central deposition hole in the Forsmark model. The graphs show normal stress variations at a small number of points close to the deposition hole, and the consequent relative transmissivity variations at these points. The transmissivity changes are based on the stress-transmissivity model shown in the lower right parts of the figures, i.e. on the Sellafield aperture model described in Chapter 2 and on the cubic flow law. Because of the non-linear relations assumed to apply for single fractures, it takes substantial relaxations to increase the transmissivity in any significant way. At maximum, the transmissivity increased by a factor of 15 at one location on Fracture #6. (Figure 5-3). Otherwise, the maximum relative transmissivity increases are in the range of 10 to 20%.

Figure 5-4 and Figure 5-5 show fracture transmissivities at corresponding history points in the Simpevarp Stress Domain 2 model and in the Laxemar model, respectively. The same stress-transmissivity rule was applied as in the Forsmark model.

In the 3DEC simulations, the 5 MPa pore pressure and the bentonite swelling pressure were established instantaneously before the heating started. In reality, the temperature will start to increase as soon as the canisters are deposited, whereas the pore pressure and the swelling pressure will increase slowly over time after backfilling and closure. These pressures will increase at a rate that will depend on the time-scale of the overall restoration of the groundwater pressure and on the local permeability conditions. In reality, the effects of the pore pressure (decreased effective normal stress) will overlap with the effects of the heat and be partly or completely neutralized.

Looking at the Forsmark relative transmissivity plots (lower left in Figure 5-1, Figure 5-2 and Figure 5-3) and corresponding Simpevarp Domain 2 and Laxemar plots (Figure 5-4 and Figure 5-5) it is clear that the maximum increase is found after the thermal cycle (the pore pressure peak is not relevant unless there is a complete restoration of the natural groundwater pressure immediately after deposition). After some 100 years, the compression is at maximum with a corresponding small decrease in transmissivity at most of the monitored points. The small residual increase found at the end of the thermal pulse (compared with the conditions immediately before heating started) shows that some of the thermally induced deformations were inelastic.

The glacial cycle was included only in the Forsmark model. The response was similar to that of the thermal pulse, i.e. an increase in compression at most of the monitored points during maximum load and, after the completed cycle, stress relaxation and a small residual increase in fracture transmissivity. In this analysis, the effect of the glacial cycle was smaller than that of the thermal load. Also, the stress effects of the glacial cycle (with increased stress anisotropy during maximum load, rather than a decreased one) were most probably overestimated (cf discussion in Section 4.6.1).

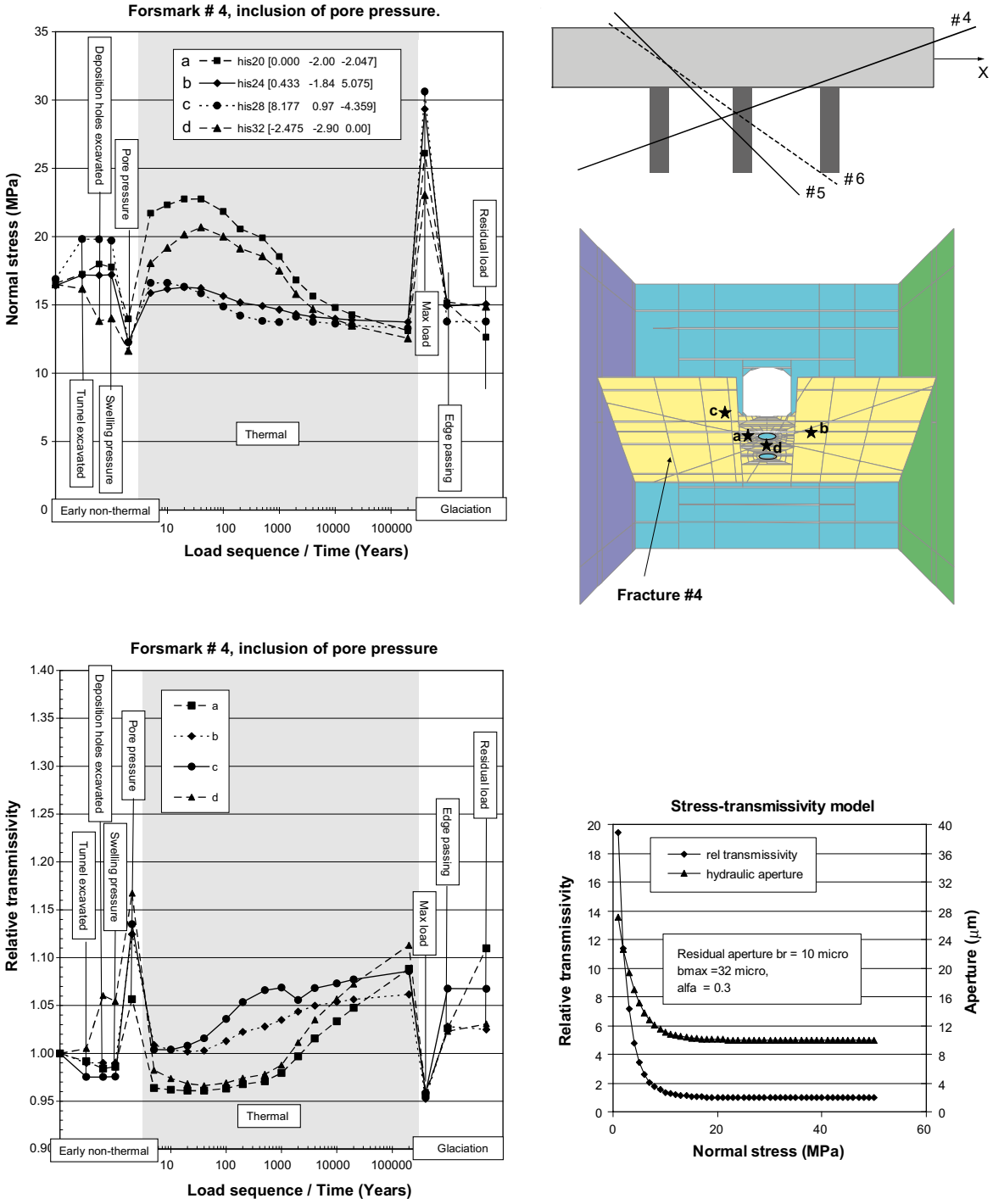

Figure 5-1. *Change in normal stress (upper left) and relative transmissivity (lower left) on some points on fracture #4. The relation used to calculate the relative transmissivity is shown in the lower right part.*

For fractures that are parallel with the tunnel walls and the tunnel floor, the transmissivity increase may be larger. It will also be more systematic, i.e. not localized to small regions as for the fractures shown here in Figure 5-1 through Figure 5-5. This is discussed at the end of this chapter.

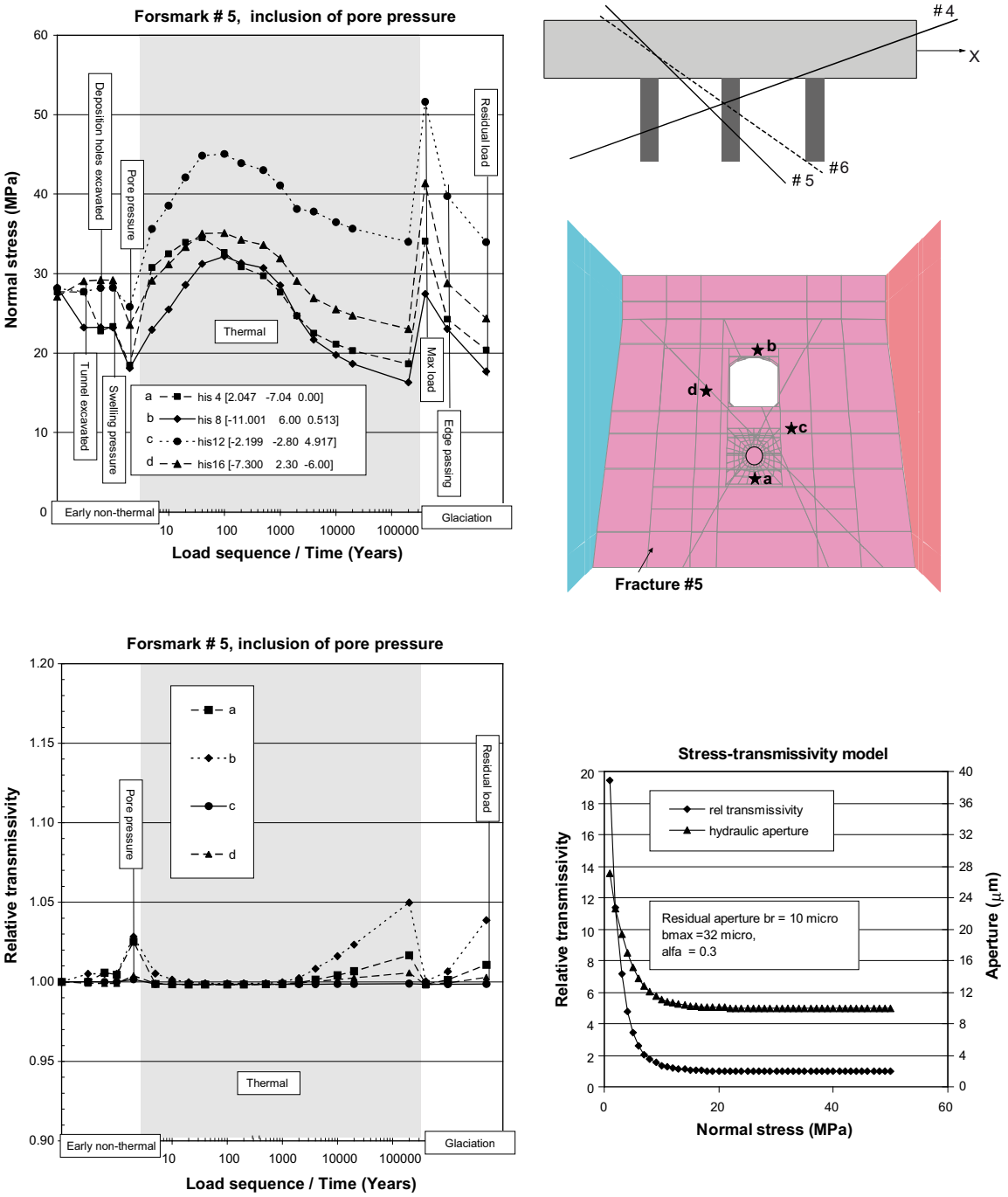

Figure 5-2. *Change in normal stress (upper left) and relative transmissivity (lower left) on some points on fracture #5. The relation used to calculate the relative transmissivity is shown in the lower right part.*

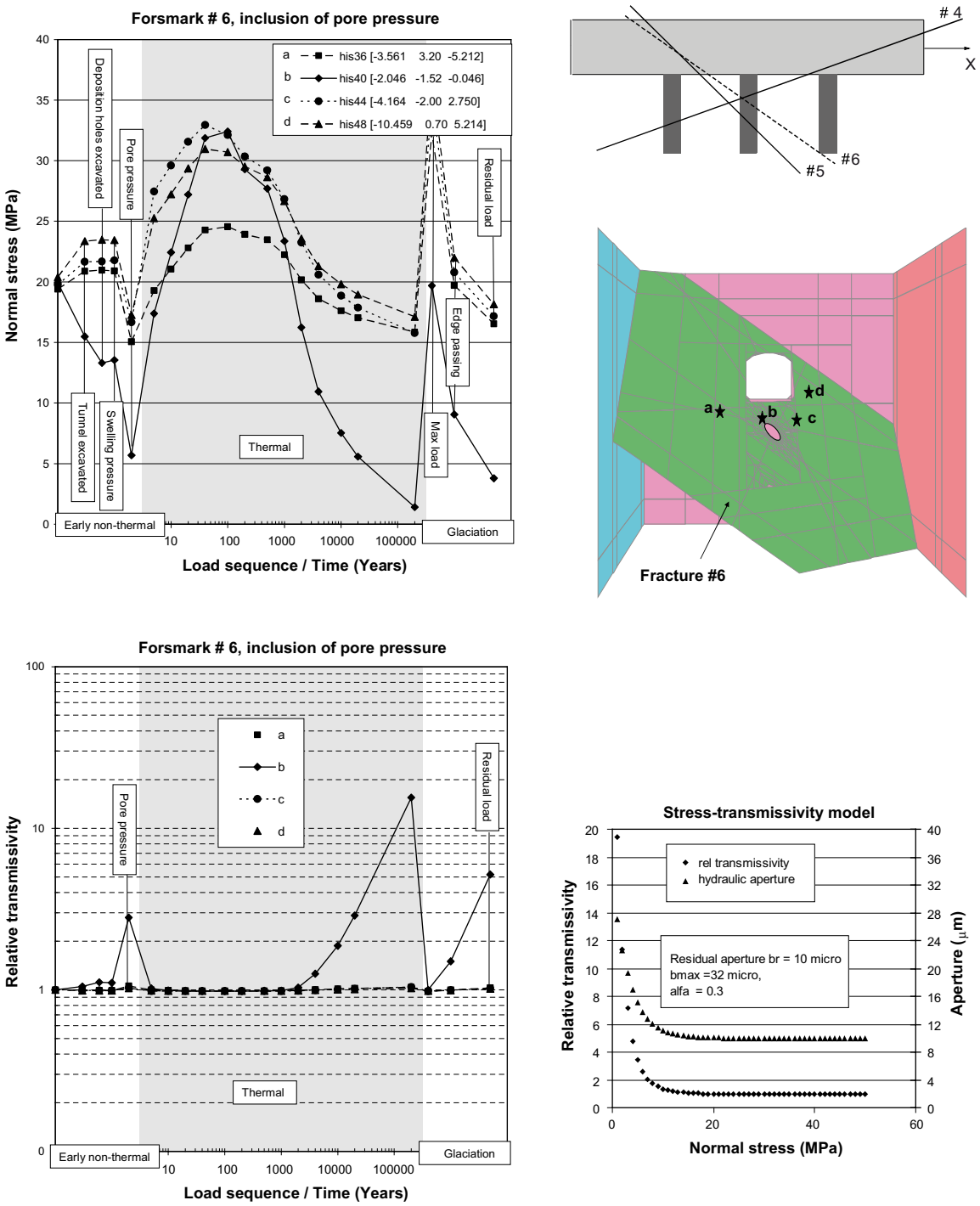

Figure 5-3. *Change in normal stress (upper left) and relative transmissivity (lower left) on some points on fracture #6. The relation used to calculate the relative transmissivity is shown in the lower right part.*

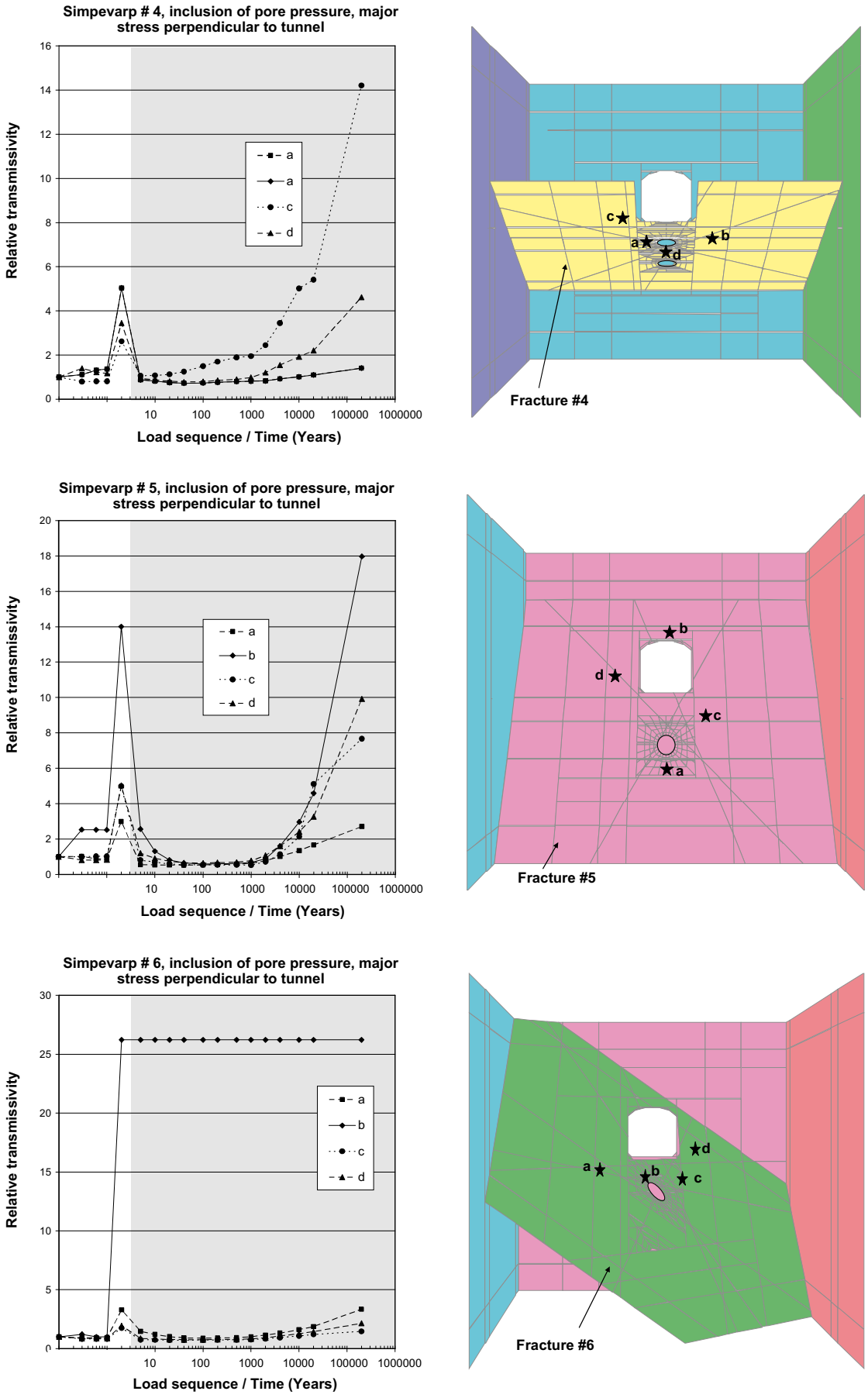

Figure 5-4. *Relative transmissivities of fractures in Simpevarp stress Domain 2 model.*

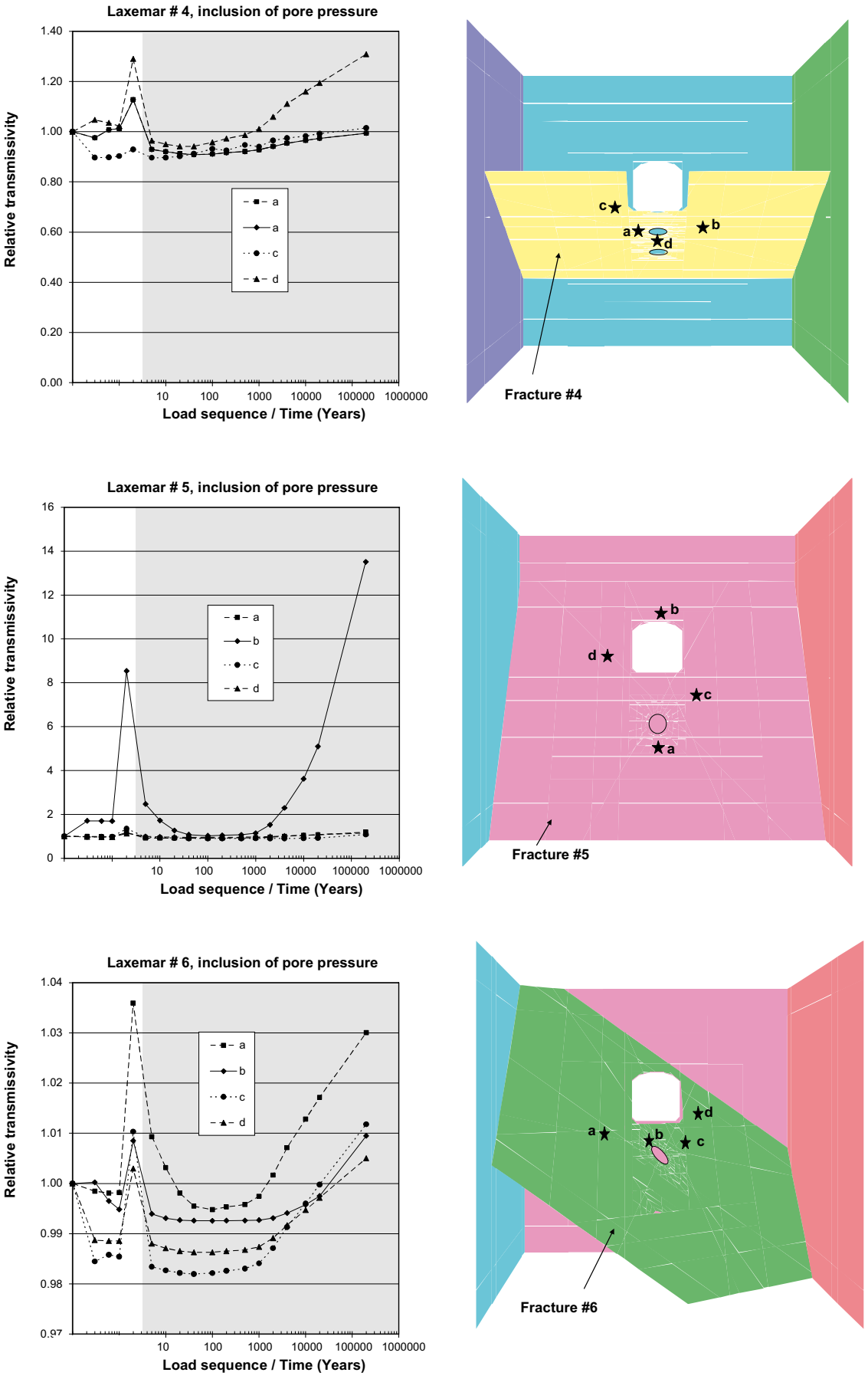

Figure 5-5. *Relative transmissivities of fractures in Laxemar model.*

5.3 Fracture shear displacements

Figure 5-6, upper left, shows fracture shear displacements at a number of points on the fracture that moved most in the Forsmark model. The fracture stiffness, friction and cohesion were set at the mean values given in the Forsmark site model (cf Table 4-3). The fracture dilation angle was set at 10 degrees, as suggested by /Olsson 1998/ (cf Figure 4-6). For a given load sequence and given geometrical conditions, these parameters control the extent of slip. The maximum slip (history point b on Fracture #4) is in the range of 4 to 5 millimetres for the reference case model.

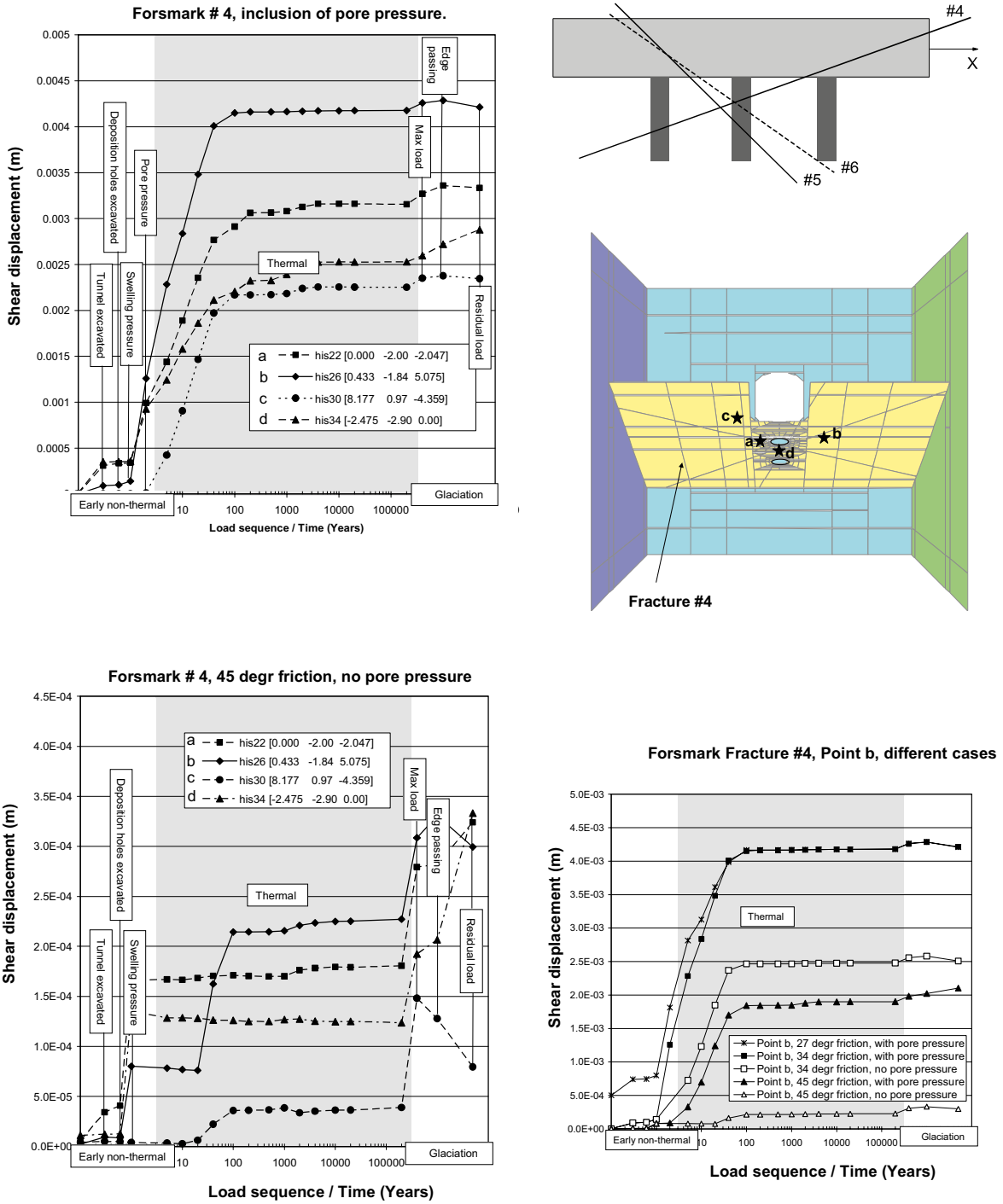

Figure 5-6. *Fracture #4. Left: history point shear displacements for two cases. Lower right: summary for a number of cases.*

For comparison, corresponding results are shown for a case without pore pressure and with a higher friction angle (45 degrees instead of 34 degrees) in the lower left part of the figure. The lower right part shows a summary of results, all regarding history point b on Fracture #4, obtained from different models.

The two other fractures that intersect the deposition hole, i.e. Fracture #5 and #6, did not displace more than 2 mm in any of the history points (cf normal displacement histories in the previous section)

In corresponding Simpevarp models, none of the recorded fracture displacements, including that of point b on fracture #4, are larger than about 1 mm /Fälth and Hökmark 2006b/.

The results summarised above, the findings in /Fälth and Hökmark 2006b/ and the experimental displacement-transmissivity relations shown in Figure 2-8 allow for the following observations:

- In the Simpevarp model, none of the fractures moved sufficiently to generate any transmissivity increases. For the modest displacements found in the Simpevarp model, the stress-transmissivity relation (Figure 2-8) would give unchanged transmissivities even for the lowest normal stress considered in /Olsson 1998/.
- In the Forsmark model, one of the fractures moved between 4 and 5 mm at some locations, Figure 5-6 (upper left). Looking at Figure 2-8 this may mean that the local transmissivity increased by two orders of magnitude. On the majority of that fracture plane, the displacements were smaller. In addition, the normal stress acting across fracture #4 was above 10 MPa (Figure 5-6, upper left), i.e. much larger than the 4 MPa maximum stress considered in Figure 2-8. This means that transmissivity increases would be less.

5.4 Near field transmissivity results

5.4.1 General

The transmissivity result examples above relates to three fractures, selected out of six fractures with different orientations but all located close to the central tunnel/hole intersection. For a complete set of results, see /Fälth and Hökmark 2006b/.

The proximity to the excavations controls the response of the fractures to the different loads. The tunnels are to be backfilled with material that does not produce any significant pressure on the peripheries. This creates a zone around the tunnel peripheries where normal stresses are low on planes that are parallel to the tunnel. That zone is particularly wide below the flat floor of horseshoe shaped tunnels (cf /Fälth and Hökmark 2006b/ for stress plots).

Figure 5-7 (left) shows, as an example, σ_z stress contours around the Forsmark tunnel after excavation. This stress component determines the normal stress on vertical fractures that are parallel to the tunnel. It appears to be larger than 3–4 MPa at distances larger than 1 m from the walls (dashed line). At most points, however, this stress is well over 5 MPa. This would give transmissivity increases of about one order of magnitude at maximum for 15 µm aperture fractures (cf Figure 5-7, right) that are vertical, parallel with the tunnel and located at that distance. Factures at larger distances and fractures that are aligned off the tunnel direction by some angle will have less change in transmissivity.

The σ_z stresses pictured in Figure 5-7 are calculated assuming the Forsmark stress state (cf Table 4-1). The stress-transmissivity relations apply for fractures of 15 µm initial hydraulic apertures, i.e. with transmissivities of $2.8 \cdot 10^{-9}$ m^2/s. A conservative generalization that is likely to be valid in most cases would be to assume that the transmissivity increase following excavation may amount to 2 orders of magnitude within a 1.5 m zone from the walls for vertical fractures that are parallel with the tunnel.

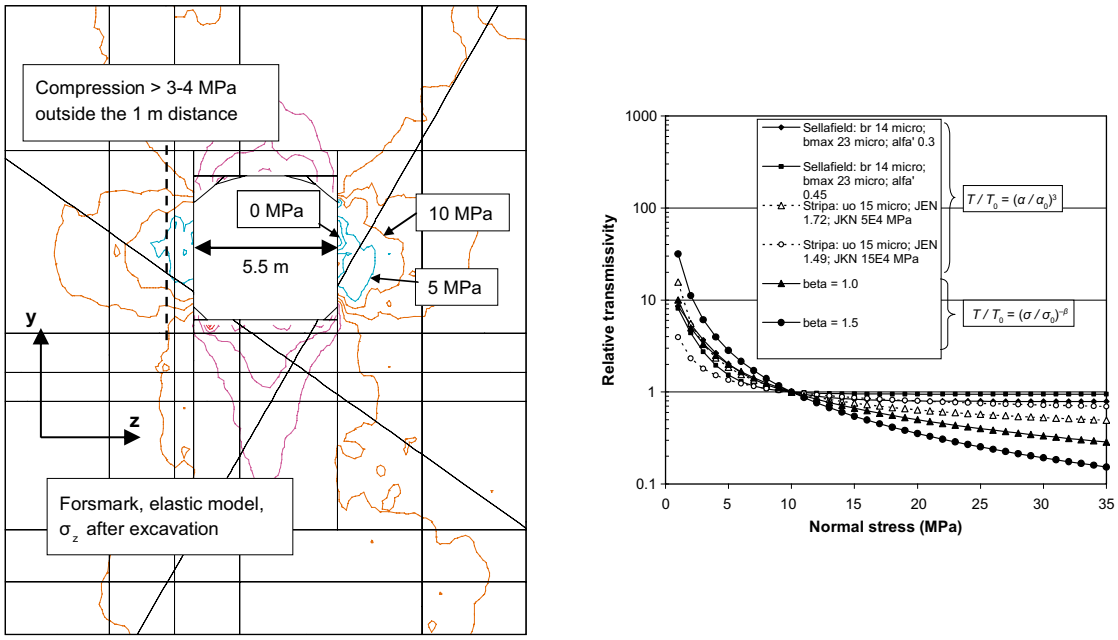

Figure 5-7. *Left: Contours of horizontal stress component normal to the tunnel in a section between two deposition holes. Right: Stress-transmissivity relation for 15 µm aperture fractures (cf Chapter 2).*

Fractures located at one or two metres distance from the repository openings will be either in increased or insignificantly reduced compression through the entire load sequence and will exhibit little displacement.

The cylindrical deposition holes are smaller in volume and do not have nearly as far-reaching effects on the stress field as the tunnel.

The region below the tunnel floor is not only stress-relaxed by the nearby low-pressure tunnel floor boundary, it is also the region of maximum thermal impact.

Figure 5-8 summarizes the above and the results of the 3DEC simulations schematically.

5.4.2 Fractures dipping 65–90

For steeply dipping fractures the influence of the region below the floor with low vertical stresses is not important. For fractures that are normal to the tunnel there will be only insignificant (#1) changes in transmissivity. For fractures that are parallel to the tunnel (#2) or oriented as #3 there will be differently sized regions of increased transmissivity around the walls.

5.4.3 Fractures dipping 0–65

Normal and slip movements on gently dipping fractures will be controlled by the conditions in the floor region, i.e. low vertical stress and maximum thermal impact.

5.4.4 Transmissivity increase

Looking at effects of normal stress variations, the transmissivity increased by a factor of 30 at maximum for the points shown in Figure 5-1 through Figure 5-4. For the fracture that slipped by the largest amount (Fracture #4 in the Forsmark model, Figure 5-6) the associated transmissivity increase may have been two orders of magnitude. A conservative approach would be to assume a two-order-of-magnitude increase in the grey-shaded areas as shown in Figure 5-8.

The stress-transmissivity relations applied here were based on the assumption of 10 µm residual hydraulic apertures. This means an absolute residual transmissivity of $8 \cdot 10^{-10}$ m^2/s. For more conductive fractures, the relative effects will be smaller (cf Figure 2-5).

A part of the transmissivity increase is due to the action of the pore pressure. In reality the pore pressure exists already in the initial state, which means that a small overestimate of the relative increase is made here.

Fractures	Nr		Dip range	Strike range
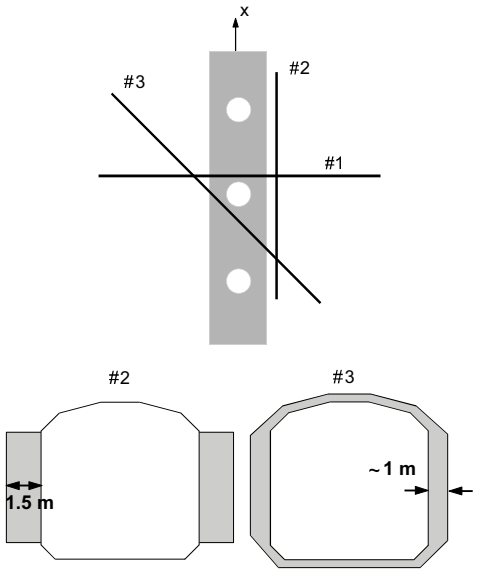	#1	No change in transmissivity	65–90	0±22.5, 180±22.5
	#2	Two orders of magnitude increase at the height section opposing the tunnel, no change elsewhere.	65–90	90±22.5, 270±22.5
	#3	Two orders of magnitude increase at up to 1 m distance from the tunnel periphery	65-90	45±22.5, 270±22.5
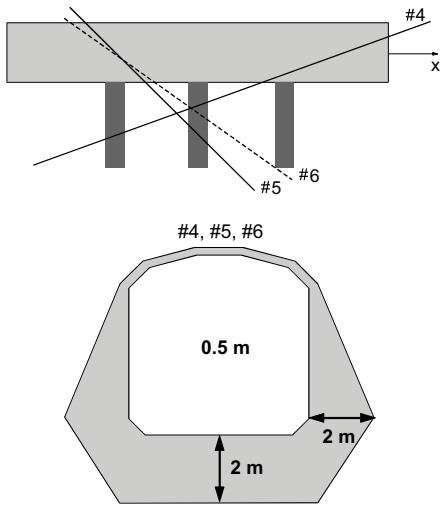	#4	Two orders of magnitude increase in region shown in left figure, no change elsewhere.	0–65	–
	#5	Two orders of magnitude increase in region shown in left figure, no change elsewhere	0–65	–
	#6	Two orders of magnitude increase in region shown in left figure, no change elsewhere	0–65	–

Figure 5-8. *Schematic summary of transmissivity results.*

6 Stress-induced spalling

6.1 General

High initial stresses or the combination of high initial stresses and subsequent thermal load may generate spalling, i.e. stress-induced brittle failure, in the walls of the deposition holes. The spalling process in general and its implications for the stability of SKB-3 type deposition holes in particular have been discussed by, for instance, /Martin et al. 1999, 2001/ and /Martin 2005/. The likelihood, extent and characteristics of spalling in full-scale KBS-3 deposition holes are being examined experimentally within the APSE experiment in the Äspö HRL /Andersson 2005/. One major objective of the experiment is to determine the spalling strength of rock in the walls of unsupported deposition holes. The APSE experiment is also directed to giving a detailed understanding of the process, for instance the importance of small support pressures for suppressing initiation of spalling. The present view is that the spalling strength of the APSE rock is about 55% of the laboratory-determined uniaxial compressive strength.

If the initial, pre-mining, stresses are sufficiently high, spalling may take place during the construction and operational phase as a response to the stress redistribution caused by excavation, in particular if the deposition tunnels are oriented normal to the major initial stress (see e.g. /Hökmark 2003/). In cases where the initial rock stresses are not sufficient to produce spalling by excavation, there is still the possibility that spalling may occur later because of the subsequent thermal load. 3DEC stresses obtained from the Forsmark, Simpevarp and Laxemar near-field models /Fälth and Hökmark 2006b/ are presented and discussed below and compared with spalling strength estimates.

6.2 Modelling of stresses

Figure 6-1 through Figure 6-4 show the major principal stress at points in different positions close to the wall of the central deposition hole in the Forsmark model, the two Simpevarp models and the Laxemar model. All points are located close to the wall:

Point 1a: 36 mm	Point 1b: 62 mm,	Point 1c: 36 mm
Point 2a: 35 mm	Point 2b: 28 mm	Point 2c: 36 mm

A number of cases are compared. For Forsmark there are several model versions, which allows observations to be made regarding the relative importance of fracture strength, pore pressure, swelling pressure, in situ stresses etc. For all cases and all points, the maximum stress value is found in the time range 40–100 years after deposition.

The grey-shaded area corresponds to the heated period (horizontal axis in years). Otherwise the horizontal axis represents the load step sequence (1, 2, 3, 4, 5) without coupling to time:

1. stress in the initial state;
2. after tunnel excavation;
3. after deposition hole excavation;
4. after full development of swelling pressure in the deposition holes;
5. after full restoration of the pore pressure.

In reality the swelling pressure and the pore pressure will both develop slowly over time and overlap with the period of thermal load.

The stress at the monitored points may be close to, or coincide with, the maximum stress found around the periphery of the hole at some instances of time, but, in general, the maximum stress

will be higher than the stress at the monitored points. In addition, the thermal stresses change over time, which means that the maximum tangential stress will be found at different points at different times. The results recorded at the selected points (Figure 6-1 to Figure 6-4) are, however, representative of how the stress at points with high stresses may vary over time.

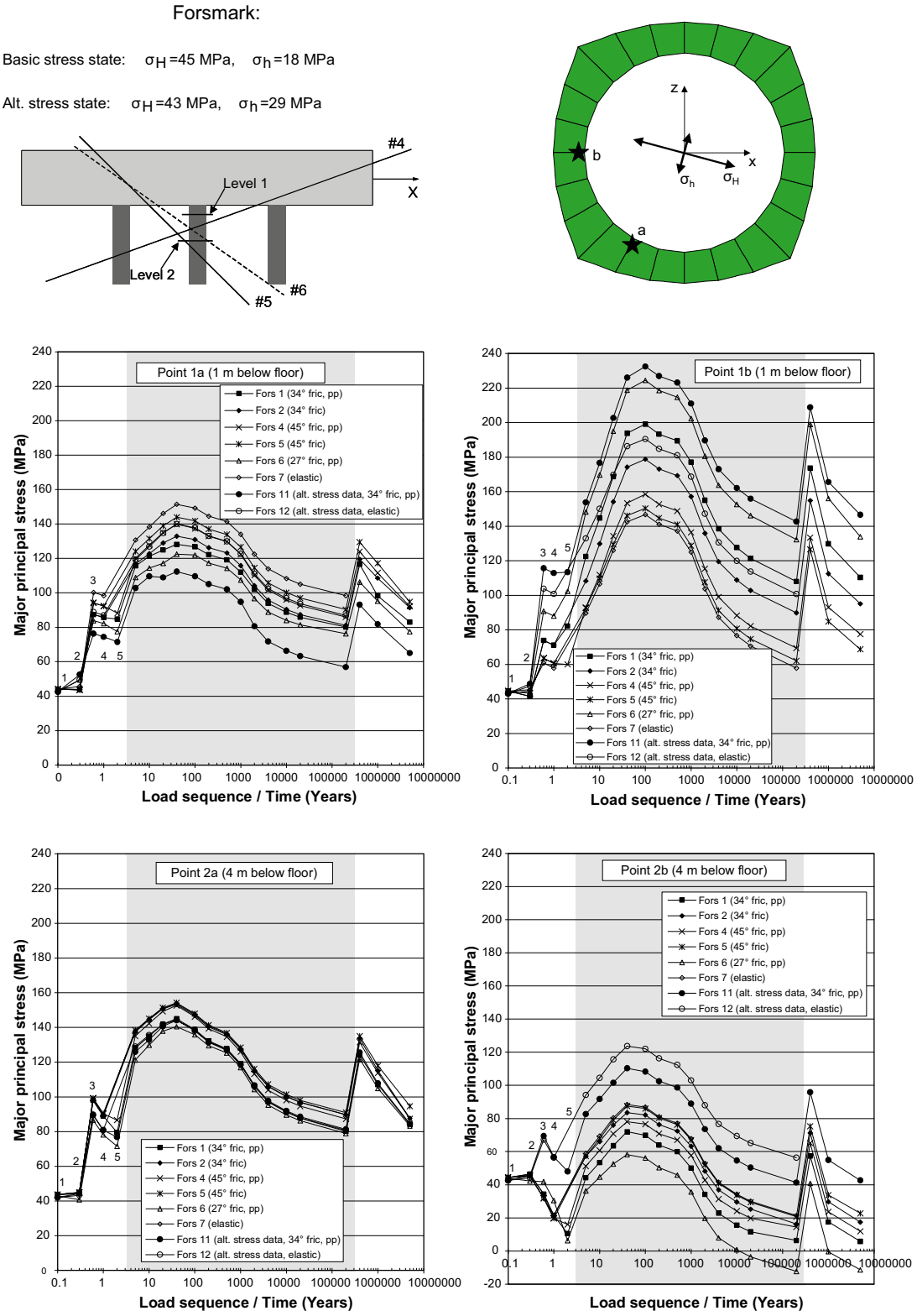

Figure 6-1. *Forsmark stresses. Fors1 is the base case with properties, stresses, pore pressure etc according to the description in Chapter 4. The 400 m models have been updated with respect to the stress state (see text above).*

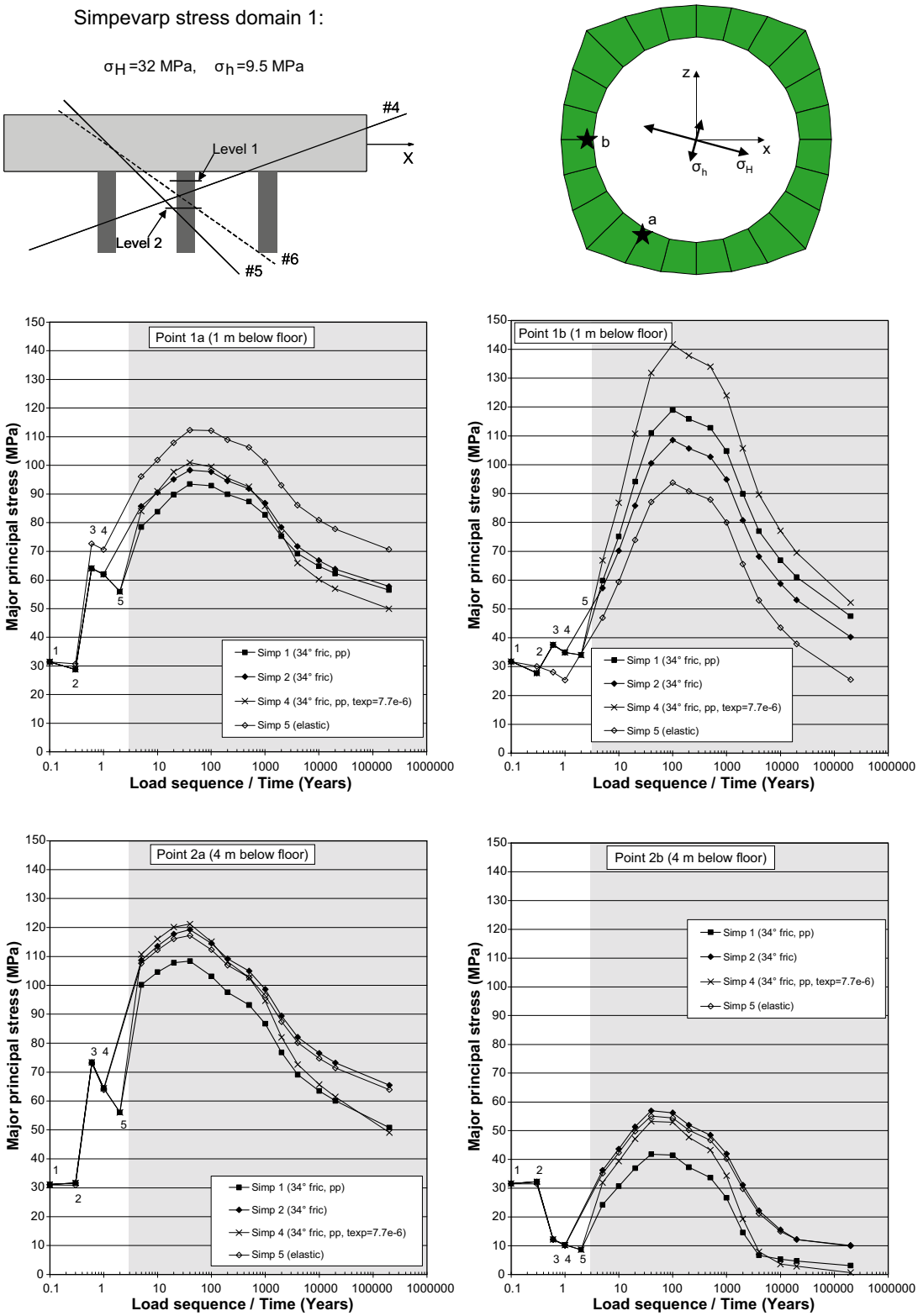

Figure 6-2. *Simpevarp I stresses. Simp 1 is the base case with properties, stresses, pore pressure etc according to the description in Chapter 4. Simp 4 is identical to the base case, except for the increased value of the thermal expansion coefficient.*

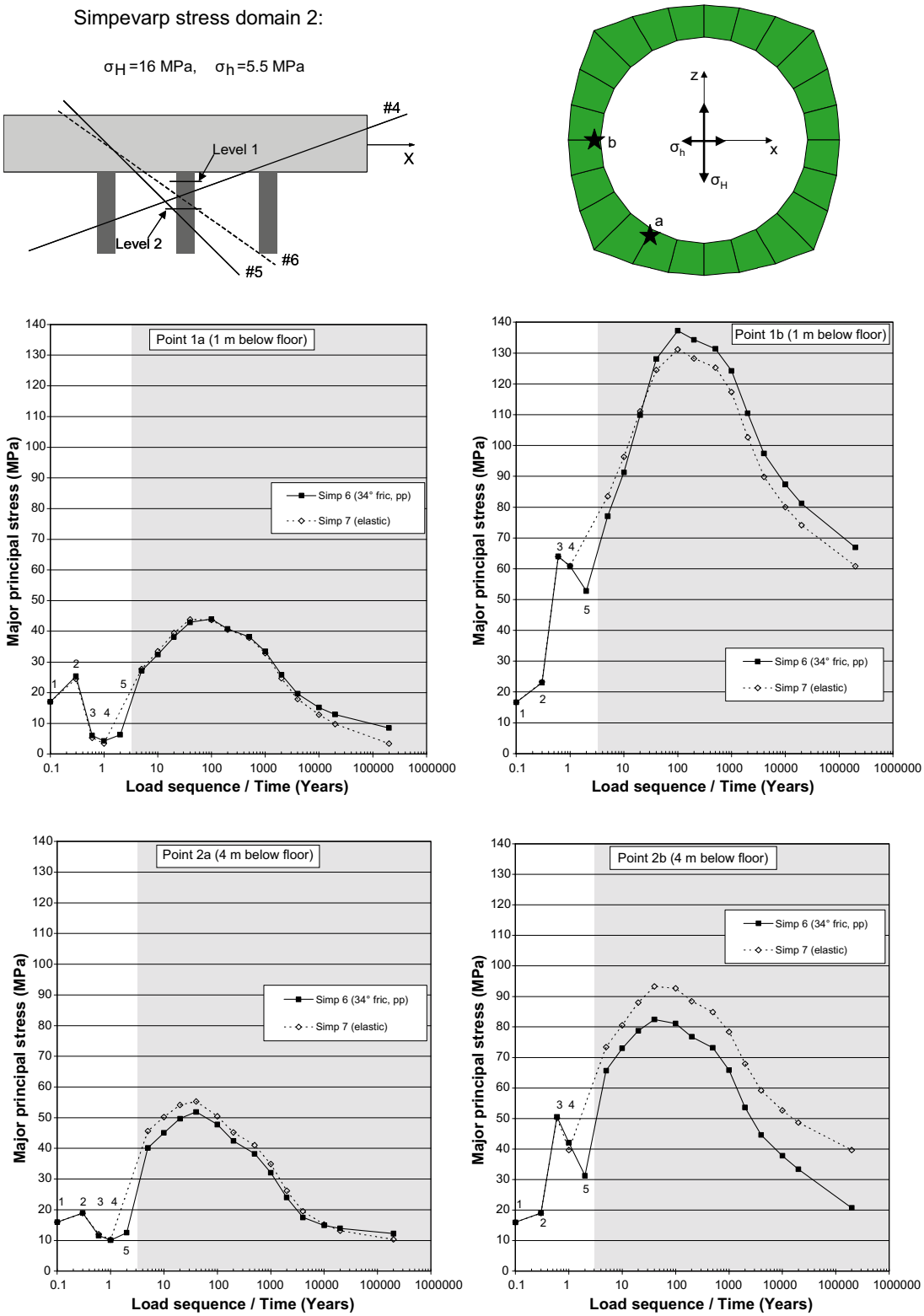

Figure 6-3. *Simpevarp II stresses. Simp 6 is the base case with properties, stresses, pore pressure etc according to the description in Chapter 4.*

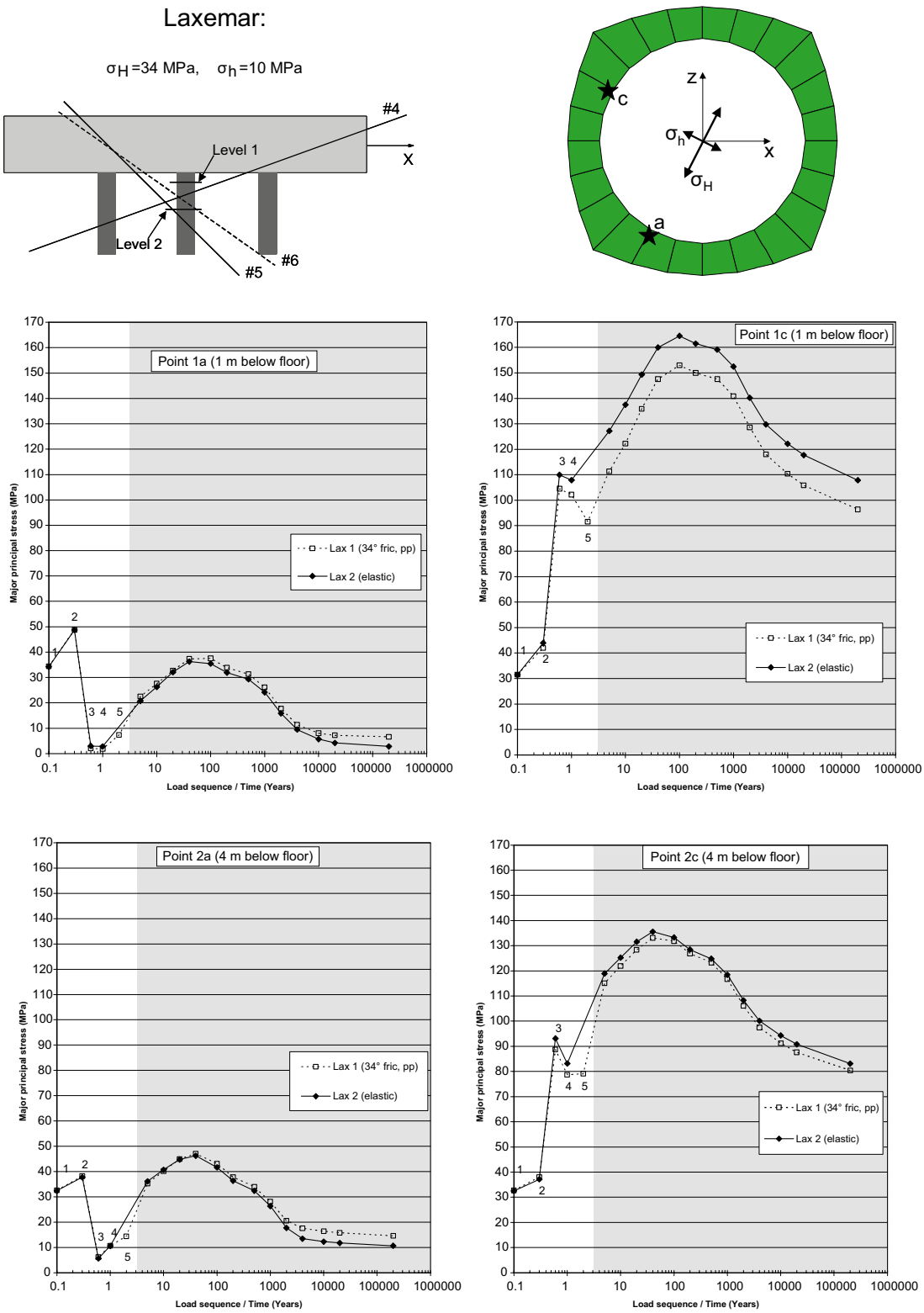

Figure 6-4. *Laxemar stresses. There is a base case version with fractures as described in Chapter 4 and with pore pressure. Lax 2 is a corresponding elastic model.*

6.2.1 Effects of slipping fractures

Effects of slipping fractures can be estimated from comparisons between results from elastic models and results from models with fractures of different strength (different friction angles; with and without pore pressure).

The stresses at the two a-points are modestly influenced by friction angle variations and by the pore pressure. The net effect of slipping fractures is a small stress relaxation: 15%–20% at the upper level and about 10% at the lower level. This applies for the Forsmark model (Figure 6-1) and for the Simpevarp Domain I model (Figure 6-2). For the low-stress Simpevarp Domain II model (Figure 6-3) and for the Laxemar model, the effects are smaller.

At the b-points, the integral effects of multiple, intersecting and slipping fractures are larger. At the lower level, there is a stress relaxation of between 20% (34° friction) and 35% (27° friction). At the upper level there are increases of about 40% and 55% for the two friction assumptions (34° and 27°). For the c-points (Laxemar, Figure 6-4) the effects are small.

6.2.2 Heat expansion coefficient

In the Simpevarp Domain I model, a value 25% higher than the base case value was tried (cf Table 4-3). This increased the maximum stress by about 10% at the a-points and, at the b-points, where thermal stresses are at maximum, by 17–25% (Figure 6-2).

6.2.3 Initial stress

The initial stress magnitude is important. The Forsmark and the Simpevarp Domain 1 models have principal in situ stresses of identical orientation but with different magnitudes. Table 6-1 shows the major principal stress at the four points after deposition hole excavation.

The Forsmark model was also analyzed for the 400 m repository depth, with major and minor in situ horizontal stresses being 43 MPa and 29 MPa, respectively (rather than 45 MPa and 18 MPa, as in the base case). The 2 MPa major stress reduction is too minor to be of any importance. The increase in minor horizontal stress gives a significant stress increase at the b–points and a small reduction at the a-points as expected, the general result being more uniform conditions around the periphery, but insignificantly increased maximum stress.

Also the alignement of deposition tunnels versus the major stress orientation is important. The Simpevarp 1 model and the Laxemar model have approximately equal stress magnitudes, but different major stress orientations. In the Simpevarp model, the major stress tends to be parallel to the tunnel axis, whereas it tends to be normal to that axis in the Laxemar model. This gives significantly higher stresses in the Laxemar model.

Table 6-1. Major stress (MPa) at selected monitored points after deposition hole excavation.

	Point 1a	Point 1b	Point 2a	Point 2b
Forsmark, Base Case	100	61	98	32
Forsmark, stress update, 400 m depth *	89	103	89	67
Simpevarp 1	72	28	73	12

* cf Table 4-1.

6.3 Using results from 3DEC analyses to estimate scope of spalling

6.3.1 General

Spalling that takes place during the construction and operational phase, in still open deposition holes, is not necessarily of importance to performance and safety. Detached rock fragments can be removed and cavities can be filled with, for instance, pieces of bentonite or with bentonite pellets before or during installation of the bentonite buffer. If the deposition holes remain intact during the construction and operational phase and the bentonite buffer has had time to take up water and begin to close the buffer-rock gap before the thermal stresses have reached levels that may cause spalling, then the bentonite support pressure will probably be sufficient to prevent spalling altogether, or to limit the growth of failed rock regions. /Cho et al. 2002/ and /Andersson and Eng 2005/, for instance, have concluded that confining stresses in the order of tens of kPa are sufficient to control spalling. In addition, if the bentonite-rock gap has closed, there will not be any disturbances of the geometry and homogeneity of the bentonite buffer because of displaced rock fragments. Thus, the main concern will probably be spalling induced by thermal stresses in deposition holes with still open bentonite-rock gaps.

The risk of spalling was estimated using 3DEC near-field modelling results described in the previous sections (Simpevarp and Laxemar). For the Forsmark site, a specific model with increased refinement of the near-field zoning and with more elaborated boundary conditions was used for the estimate. All models are described in detail in /Fälth and Hökmark 2006b/. The Simpevarp and Laxemar models referred to below are the elastic, no-pore pressure versions of the base case models. The stresses shown in Figure 6-1 through Figure 6-4 are not necessarily the largest ones that would be present, and cannot be used directly to determine if there will be spalling. The spalling estimates are based on the largest stresses found in the wall regions.

6.3.2 Forsmark

The Forsmark model /Fälth and Hökmark 2006b/ was analyzed assuming the rock type to be *granite-to-granodiorite* with a uniaxial compressive strength of 225 MPa. The major horizontal stress is 45 MPa, the minor horizontal stress 18 MPa and the vertical stress 13 MPa. The tunnels are inclined 15 degrees with respect to the major stress (cf Table 4-1).

The specific Forsmark 3DEC model considered here is one without fractures, without buffer swelling pressure in the deposition holes (and without pore pressure). To increase the accuracy of the stress-deformation analysis, this particular version of the model was specifically densely meshed in the immediate vicinity of the central deposition hole. To avoid over-prediction of the thermal stresses (cf Figure 4-8), the outer vertical boundaries of the model were moved to replicate the expansion and subsequent contraction of the local model volume within the large-scale model shown in Figure 4-7.

Figure 6-5 shows principal stresses in a horizontal section 4 m below the tunnel floor and in a vertical section along the deposition hole axis. Only rock within about 0.3 m distance from the walls is visible. The arrows show the tunnel axis orientation and the dashed lines indicate the two sections. The three sets of stress plots represent the state after excavation, the state after 5 years, and after 40 years, respectively. The stress tensor symbols scale with the projection of the principal stresses onto the viewing plane, whereas the colour code relates to the magnitude of the major principal stress (note that there are different colour codes for the three sets of plots).

The contour lines indicate areas where the major stress exceeds the spalling threshold, which is assumed here to be 124 MPa. This does not mean that spalling will occur everywhere within the contours. The stresses are calculated assuming linear elasticity whereas in reality the stress field will change as soon as the failure process begins. An estimate of the actually failed volumes is given in the following sections.

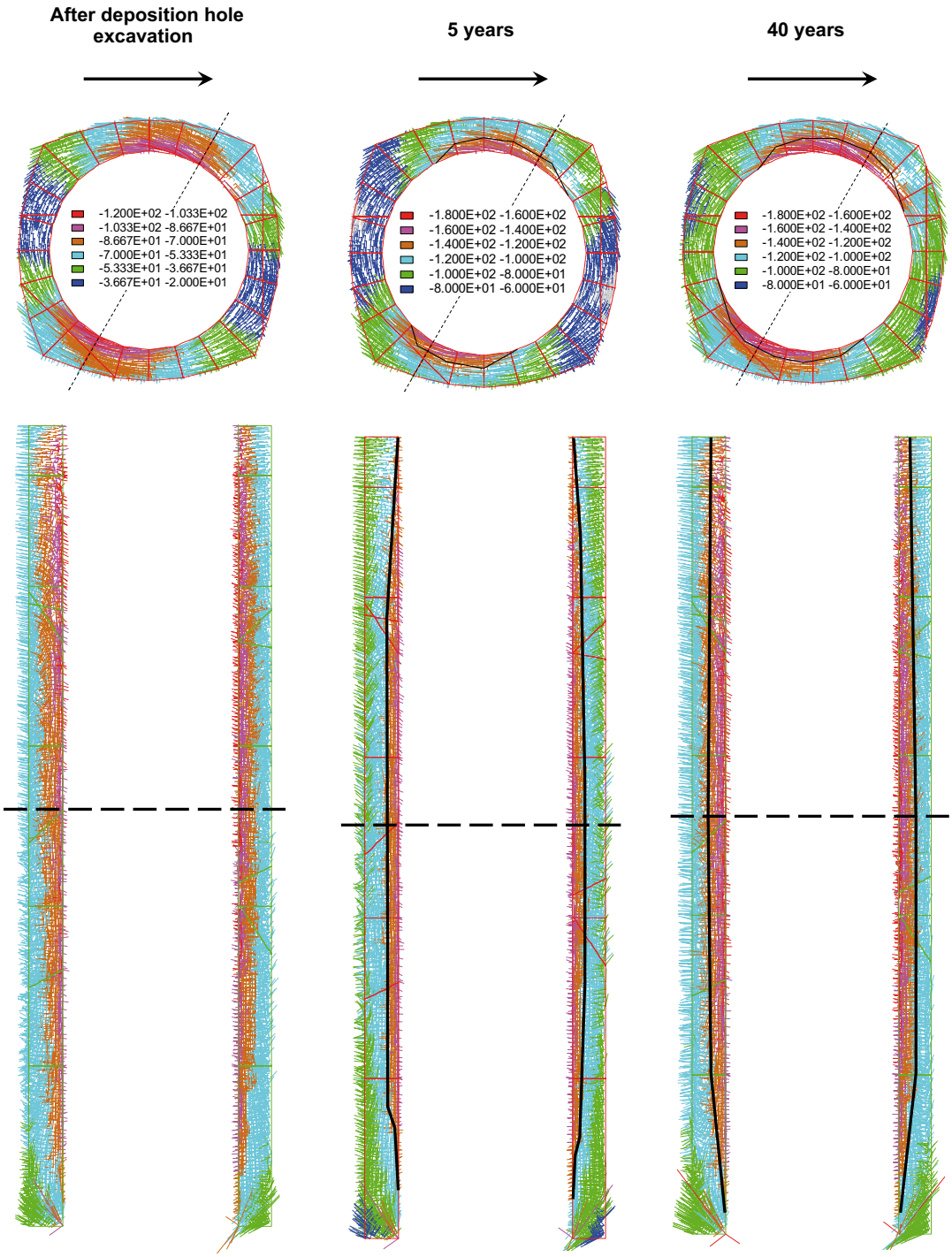

Figure 6-5. *Stresses around the central deposition hole (cf Figure 4-2) at different times.*

The following can be observed:

- The spalling threshold was not exceeded anywhere after completed excavation;
- After 5 years, the spalling strength was exceeded along two 1 m sections of the periphery to a maximum depth of about 0.1 m;
- After 40 years the spalling strength was exceeded along two 1.5 m sections of the periphery to a maximum depth of about 0.15 m.

Figure 6-6 shows the stress path of four points at different distances from the deposition hole wall. All points are at 4 m depth below the tunnel floor. The concepts of the plot are those used by /Martin et al. 2001/. Here, the damage initiation envelope is based on the assumption that the spalling strength is about 55% of the 225 MPa uniaxial compression strength. The horizontal and vertical axes represent the major and minor principal stresses, both normalized to the uniaxial compressive strength.

6.3.3 Simpevarp

The Simpevarp models were analyzed assuming the rock type to be *Ävrö granite* with a uniaxial compressive strength of 165 MPa. For Simpevarp, there are no high resolution models with moving boundaries, such as the specific Forsmark model described above. All Simpevarp models were analyzed assuming a 10 MPa swelling pressure in the deposition holes during the heated period. The risk of thermally induced spalling is, however, not an issue in deposition holes where the buffer has developed a supporting swelling pressure. For deposition holes without that supporting pressure, the tangential stresses would be 10 MPa larger, meaning that the spalling risk estimate for Simpevarp must be based on tangential stresses 10 MPa larger than the calculated ones.

In stress Domain 1, the major horizontal stress is about 32 MPa, the minor horizontal stress 9.5 MPa and the vertical stress 14 MPa. The tunnels are inclined 15 degrees with respect to the major stress. The excavation induced tangential stresses of about 82 MPa at borehole mid-height, i.e. below the spalling threshold assuming the spalling strength to be 55% of the uniaxial compressive strength. After 5 years of heating, the tangential stresses amounted to about 125 MPa, i.e. to 135 MPa if the swelling pressure is compensated for. This is well above the threshold. The development in Simpevarp, with deposition holes walls being stable during the construction and operational phase and then entering a state where spalling is likely to occur in the beginning of the heated phase (assuming that the bentonite buffer has not established a sufficiently firm contact with the rock wall that a support pressure has had time to develop) is very much similar to the situation in the Forsmark model described above.

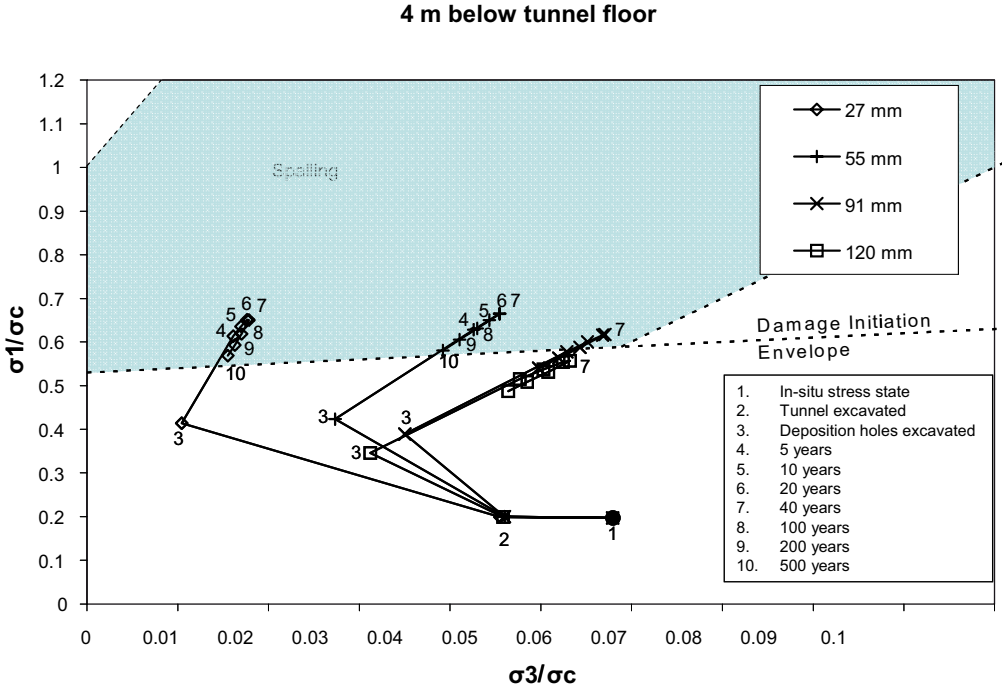

Figure 6-6. *Stress path for points at different distance from the deposition hole wall.*

In stress Domain 2, the major stress (15 MPa) is horizontal and normal to the tunnel. The minor horizontal stress is about 5.5 MPa and the vertical stress is 9 MPa. After 5 years the tangential stress is above the threshold, but by not nearly as much as in stress Domain 1.

6.3.4 Laxemar

The Laxemar 3DEC model gave larger tangential stresses than the corresponding Simpevarp model. The main reason is that the tunnel orientation assumed was the most unfavourable one of those given in /Jansson et al. 2006/, i.e. with the major in situ stress nearly normal to the tunnel axis. The maximum stress after deposition hole excavation was 122 MPa, which is above the 55% spalling threshold, given that the uniaxial compressive strength of the Laxemar version of the *Ävrö granite* is 195 MPa /SKB 2006/. This does not mean that spalling after excavation is generally more likely in the Laxemar subarea than in the Simpevarp subarea. If the tunnels were oriented as assumed in the Simpevarp Domain 1 model, i.e. almost aligned with the major stress, Laxemar deposition holes would be more stable than the Simpevarp holes because of the higher uniaxial strength.

6.4 Depth and extent of stress-induced failures

6.4.1 Empirical relation between stress and depth of failure

/Martin et al. 1999/ proposed Equation 6-1 below for prediction of the depth d_f of failure at the periphery of a circular opening of radius a. The depth of failure depends linearly on a as well as on the stress/strength ratio σ_{max}/σ_c. Here σ_{max} is the maximum tangential stress and σ_c the uniaxial compressive strength.

$$\frac{d_f}{a} = 1.25 \cdot \frac{\sigma_{max}}{\sigma_c} - 0.5 \pm 0.1 \qquad (6\text{-}1)$$

Equation 6-1 is a fit of data obtained from tunnels around the world and does not square with the high stress ratio assumed here for the spalling strength, i.e. 55% of the uniaxial compressive strength. The equation corresponds to an upper bound of about 50% as confirmed in Figure 6-7 (left). The right part shows the stress-depth relation for a 0.875 m radius deposition hole. Extending the uncertainty interval (e.g. ± 0.2 instead of ± 0.1) appears to be sufficient to cover the 55% stress ratio.

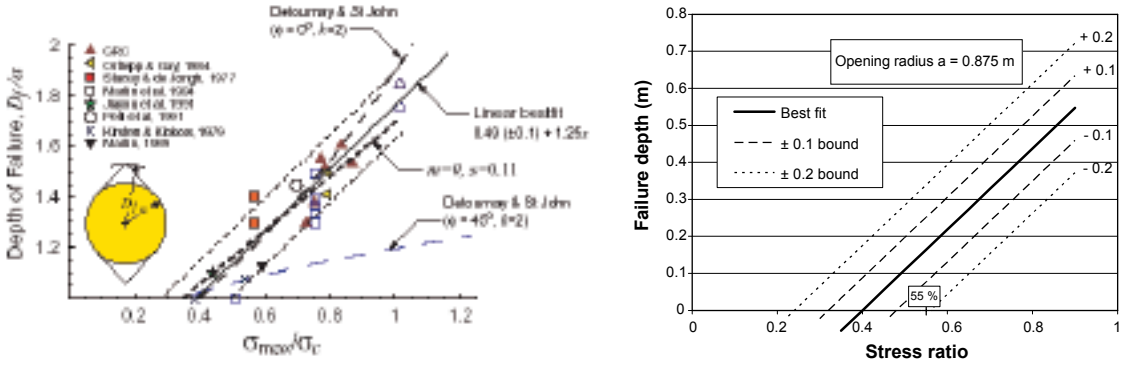

Figure 6-7. *Left: Depth of failure data. From /Martin et al. 2001/. Right: stress-depth relations for KBS-3 deposition hole.*

In the Forsmark example (Figure 6-5), the calculated maximum tangential stress is 165 MPa after 5 years and 175 MPa after 40 years. Using Equation 6-1 and assuming the –0.2 relation as shown in Figure 6-7 (right) this gives a spalling depth d_f = 20 cm after 5 years and 24 cm after 40 years.

6.4.2 Heated experiments

The stress-depth relation (i.e. Equation 6-1) is based on cases of tunnelling under iso-thermal conditions, with the maximum tangential stress being established immediately after excavation. It does not necessarily apply for openings that are in the elastic domain initially and then successively taken into the brittle failure domain by slowly increasing thermal loads.

Effects of heat on the stability of a highly stressed pillar between two holes excavated in the TASQ tunnel in the Äspö Hard Rock Laboratory were investigated within the Äspö Pillar Stability Experiment (APSE), cf Figure 6-8 (left). Minor spalling took place during excavation, but increasing thermal loads did not seem to increase the failure depth once a stable v-shaped notch, similar to the one shown in Figure 6-7 (left) had formed /Andersson and Eng 2005/. The vertical extension of the failure increased, however (cf Figure 6-8, right). The findings seem to support the notion that the depth of failure is controlled by the tangential stress that prevailed locally when the failure started, and not by subsequent stresses. Note that the failure did not extend into the floor region, i.e. the tunnel EDZ.

In URL in Canada, brittle failures were found along nearly vertical lines in the walls of 0.6 m holes, drilled in the floor of a tunnel in fracture-free, highly stressed rock /Martino and Read 1995/. Spalling to a depth of about 50 mm from the walls occurred as a result of the excavation. In the top part of the hole, down to depth of about 0.5 m below the tunnel floor, no spalling was observed. During a subsequent heating phase, the failure propagated downwards such that the failure zone was continuous down to the bottom of the hole at the end of experiment, still with the exception of the top 0.5 m. The depth of the failure, however, did not change much during the period of increasing thermal load.

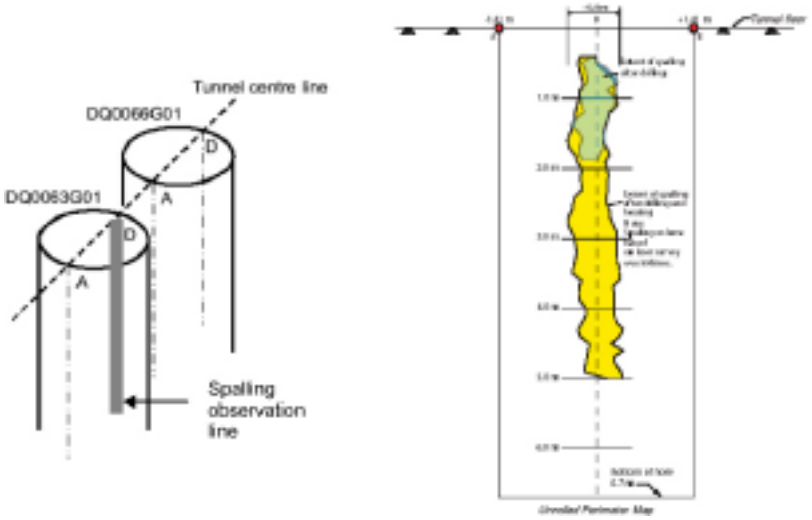

Figure 6-8. *Äspö Pillar Stability Experiment. Left: schematics of pillar geometry (from /Andersson and Eng 2005/). Right: failure caused by excavation and heating (From /Martin 2005/).*

6.5 Spalling risk assessment in deposition holes at the different sites

6.5.1 General

The results of the thermo-elastic 3DEC analyses can be used to decide whether spalling will occur in the construction and operational phase, during heating or not at all, provided that relevant values of the spalling strength are known.

At present, it is not possible to calculate the actual shape or depth of thermally induced failures. Experience is that the failures will be notch-shaped (cf Figure 6-7, left) and that the notch will self-stabilize at some depth that depends on the stress that prevailed at the time of the failure. Once the notch is stable, subsequent increases in stress will not increase the depth of the failure. The experience of brittle failures induced by continuously increasing thermal stresses is, however, not extensive at present. When the full evaluation of the APSE experiment is at hand, it may be possible to make quantitative estimates.

For now, using the Forsmark example, a rough estimate may be based on the following:

If the failure takes place after 5 years, the notch depth would be about 20 cm according to Equation 6-1 (using the –0.2 limit in Figure 6-7, right). This is about twice as deep as the spalling strength contour shown in the 3DEC plot (Figure 6-5, centre). It is about four times the failure depth found in AECL's heated failure test /Martino and Read 1995/. Therefore it is likely that the notch will form and stabilize much earlier, and at a lower tangential stress, perhaps at a depth of 0.1 m. The APSE experiment gave a notch depth of 0.07 m and a lateral spalling extent of about 0.8 m /Martin 2005/.

6.5.2 Site overview

The 3DEC results presented here indicate that there will be no spalling during the construction and operational phase (provided again that the ratio between spalling strength and uniaxial compression strength is 55%) in Forsmark and Simpevarp, but there will probably be in Laxemar. These results are not generally valid for any of the sites other than Simpevarp (Domain 2). The modelling results from the different sites (or subareas) depend very strongly on the assumptions made regarding tunnel orientation:

- In the Forsmark and Simpevarp I models, the tunnels were almost parallel with the major horizontal stress, which gives relatively modest tangential stresses and reduces the spalling risk.
- In the Simpevarp II model, the tunnel was normal to the major horizontal stress. However, the stresses magnitudes are sufficiently small that the tangential stresses did not exceed the spalling threshold.
- In the Laxemar model, the tunnel was almost normal to the major stress. This gave tangential stresses above the spalling threshold. Yet Laxemar has the same in situ stress as Simpevarp 1 and a higher threshold.

Because of the above, the 3DEC results cannot be used for direct and unbiased comparisons between the sites, only between the specific layout solutions modelled here.

In Forsmark, Simpevarp (stress Domain I) and Laxemar there will almost certainly be spalling because of the thermal load (assuming that there is no supporting bentonite swelling pressure).

In conclusion, forecasting if and when spalling will take place is difficult because of the many uncertainties. The spalling strength depends on the uniaxial compressive strength (cf Figure 6-7) for which mean values and standard deviations are given in the site-descriptive models /SKB 2005ab, 2006a/. The 55% stress/strength ratio assumed here in the Forsmark example was based

on findings made for the APSE deposition holes in the TASQ tunnel and is relevant for Äspö diorite /Andersson 2005/. The present view is, however, that this figure, or rather 57% ±2%, is likely to be relevant for coarse-grained and medium-grained crystalline rocks in general /Martin 2005/.

Table 6-2 shows 9 cases for which spalling risks estimates are made. The 30% and 40% columns are included for completeness and comparison (note that these values are within the bounds shown in Figure 6-7, left). Table 6-3 shows that the sensitivity of the spalling risk to uncertainties in, for instance, data (UCS) and conceptual understanding (factors controlling stress/strength ratio) is very large. The table is based on the maximum stresses calculated at the deposition hole wall without account of fractures, pore pressure or swelling pressure. For each of the sites, there are 9 cases of spalling strength corresponding to different assumptions regarding UCS and the stress/strength ratio (Table 6-2).

The row representing the reference strength case (UCS = mean value; spalling threshold stress/strength ratio = 55%) is grey-shaded.

The maximum stresses were obtained from the modelling results as described below.

For the Forsmark columns, values were taken from a specific, finely meshed model with vertical boundaries moving to reproduce the model-scale thermal volume expansion /Fälth and Hökmark 2006b/, cf Figure 4-8. This model was analyzed without account of the swelling pressure. The consequences of the recent revision of the Forsmark in situ stresses are not included (i.e. horizontal in situ stresses are 45 MPa and 18 MPa, respectively). Table 6-1 indicates that the maximum stress would be approximately the same, meaning that the estimates made in Table 6-3 are probably also valid for the updated stress model.

For the Simpevarp and Laxemar columns, the stresses were obtained from roller boundary models, i.e. with vertical boundaries fixed in the normal direction, and with account of the swelling pressure. To find stress values relevant to the thermal spalling risk, 10 MPa (corresponding to the swelling pressure support) was added to the 5-year and 40-year columns. To compensate for volume expansion the 40-year stress was reduced by 4 MPa (cf Figure 4-8 and /Fälth and Hökmark 2006b/).

It should be pointed out again that the risk estimates above are valid for the layout solutions analyzed here. In Laxemar, for instance, there are several deposition areas with other tunnel orientations than the one assumed here /Jansson et al. 2006/. An unbiased site comparison must include spalling risk estimates for all tunnel orientations considered and also give quantitative estimates based on statistical distributions given for stresses and intact rock properties in the site descriptions. The spalling risk overview above is, however, in agreement with more general and quantitative risk estimates reported by /Martin 2005/.

Table 6-2. Strength cases.

	Spalling strength 30% of UCS	Spalling strength 40% of UCS	Spalling strength 55% of UCS
UCS = Mean – σ	1	2	3
UCS = Mean	4	5	6
UCS = Mean + σ	7	8	9

Entries to Table 6-3 are as follows:

“x”	Spalling	Max stress > spalling strength + 5 MPa
“?”	Risk of spalling	Max stress = spalling strength ± 5 MPa
“–“	No spalling	Max stress < spalling strength – 5 MP

Table 6-3. Spalling risk overview. Mean values and standard deviation values of UCS are obtained from the site-descriptive models /SKB 2005ab, 2006a/. Note the difference between Simpevarp and Laxemar versions of Ävrö granite.

	Forsmark (granite to granodiorite) UCS = 226 MPa sdev = 22 MPa			Simpevarp I (Ävrö granite) UCS = 165 MPa sdev = 30 MPa			Simpevarp II (Ävrö granite) UCS = 165 MPa sdev = 30 MPa			Laxemar (Ävrö granite) UCS = 195 MPa sdev = 20 MPa		
Strength case	**Exc 114***	**5 yr 165***	**40 yr 175***	**Exc 82***	**5 yr 135***	**40 yr 148***	**Exc 64***	**5 yr 97***	**40 yr 120***	**Exc 122***	**5 yr 154***	**40 yr 193***
1	x	x	x	x	x	x	x	x	x	x	x	x
2	x	x	x	x	x	x	x	x	x	x	x	x
3	?	x	x	x	x	x	–	x	x	x	x	x
4	x	x	x	x	x	x	x	x	x	x	x	x
5	x	x	x	x	x	x	?	x	x	x	x	x
6	–**	x**	x**	–	x	x	–	x	x	x	x	x
7	x	x	x	x	x	x	x	x	x	x	x	x
8	x	x	x	?	x	x	–	x	x	x	x	x
9	–	x	x	–	x	x	–	–	x	?	x	x

*) Maximum stress (MPa) after deposition hole excavation, after 5 years of heating and after 40 years of heating.
**) see Figure 6-5.

7 Effects on far-field fractures

7.1 Temperate period

7.1.1 Stresses between the repository and the ground surface

The large-scale Forsmark 3DEC thermo-mechanical model (cf Figure 4-7) was used to examine the stresses above (and below) the repository as a function of time. The large-scale model did not include tunnels or deposition holes, meaning that stresses are not disturbed by openings. The calculated 3DEC thermo-elastic stresses agree well, qualitatively and with respect to order of magnitude, with corresponding stresses calculated analytically by /Probert and Claesson 1997b/ for a generic, square-shaped repository at 500 m depth. There is, for instance, high compression within a volume around the repository and regions of horizontal tension above and below that volume. The stress magnitudes as well as the volumes of rock being in tension change over time as illustrated in Figure 7-1.

The results presented below relate to the scan-line shown in Figure 7-2. Figure 7-3 and Figure 7-4 show the calculated thermo-elastic horizontal stresses superpositioned on the minor and major horizontal in situ stresses, respectively. In situ stresses were obtained from depth-stress relations given in the Forsmark site-descriptive model.

Regions of tensile horizontal stresses are found, but appear to have small depths. In the minor stress direction, stresses are compressive below 100 m depth at all times (Figure 7-3 and Figure 7-5). At depths below about 350 m, the compression increased at nearly all times, with only insignificant exceptions at early stages. In reality, steeply dipping fractures will control the stresses in the upper parts (uppermost 50–100 m) and be at low or zero compression where the results from the thermo-elastic 3DEC model would indicate tension. In fractured rock, tensile stresses such as those obtained from the linear elastic 3DEC model, are not likely to occur.

Note that compressive stresses are negative in the following diagrams.

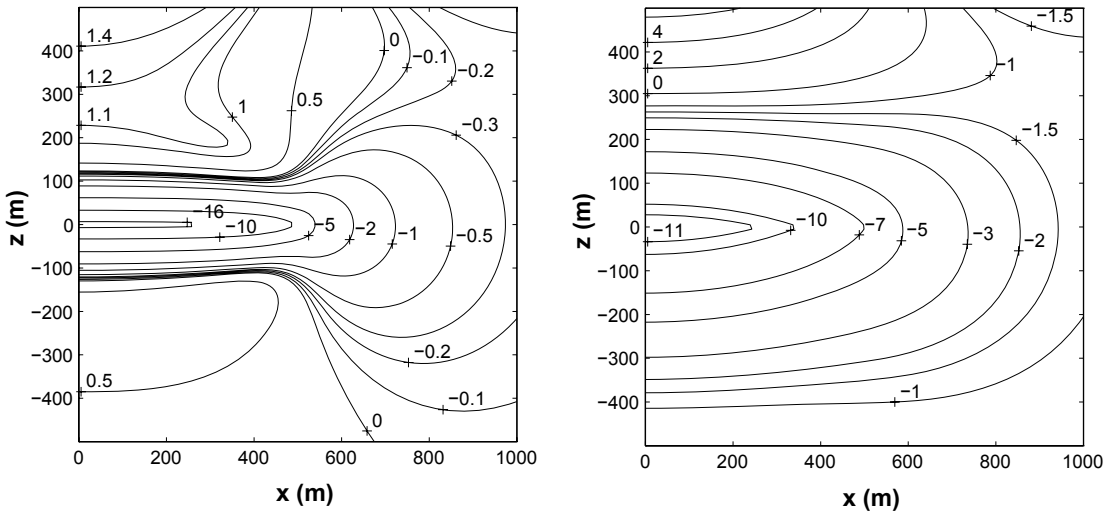

Figure 7-1. *Vertical cross section through generic, square-shaped 1,000 m x 1,000 m repository at 500 m depth with approximately the same heat generation as in the 3DEC models. The contours show horizontal thermal stress σ_x after 50 years (left) and after 1,000 years (right). Tension (positive) is found at varying distances above and below the repository (From /Probert and Claesson 1997b/).*

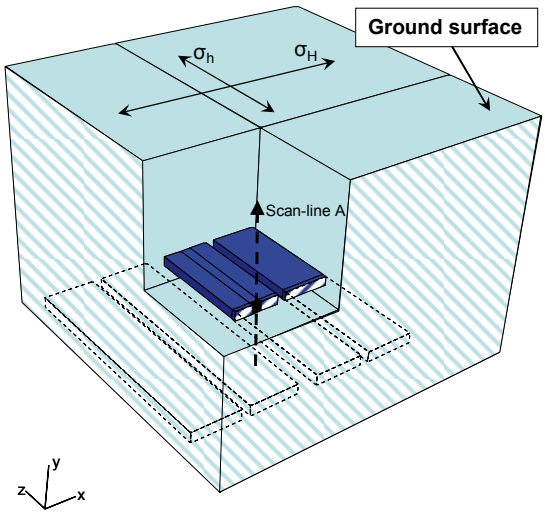

Figure 7-2. *Vertical scan line in large-scale 3DEC model. Orientation of horizontal in situ principal stresses assumed as shown on top of the model.*

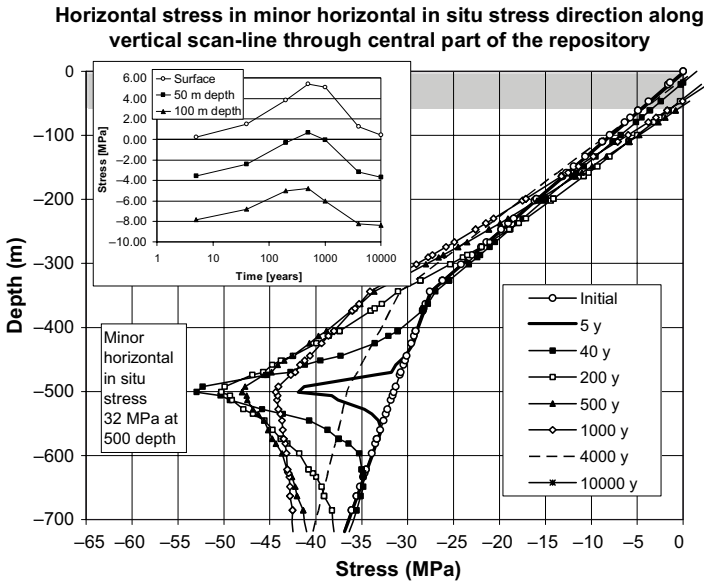

Figure 7-3. *Forsmark: Scan-line minor horizontal stress at different times. Initial stresses as in /SKB 2005b/. Note that compressive stresses are negative here. The insert shows the stress as function of time at three different depths.*

Figure 7-5 shows corresponding results for a stress-depth relation given in draft versions of the Forsmark site description. The minor horizontal stress, "initial", was assumed to be significantly smaller, giving tension down to a depth of about 80 m.

The grey-shaded regions in Figure 7-3 and Figure 7-5 denote the depth of possible tension. In reality, the horizontal stress will be approximately zero (rather than tensile) in these near-surface parts because of rock fractures with low or zero tensile strength. The tension depth difference found between the results shown in Figure 7-3 and Figure 7-5 is due to the difference in assumed initial minor horizontal stress only. Figure 7-6 shows the effect of depositing at 400 m depth rather than 500 m for one of the initial stress assumptions considered above. These results were obtained by use of the analytical solutions given by /Claesson and Probert 1996/. The left part verifies nicely corresponding 3DEC results shown in Figure 7-3. The right part shows that the conditions in the upper part are hardly influenced by the smaller deposition depth.

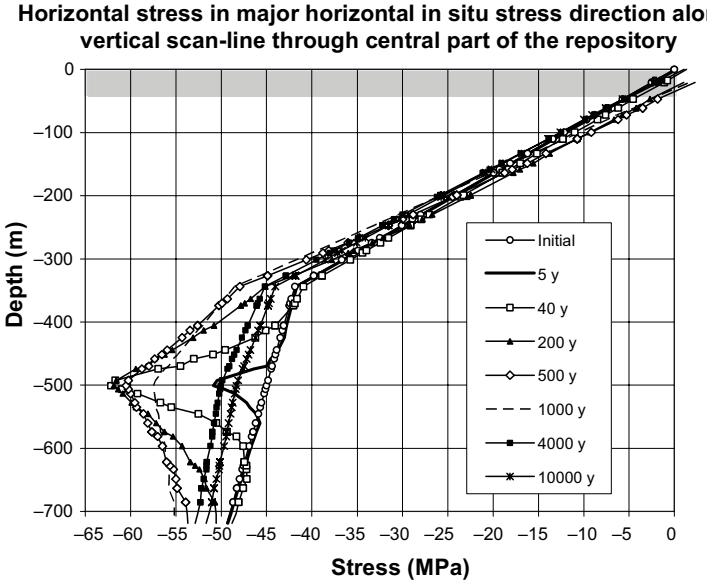

Figure 7-4. *Forsmark: Scan-line major horizontal stress at different times. Initial stresses as in /SKB 2005b/.*

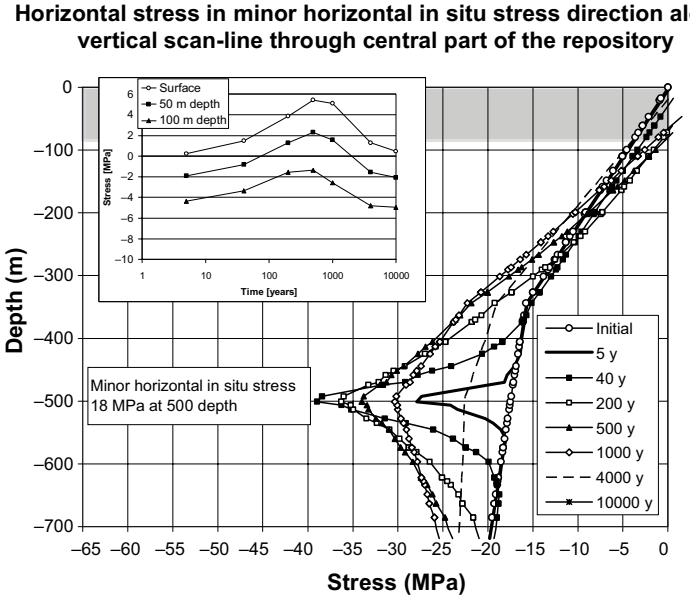

Figure 7-5. *Forsmark: Scan-line minor horizontal stress at different times for draft site model version of minor initial horizontal stress. The insert shows stress as function of time at three different depths.*

The initial stresses assumed in this section are based on data given for depths below 350 m /SKB 2005b/. The top parts of the bilinear relations are interpolations between the ground surface and that depth, assuming the horizontal stresses to be zero at the surface. In reality the stress gradients in the upper part may be disturbed by gently dipping fracture zones and are not necessarily linear as assumed here and the horizontal stresses are not necessarily zero at the ground surface. For the transmissivity estimates made in following sections, this uncertainty may be important at shallow depths because of the sensitivity of the transmissivity to stress variations for fractures in low compression (cf Chapter 2). At shallow depths, however, the stresses are likely to be underestimated rather than overestimated, which would mean that some of the increase in transmissivity found at shallow depths, in following sections may be overestimated. For the general conclusions this does not appear to be important.

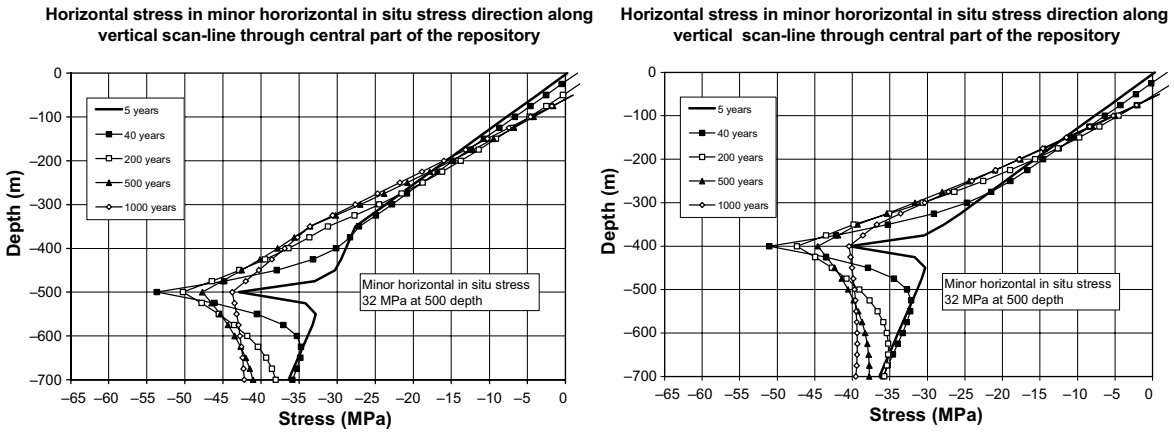

Figure 7-6. *Effects of depositing at 400 m depth (right) rather than 500 m (left)*

7.1.2 Effects of normal load variations on transmissivities

Figure 7-7 and Figure 7-8 show relative transmissivities for differently striking vertical fractures, calculated using the stress-transmissivity relation suggested by /Derschowitz et al. 1991/ (cf Chapter 2). The transmissivities relate to vertical fractures that are parallel with (Figure 7-7) and normal to (Figure 7-8) the major horizontal stress, respectively. The stress changes shown in Figure 7-3 and Figure 7-4, i.e. the horizontal stresses on a vertical scan-line through the central parts of the repository, were used as input. The uppermost 100 m, where tension (or rather, very small horizontal stresses) may be found after about 50 years, was ignored.

Transmissivities increase in the upper parts, in particular from about 40 years after deposition and onwards. There is a maximum after about 500 years, whereas the conditions begin to approach the initial ones after some 1,000 years. However, the effects appear to be modest. Below a depth of 200 m, the increase was at most 10% (after 200 years). In general, the transmissivities decrease, in particular within a few 100 m below and above the repository horizon.

Figure 7-9 shows corresponding results for a case of lower initial stresses (cf Figure 7-5). The transmissivity increase in the upper part is larger, but still less than 25% at all depths larger than 200 m.

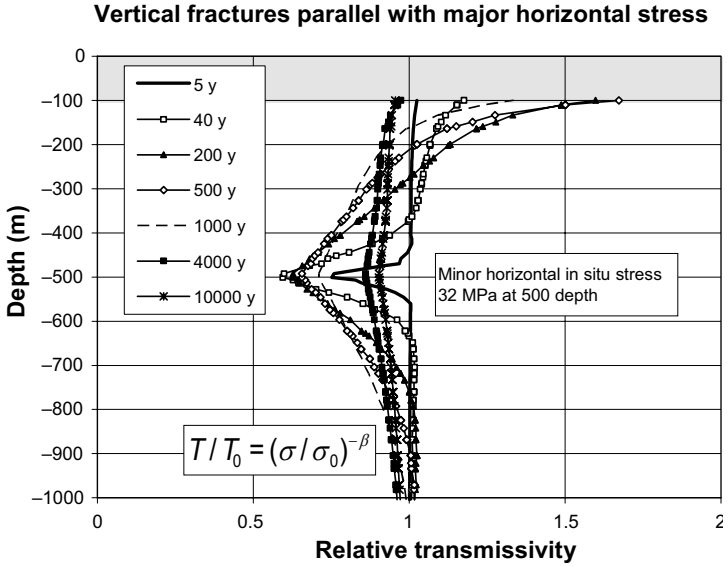

Figure 7-7. *Relative transmissivity of vertical fractures parallel with major horizontal stress (β = 1).*

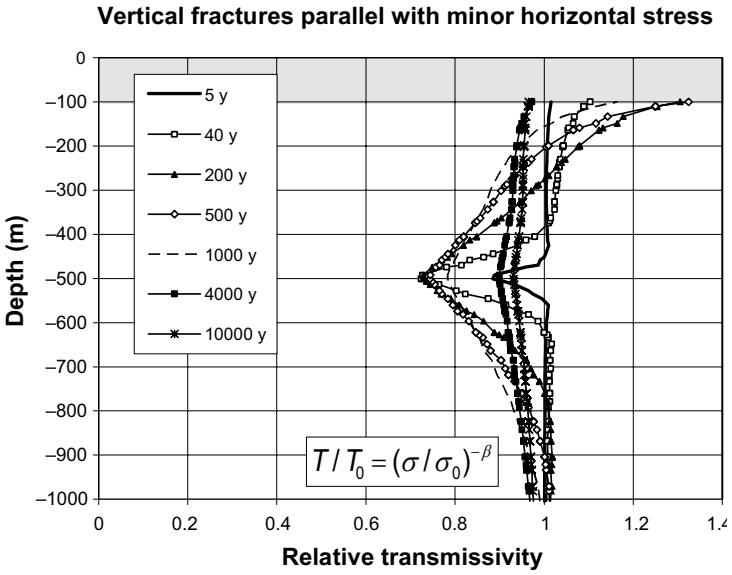

***Figure 7-8**. Relative transmissivity of vertical fractures parallel with minor horizontal stress (β = 1).*

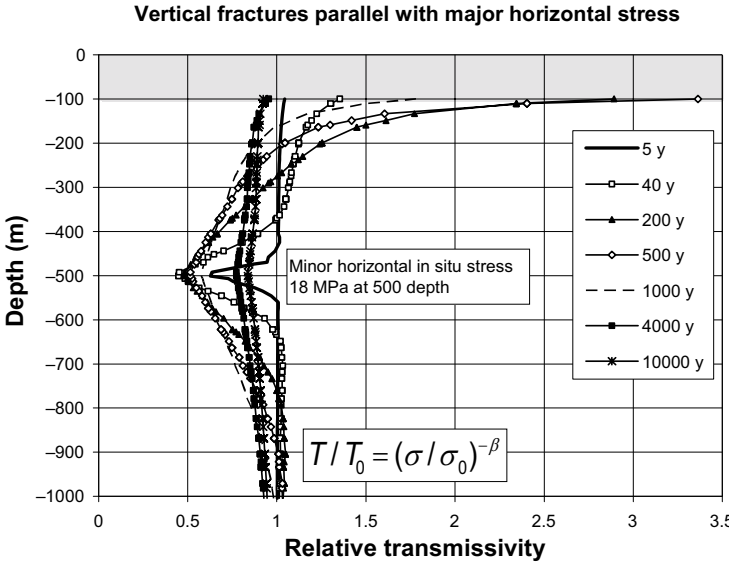

***Figure 7-9**. Relative transmissivity of vertical fractures parallel with major horizontal stress (β = 1).*

The stress-transmissivity law applied here (i.e. the one suggested by /Dershowitz et al. 1991/ does not consider residual apertures or residual transmissivities at high stresses, meaning that part of the transmissivity reduction calculated between 300 m and 800 m (Figure 7-7, Figure 7-8 and Figure 7-9) is an effect of applying that stress-transmissivity relation outside its range of validity. Figure 7-10 shows transmissivities after 200 years, calculated, for comparison, also by use of the stress-aperture law suggested for Sellafield fractures /Liu et al. 2003/ together with the cubic flow law (cf Chapter 2). There are two sets of parameter values for both stress-transmissivity laws.

Except for the overestimated closure effects at repository depth, the two different stress-transmissivity relations give similar results, i.e. modest effects on fracture transmissivities between 100 m and 300 m depth and reduced or unchanged transmissivities at all depths below 300 m.

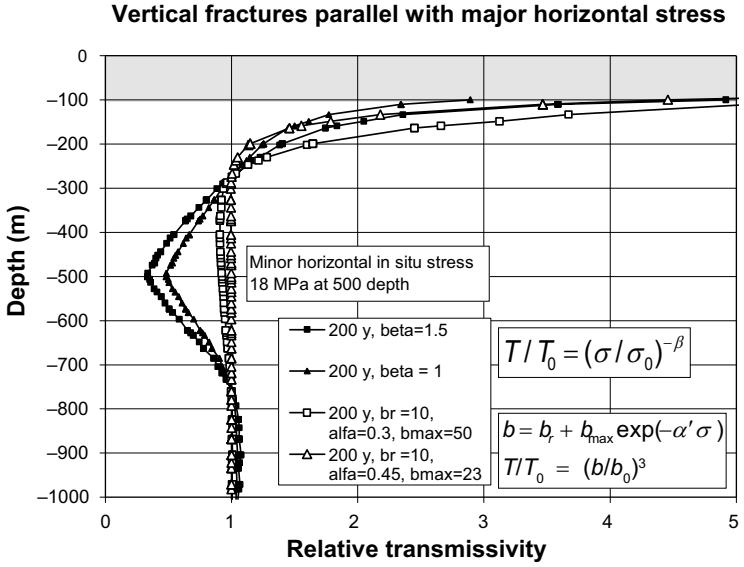

Figure 7-10*. Relative transmissivity of vertical fractures after 200 years for different stress-transmissivity models. The fractures are assumed to be parallel with the major horizontal stress. Initial stress as in Figure 7-9.*

7.2 Glaciation cycle

7.2.1 Upper crust stresses

Figure 7-11 (upper) shows the vertical load generated by the most recent glaciation on a NE-SE scan-line across the Baltic Shield according to Lambeck's 1998 ice model /SKB 2006c/, (B Lund, Dep. of Earth Sciences, Uppsala University, personal communication, 2005). Figure 7-11a, b and c show ice-load induced stress additions 500 m below the ground surface at 800, 1,500 and 1,800 km distance from the NW ice edge, respectively. Horizontal stress additions obtained from the FEM crust stress field analysis are adjusted in accordance with the elastic properties of the top layers of the crust and with the crust compressibility (cf Section 4.6.1). The possibility that the ice-load might be higher is, however, not considered here.

800 km from the NW edge all stress additions are compressive, giving increased or unchanged normal stresses on all fractures.

1,500 from the NW edge there is a 2–4 MPa decrease (approximately) in horizontal stresses after the period of actual ice-cover. Steeply dipping fractures will lose some compression.

Outside the range of the ice cover, in the forebulge region 1,800 km from the NW edge, stress additions are tensile in the upper crust similar to the conditions close to the edge at 1,500 km distance. This gives normal stress reductions of 2–3 MPa on steeply dipping fractures.

7.2.2 Effects on fracture transmissivities

The largest normal stress reduction found in the previous section is about 4 MPa (cf Figure 7-11b). Figure 7-12 shows corresponding transmissivity effects on steeply dipping fractures that are aligned with the present-day in situ horizontal principal stresses. The Forsmark stresses and the Laxemar (Domain I) stresses are used as examples. Results are shown for two of the stress-transmissivity models described in previous sections. The (worst case) 4 MPa stress reduction (Figure 7-11b) was applied in the major horizontal stress direction. In the minor horizontal stress direction the reduction was set to 2 MPa.

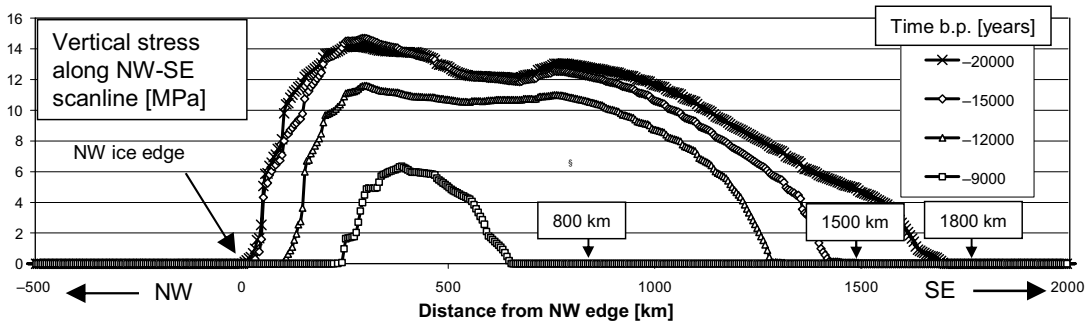

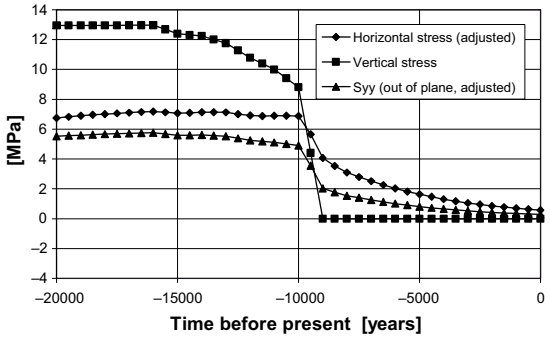

Stress additions 500 m below ground surface 800 km from the NW ice edge.

Increased compression of all fractures at all times.

a)

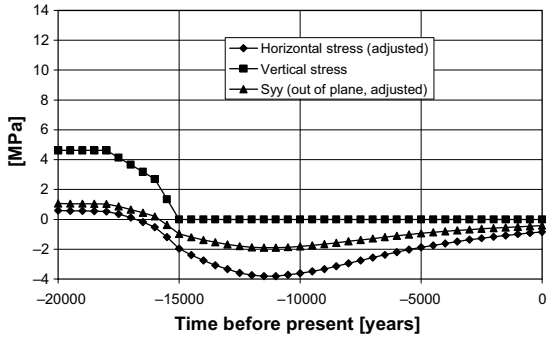

Stress additions 500 m below ground surface 1500 km from the NW ice edge.

2–4 MPa decompression of steeply dipping fractures after ice edge has passed.

b)

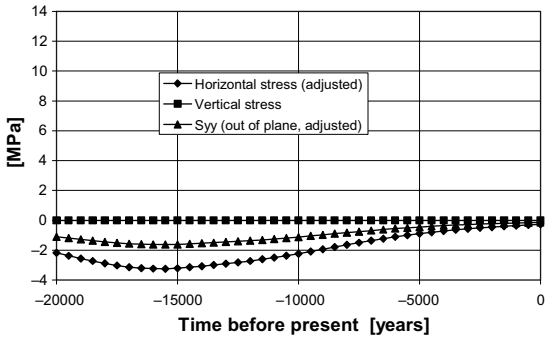

Stress additions 500 m below ground surface 1800 km from the NW ice edge.

2–3 MPa decompression of steeply dipping fractures some 5000 years before final disappearance of the ice.

c)

Figure 7-11. *Upper: vertical load on NW-SE scan-line through the Baltic Shield. a), b and c): stress evolution at 500 m depth at different distances from NW edge. Positive sign means increased compression.*

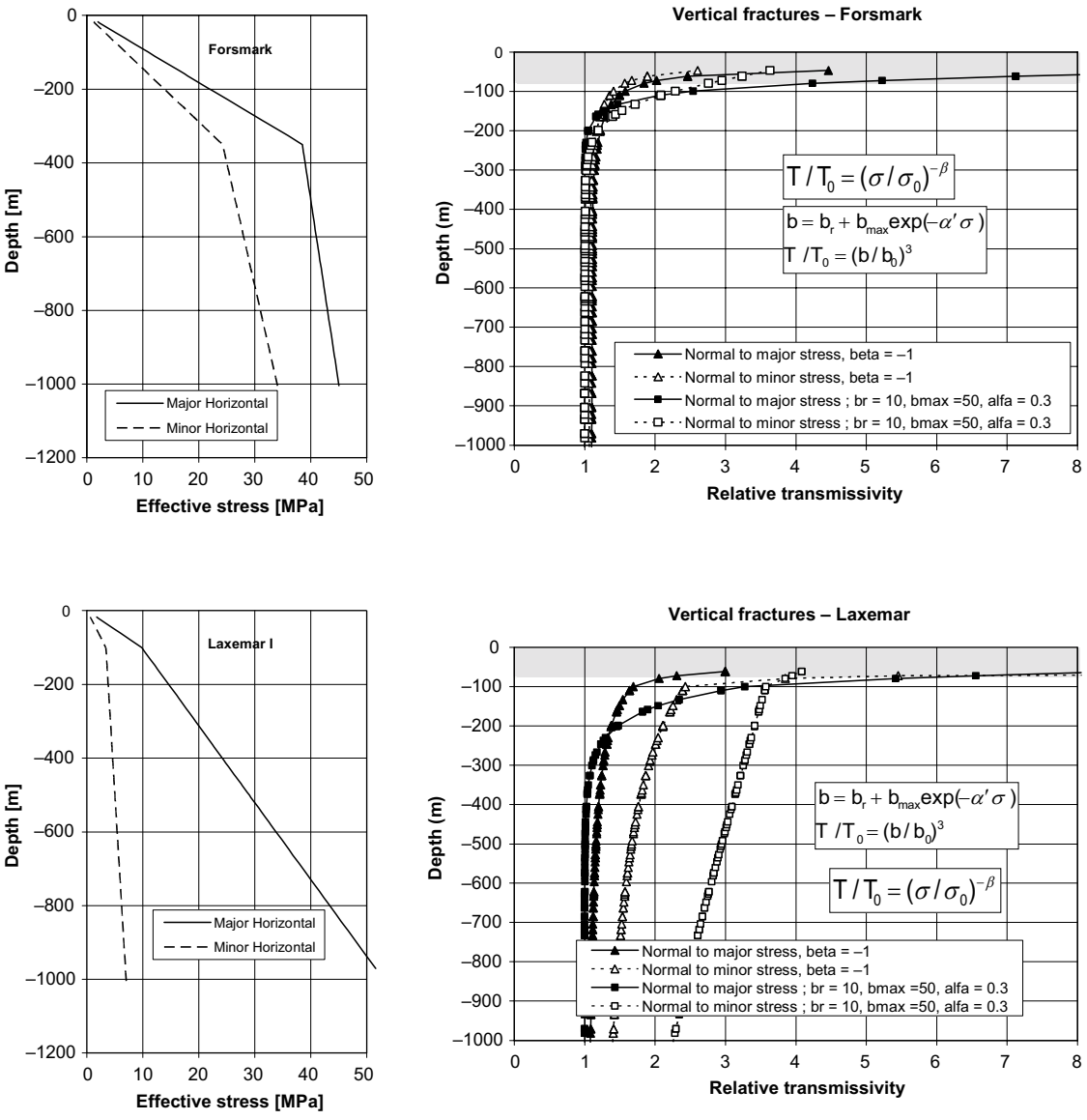

***Figure 7-12**. Transmissivity effects of horizontal stress reduction on steeply dipping fractures in Forsmark and Laxemar. The left parts show present-day stress/depth relations derived from the site descriptions (here compressive stresses are positive).*

The grey-shaded bands indicate the depth region in which horizontal effective stresses approach zero and where transmissivity effects become uncertain. At 150 m depth the transmissivity increased by, at most, a factor of 2 for Forsmark, and a factor of 3.5 for Laxemar. At 400 m depth the increase was negligible for Forsmark and a factor of 3 for Laxemar.

The Laxemar (and Simpevarp) Stress Domain II is believed to be localized in a wedge-shaped region between large deformation zones /SKB 2005a/ and is characterized by low stresses. The wedge geometry and the strength and stiffness properties of the deformation zones control the mechanical interaction between the wedge and the surrounding rock mass such that regional changes in the stress state are not likely to be fully transferred to the Domain II rock mass. Therefore it is not meaningful to analyze effects of a regional-scale 4.0 MPa horizontal stress reduction.

The above shows that transmissivity changes induced by relaxation of fracture normal stresses during the glacial cycle will be modest for the assumptions made here regarding glacial load stresses (cf Figure 7-11b). However, in Laxemar slightly larger stress reductions in the forebulge region would mean considerably more severe effects on steeply dipping fractures with strike along the major stress. In Forsmark the fracture normal effective stresses are sufficiently high that the results (Figure 7-12, upper) are not sensitive to variations in horizontal stress.

Contrary to normal stress effects, possible changes in fracture transmissivities caused by shear displacements are very difficult to estimate. The picture of the stress evolution in the upper crust given in Figure 7-11 above indicates that shear displacements will be promoted after the retreat of the ice at the 800 km edge distance (Figure 7-11a). Here, the typical present-day stress anisotropy with high horizontal stresses and low vertical stress is increased because of a 4 MPa horizontal residual stress addition. This means a 4 MPa deviatoric stress increase (cf Figure 4-12, left) and 2 MPa increase in shear stress for correspondingly oriented fractures. Considering the present-day stresses below 200 m, this modest shear stress increase for a limited fraction of the fracture population seems to be too small to cause significant and systematic shear displacements. Slip magnitudes during the glacial cycle may however be influenced also by possible pore pressure variations, and are estimated in the following chapter. Irrespective of the slip magnitudes, large-scale shear displacements will take place under significantly higher normal stresses, tens of MPa, than those applied in hydro-mechanical laboratory-scale shear tests. In the experiments reported by /Olsson 1998/, for instance, the fracture normal stress was 4 MPa at maximum (cf Figure 2-8). The experiments showed that the sensitivity of the results to normal stress variations was very significant. This suggests that relative transmissivity effects on large-scale slipping fractures will be much smaller than those found experimentally in the laboratory.

8 Hydro-mechanical glaciation studies

8.1 General

Ice sheets have the potential to strongly influence the geosphere, by altering both the mechanical and the hydraulic boundary conditions. The response of the Earth to an applied ice load is determined by the Earth's rheological structure. Due to the long time spans involved in a glacial cycle both elastic and viscous deformation will occur. The lithosphere is generally regarded as an elastic plate overlying a viscoelastic mantle /Lund 2005a, SKB 2006c/.

The load imposed by the ice sheet on the underlying bedrock leads, on the large scale, to downwarping under the ice sheet and upwarping on the margins of the depression (forebulge). This results in the development of bending stresses in the crust. A calculated stress history based on a reconstruction of the last glaciation/deglaciation cycle is presented in Sections 4.6 and 7.2. On a small scale the transient load of the ice sheet will cause an overall increase in total stresses, and an increased confinement.

Groundwater flow beneath ice sheets will be driven by two processes /Boulton et al. 1995/:

- The consolidation of the bedrock due to the ice sheet loading will cause an increase in pore pressure and an expulsion of water yielding a flux.
- Recharge of meltwaters from the ice sheet, available at the bed interface.

These new boundary conditions for groundwater flow during glacial conditions may have the ability to create larger hydraulic gradients than would a present day groundwater system, which in principle is governed by the groundwater recharge and the topographical relief.

The combination of load from the ice sheet and increased pore pressures means that the effective stress is generally affected in two different ways:

- An increase in total stress due to the mechanical loading of the ice sheet leads to an increase in effective stress; and
- An increase in pore pressure due to glaciation leads to a decrease in effective stress.

Coupled hydraulic and mechanical processes that may be of importance for the performance and safety of the deep repository are shear or tensile failures induced by elevated fluid pressures and transient changes in fracture transmissivities due to temporal variations in load and hydraulic pressure.

8.2 Effects on permeability

When rock fractures are subject to changes in mechanical loading during glaciation, their hydraulic apertures will change, which will lead to increased or decreased transmissivity/ permeability (see Chapter 2). Enhanced fluid pressure in a single fracture decreases the effective normal stress across the fracture leading to fracture widening. The result is a counter-balancing effect between total mechanical stress and pore pressure, and the resulting transmissivity change is expected to be fully elastic. Transmissivity changes induced during a glaciation period, as predicted by 3DEC models, are presented in Chapter 5. This type of H-M effect of glaciation will not be further described here.

The initial rock mass permeability may also be altered as a secondary effect of hydraulic jacking or shearing induced by the glaciation. /Boulton and Caban 1995/ argued that rock mass permeability beneath an ice sheet must be considered as time-dependent and self-organising.

An excess of glacial melt-water in combination with low sub-glacial permeabilities may induce pressures up to the magnitude of the limiting pressure set by the ice sheet thickness. The pressure gradients are determined by the slope of the ice sheet surface and by the presence of conductive features in the sub-glacial hydrological system at the ice/bed interface. A detailed description of glacial hydrology can be found in /SKB 2005c/.

Hydraulic jacking occurs when groundwater pressures in the fractured bedrock exceed the value of the minimum rock stress. These tensile failures may increase the permeability of the rock and thereby reduce groundwater pressures until a balance between recharge and permeability is reached. However, in this context it should be noted that the greatest potential for permeability increase exists in the sub-glacial sediments at the ice/bed interface.

/Boulton and Caban 1995/ also discussed the potential role of proglacial permafrost for the development of hydraulic fracturing. Since the permafrost layer has a very low permeability, the infiltration of glacial meltwater into the groundwater aquifer is prevented and high water pressures may occur in the area beyond the extent of the ice sheet where there is no increase in vertical stress due to the ice load.

8.3 Mechanical effects of high pore pressures

8.3.1 Hydraulic jacking

Hydraulic jacking of a fracture is initiated when the effective normal stress across the fracture becomes tensile, on condition that the fracture has no tensile strength. This is the same mechanism as hydraulic fracturing, which is a standard operation in the petroleum industry carried out in wells for improving oil or gas recovery from reservoir rocks. The technique is also used for stress measurement both by hydraulically creating new fractures and by jacking open existing fractures. Large-scale hydraulic stimulations are also carried out in geothermal energy projects where pressurised fluid is injected in fractured crystalline rock masses in order to create increased rock mass permeability.

/Lindblom 1997/ presented analytical calculations of the potential for hydraulic jacking of fractures in the rock mass in different positions in relation to an ice sheet front.

The first situation studied by Lindblom was a rock mass located under the ice sheet far from the ice sheet margin. Assuming a hydraulic head corresponding to the ice sheet thickness, Lindblom suggested that hydraulic jacking of horizontal fractures may occur to a depth of $h_{ice}/16$. For a 1,000 m thick ice, this means a depth of about 60 m.

The second, and more interesting, case studied by Lindblom, was a frontal position of a retreating ice sheet, where the situation in the rock mass outside the margin of the ice sheet was analysed. Based on the assumption that the vertical total stress has returned to its non-glacial magnitude, whereas the groundwater pressure in the rock pores and fractures for some reason remains enhanced corresponding to the top level of the ice sheet, he derived an expression for the groundwater pressure required to produce jacking. Lindblom concluded that 800 m of ice would be sufficient to produce jacking of fractures at 500 m depth (i.e. ice thickness divided by 1.6). However, a necessary condition for this to occur, which is not discussed by Lindblom, is that the hydraulic pressure must be transmitted without losses over a long horizontal distance from a position under the ice sheet to a position at the ice sheet front.

Numerical mechanical and hydraulic modelling by /Pusch et al. 1990/ suggested, for a similar situation to Lindblom's second case, that water flowing in the rock mass 1 km behind a 200 m high ice front is capable of lifting a rock slab about 30 m thick. On the basis of these modelling results /Talbot 1999/ argued that water pressures beneath a 3,500 m thick ice can "lift" between 500 m and 1,000 m of rock (Figure 8-1).

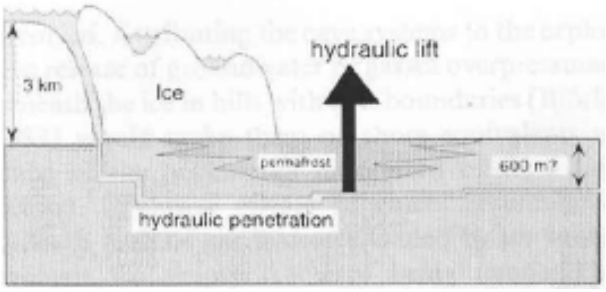

Figure 8-1. *Principles of jacking at large depth. From /Talbot 1999/.*

Talbot's arguments are, however, not realistic, when considering the shape of an ice sheet, the thermal and hydrological conditions beneath an ice sheet and the geometry and transmissivity of existing rock fracture systems.

Theoretically hydraulic jacking can occur at great depth if specific conditions are fulfilled. The conditions promoting such a situation are:

- A steep slope of the ice-sheet front;
- High meltwater pressures at the ice-sheet bed;
- Conductive steeply dipping rock fractures beneath the part of the ice sheet that is melting;
- Horizontal or shallowly dipping high-permeable rock fractures leading towards a position beyond the ice margin
- Low permeability rock mass with few connecting conducting fractures that could disturb the long-distance horizontal pressure transfer.

From the hydrological perspective, the most critical conditions occur during deglaciation. However, a retreating ice sheet is expected to have a rather flat profile, compared with an advancing or steady-state ice sheet. For example, ice-sheet modelling carried out with the University of Maine Ice Sheet Model (J-O Näslund, SKB, personal communication, 2006) shows that an ice thickness of 200 m, which could be sufficient to give rise to water pressures high enough to induce hydraulic jacking beyond the ice front at 125 m depth, during deglaciation is not expected closer than some kilometres from the ice margin. This calculation presupposes that the basal water pressure head is equal to the ice thickness.

However, it can not be completely ruled out that melting conditions giving rise to high sub-glacial water pressures can occur also during specific phases of the ice sheet advance when the slope of the ice sheet is much steeper. This may theoretically lead to potential jacking at larger depths. A calculation of the shape of a steady-state ice sheet /Patterson 1994/ gives an ice thickness of 350 m at a distance of 1,000 m from the margin. This thickness implies that a critical depth where jacking can occur is about 220 m, with the same assumptions as above.

In order for the hydraulic pressure to be transmitted through the rock mass over such a distance, horizontal or sub-horizontal connective fractures of great lengths and widths are required. Connecting permeable fractures in all directions, as well as friction losses, would in reality significantly reduce the fluid pressure. Neither Forsmark nor Laxemar seem to have geological/hydrogeological conditions favouring the initiation of hydraulic jacking at depth.

If conditions for hydraulic jacking are fulfilled this is likely to occur at shallow depths in the first place. This will in turn act to reduce pressures so that jacking at larger depths becomes less likely.

Evidence or at least strong indications for such glacial/postglacial hydraulic jacking events can be found down to some tens of metres in the crystalline bedrock at several sites in Sweden (for instance the Forsmark site) where drillhole records and excavations show subhorizontal fractures, filled with sediments. It is likely that the jacking effect will be preserved by the high density and viscosity of a meltwater/sediment slurry. The depths at which the observations have been made are in accordance with the discussion above.

Under the ice cover the mechanical vertical load can be assumed to be sufficient to balance effects of increased pore pressures, which means that effective stress variations on horizontal and subhorizontal fractures will give only insignificant effects on fracture transmissivities. For steeply dipping fractures, however, high pore pressures may cause very significant transmissivity increases at large depths if the horizontal stresses do not increase correspondingly. The ice load stress model suggested in Figure 4-12 (right), i.e. with a vertical load of 25 MPa and horizontal stress additions of about 11 and 14 MP in the two principal directions, would increase the transmissivities in Forsmark very significantly down to 200 m depth if the pore pressure increased by about 90% of the ice load (Figure 8-2). Below 300 m the transmissivity would increase by less than factor of 2.

For the ice-load stress model suggested in Figure 4-10 the effective normal stress on all fractures, vertical and horizontal, would increase with slightly reduced transmissivities as a result.

With respect to transmissivity increase of steeply dipping fractures, the Laxemar site with lower in situ stresses than Forsmark is more sensitive to assumptions made regarding horizontal stress additions during the period of ice load and high pore pressures. Applying the stress/pressure assumptions shown for Forsmark in Figure 8-2 to the Laxemar site would give zero effective stress down to the repository depth and below. However, the ice stress model used to estimate the horizontal stress additions is a very schematic one, based on oversimplified and preliminary ice-crust-mantle analyses (cf Section 4.6). This points to the need for more elaborated analyses with reasonably realistic assumptions regarding crust compressibility and stiffness/depth relations (cf Chapter 9).

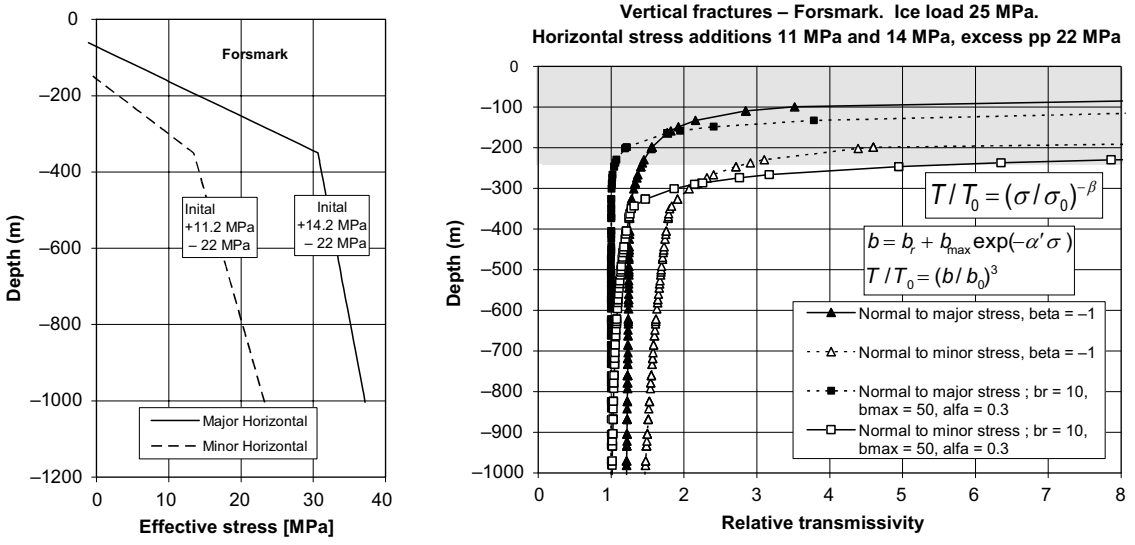

Figure 8-2. *Left: effective horizontal stresses assuming 25 MPa vertical ice load and 22 MPa excess pore pressure. Right: transmissivity effects on steeply dipping fractures. The grey-shaded band indicates region in which stresses approach zero and transmissivity estimates become uncertain.*

8.3.2 Hydraulic shearing

The theory of hydraulic shearing of fractured bedrock has been described by e.g. /Pine and Batchelor 1984/, and adopted primarily for situations when fluid under pressure is injected in a borehole /e.g. Wallroth 1992/.

Injection of pressurized fluid into a rock fracture reduces the effective normal stress and shearing is initiated if the pressure is sufficiently high. The critical fluid pressure P_c required to induce failure depends on the in situ stress field, the fracture orientation and the fracture shear strength, and can be illustrated in a Mohr circle diagram (see Figure 8-3).

In this case, a linear Mohr-Coulomb shear strength criterion has been used. P_c can be expressed as:

$$P_c = \sigma_n - \tau / \tan \varphi \qquad (8\text{-}1)$$

where σ_n is the normal stress, τ the shear stress and φ the total friction angle.

The plane most likely to slip is the one with the largest ratio of shear to normal stress. The most critical plane is hence found for $\theta = (90–\varphi)/ 2$. For a state of stress with roughly vertical-horizontal principal stresses, the most critical fracture orientation is vertical if the minimum stress is horizontal and shallowly dipping if the minimum stress is vertical.

By inserting stress magnitudes measured at the Forsmark site investigations into the equation above, one finds that even small changes in pore pressure are sufficient to initiate shear failure, given that critically oriented fracture planes exist in the rock mass.

At 500 m depth in Forsmark, the major horizontal stress is about 45 MPa and the minor stress (vertical) is 13 MPa /SKB 2005b/. This means that the largest shear to normal stress ratio is found on planes dipping 28.3 degrees. If the pore pressure is 5 MPa, fractures with that dip need to have a friction angle of 41.5 degrees to be stable. Figure 8-4 shows analytically calculated shear displacements following failure caused by pore pressure increases for fractures having the most unfavourable dip (28.3 degrees) and for fractures dipping 40 degrees. The critical failure pore pressure for the two fracture orientations equals the hydrostatic 5 MPa pressure and (about)

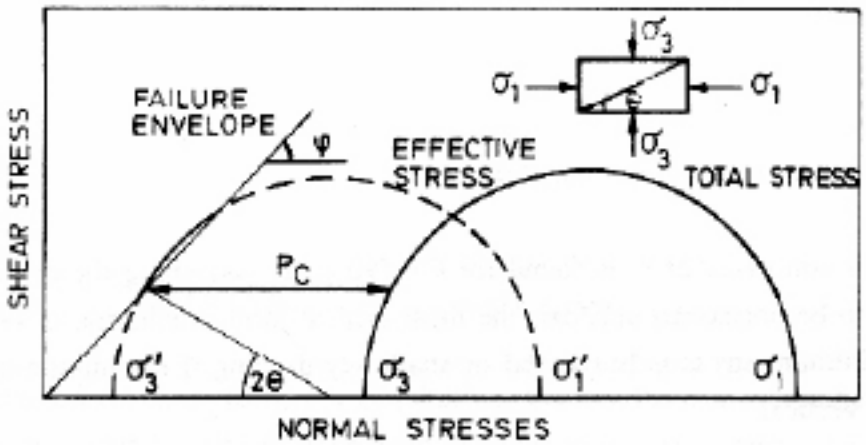

Figure 8-3. *Mohr diagram showing the influence of fluid pressure P_c on the conditions for shear failure along plane θ. Note: there will be shear failure along planes in the 2θ range defined by the two failure envelope intersections.*

8 MPa, respectively. The shear displacement is about 4.5 mm for each MPa of pore pressure above the failure limit for the large 300 m diameter fracture, and about 1.5 mm/MPa for the smaller 100 m diameter fracture. The analytical solution reads /Itasca 1992/:

$$u_s = \frac{2(1-\nu)}{G} \cdot \tau_{drop} \cdot a \qquad (8\text{-}2)$$

Here, u_s is the shear displacement, at the centre of the fracture, while v and G are Poisson's ratio and the shear modulus, respectively, of the elastic surrounding rock. The stress drop τ_{drop} is the difference between the nominal shear stress acting on the plane of the fracture and the fracture shear strength. The expression is valid for 2-D fractures of infinite extension in the out-of-plane direction and with in-plane half-length a /Itasca 1992/. For circular fractures with radius a, the 2-D shear displacements obtained from Equation 8-2 must be multiplied by a factor of 0.7 /Hakami and Olofsson 2002/.

Figure 8-5 shows the same type of result for 30 degree friction angle fractures (which are in a state of failure at the time of the pore pressure increase). Shear displacements are 3 mm/MPa for the large 300 m diameter fracture and 1 mm/MPa for the smaller fracture. For both fracture orientations the fracture shear strength is well exceeded already in the initial, 5 MPa pore pressure state, meaning that additional slip occurs at any pore pressure increment.

Evidence that shear failures can be triggered by fluid injections at rather low pressures exist e.g. from the hot dry rock experiments at Fjällbacka in south-western Sweden /Jupe et al. 1992, Wallroth et al. 1996/. A multitude of microseismic events from shear-slip failures were monitored at fluid pressures between 3 and 4 MPa above hydrostatic pressure. The observations were in accordance with the measured stress situation and orientations of the dominating fracture sets at the site.

Unlike the conditions when fluid under pressure is injected while total stresses are constant, both total stresses and pore pressures are changed with time under the influence of an ice sheet. This means that in order to investigate whether at any time shear failure occurs or not the entire stress and pore pressure history has to be studied (see Sections 8.3.3 and 8.4). During glacial retreat residual elevated pore pressures in the rock mass may help to trigger end-glacial faulting /Lund 2005/ following the same principle as described above.

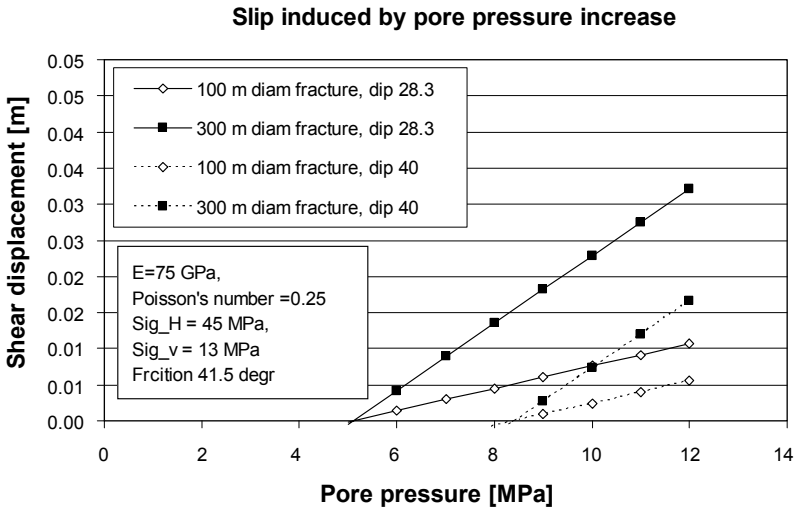

Figure 8-4. *Shear displacement as function of pore pressure for a fracture with 41.5 degree friction angle. Only the fracture with the most unfavourable orientation slips at the first pore pressure increment.*

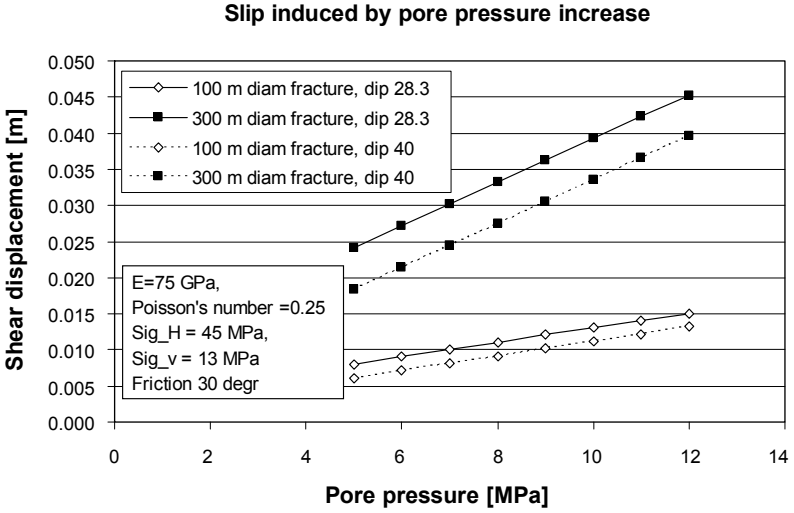

Figure 8-5. *Shear displacement as function of pore pressure for a fracture with 30 degree friction angle. A pore pressure increase from 5 MPa to 12 MPa gives a slip of 7 mm for the small fracture and 21 mm for the large fracture.*

/Lindblom 1997/ applied the theory of hydraulic shearing of fractured bedrock to derive an expression for a so-called augmentation factor of groundwater pressure, required to induce shear failure in the rock mass at different depths. Assuming no ice load and ambient in situ stresses according to a statistical average situation in Scandinavia /Stephansson et al. 1987/, Lindblom calculated critical pressures for hydraulic shearing at different depths and for different friction angles (see Figure 8-6). Since an ice sheet in reality would increase both horizontal and vertical total stresses the calculation does not correspond to a glacial case, neither during ice advance nor retreat. However it is obvious that, when considering an anisotropic state of rock stresses and natural fractures with many different orientations, a relatively small increase in pore pressure is required to induce failure on critically aligned fractures under current conditions. This conclusion is also likely to be valid under glacial conditions.

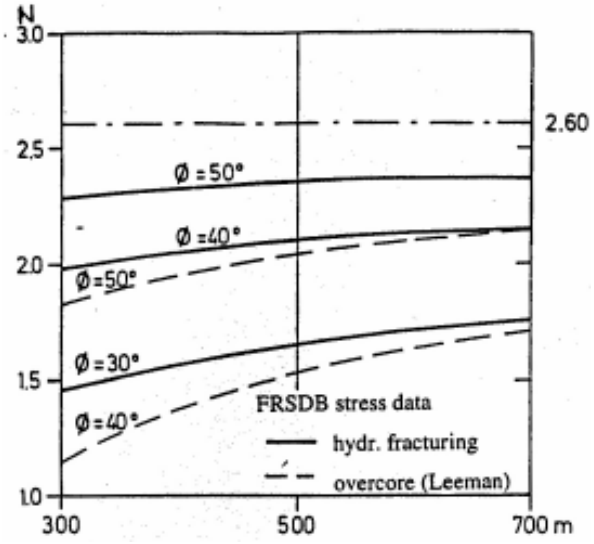

Figure 8-6. *Augmentation factor N for groundwater pressure (relative increase) required to produce shear failure in critically oriented fractures at different depths and for different friction angles. The diagram shows the factors calculated for two different stress data bases /Lindblom 1997/.*

The overcoring relations shown in Figure 8-6 relate to average stress conditions in Swedish bedrock and suggest that it would take 2.5 MPa of pore pressure increase, i.e. 50% above the undisturbed present-day 5 MPa pressure, to produce failure at 500 m depth along 40° friction angle fractures. In Forsmark, with 45 MPa of horizontal stress and 13 MPa of vertical stress at that depth, the potential for hydraulic shearing is much larger, as shown in Figure 8-4 and Figure 8-5.

8.3.3 Shearing under hydro-mechanical glacial load

The previous section concerned effects of pore pressure variations. Significant pore pressure increases are not likely, however, to occur without accompanying changes in mechanical load. This section considers the combined effects of glacially induced changes in mechanical load and pore pressure. Figure 8-7 shows the evolution of the effective stress field (σ_1/σ_3 plane, cf Figure 8-3) at 500 m depth in Forsmark for four different cases:

a) Modified ice-load stresses derived from FEM ice-crust-mantle analysis (cf Figure 4-12, left). The pore pressure is assumed to be constant over time.

b) Same as a), but with increased pore pressures. The excess pore pressure at the time of maximum load is assumed to be 90% of the max mechanical load, i.e. about 11 MPa. When the ice margin passes, the excess pore pressure is assumed to be 25% of the max load, i.e. 3.1 MPa.

c) Ice load stresses assumed to be doubled compared with a) (i.e. according to Figure 4-12, right). Pore pressure is assumed to be constant over time.

d) Same as c), but with increased pore pressures. The excess pore pressure at the time of maximum load is assumed to be 90% of the max mechanical load, i.e. about 22 MPa. When the retreating ice margin passes, the excess pore pressure is assumed to be 25% of the max load, i.e. 6.2 MPa.

The failure envelope included for reference in the Mohr circle diagrams relates to fractures with zero cohesion, zero dilation and a 34 degree friction angle. Fractures dipping between 11 and 44 degrees (in the σ_1/σ_3 plane) are in state of failure already under the initial present-day effective stresses as indicated in the topmost diagram.

Under the ice cover (max load; dotted Mohr circles) the stability improves considerably for all cases. This is particularly true if there is no excess pore pressure. When the ice margin passes, the Mohr circle diameter increases, i.e. the deviatoric stresses increase as shown in Figure 4-13. This extends the dip range of fractures that are in a state of failure, particularly if pore pressures increase (i.e. the Mohr circles move to the left in the diagram, cf Figure 8-3).

An estimate of the magnitude of the slip induced during the glacial cycle can be obtained using Equation 8-2. Figure 8-8 illustrates this for the stress cases in Figure 8-7c and Figure 8-7d. Fractures with different dip angles: 28.6° (worst dip), 43° (just within the present-day failure dip range) and 47° (just outside present-day failure dip range) are analyzed. Figure 8-8a shows slip as function of fracture radius for the assumption that the pore pressure remains at 5 MPa as in Figure 8-7c. Figure 8-8b shows corresponding results for the pore pressure assumption made in Figure 8-7d.

If the pore pressure is constant over time, i.e. unaffected by the ice load, slip magnitudes are about 15 mm at maximum for 400 m diameter fractures, and correspondingly smaller for smaller fractures (Figure 8-8, upper). The fracture with a dip angle just outside the present-day failure dip range (47°) slipped by about 1 mm.

If the pore pressure is increased under the retreating margin, slip magnitudes increase. For the 6.2 MPa excess pressure the maximum slip is about 44 mm for the 400 m diameter fracture.

Pore pressures as high as 11 MPa below the margin of the retreating ice are not likely, as suggested in the hydraulic jacking Section (8.3.1), meaning that the slip estimates made in Figure 8-8 (upper) are probably more relevant than those in Figure 8-8 (lower).

a) and b): ice load stress additions derived from FEM ice-crust-mantle analysis

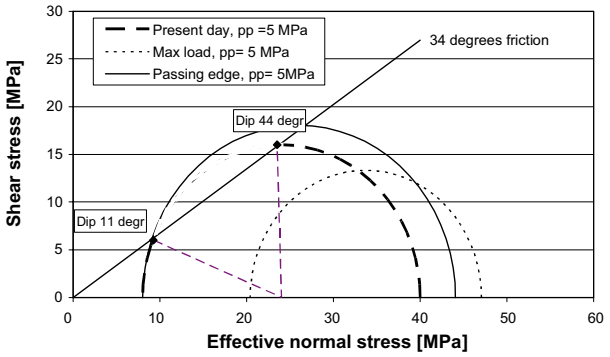

a)

Present day ,
σ_H= 45 MPa,
σ_v= 13 MPa,

Max ice load :
σ_H= 45 + 7.1 = 52.1 MPa
σ_v= 13 + 12.4 MPa = 25.4 MPa

Edge passing :
σ_H=45+4.1 =49.1 MPa
σ_v=13 + 0 MPa = 13 MPa

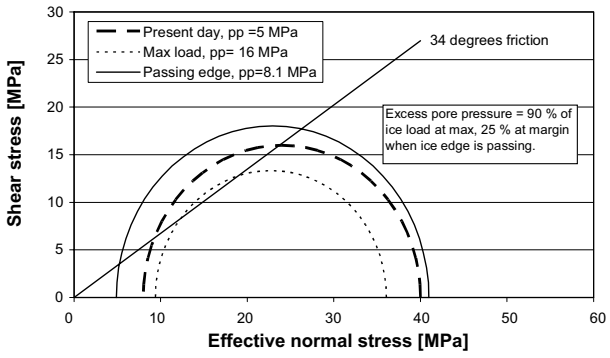

b)

Same stress history as above, i.e. according to the results derived from the ice-crust-mantle FEM analysis but pore pressure assumed to be 16 MPa during max load and 8.1 MPa under the retreating margin. The excess pore pressures reduce the effective normal stresses and move the Mohr circles to the left, giving correspondingly decreased stability.

c) and d): all ice load stress additions doubled

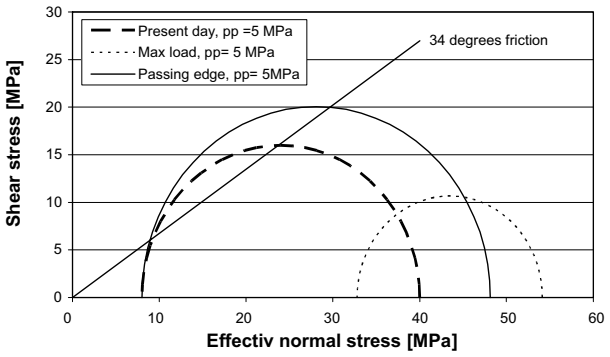

c)

Present day :
σ_H= 45 MPa,
σ_v= 13 MPa,

Max ice load :
σ_H= 45+14.2 = 59.2 MPa
σ_v= 13 + 24.8 MPa = 37.8 MPa

Edge passing
σ_H=45+8.2 =53.2 MPa
σ_v=13 + 0 MPa = 13 MPa

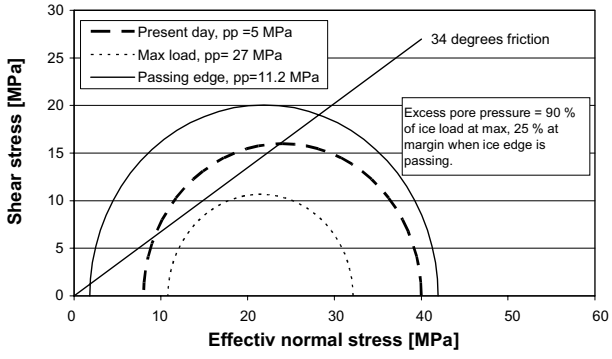

d)

Same stress history as above, but pore pressure assumed to be 27 MPa during max load and 11.2 MPa under the retreating margin. The combination of high stress anisotropy (large Mohr circle diameter) and high pore pressure (Mohr circle offset to the left) under the retreating ice may create potential instability for a large number of differently oriented fractures.

Figure 8-7. *Mohr circle representation of stresses at 500 m depth in Forsmark.*

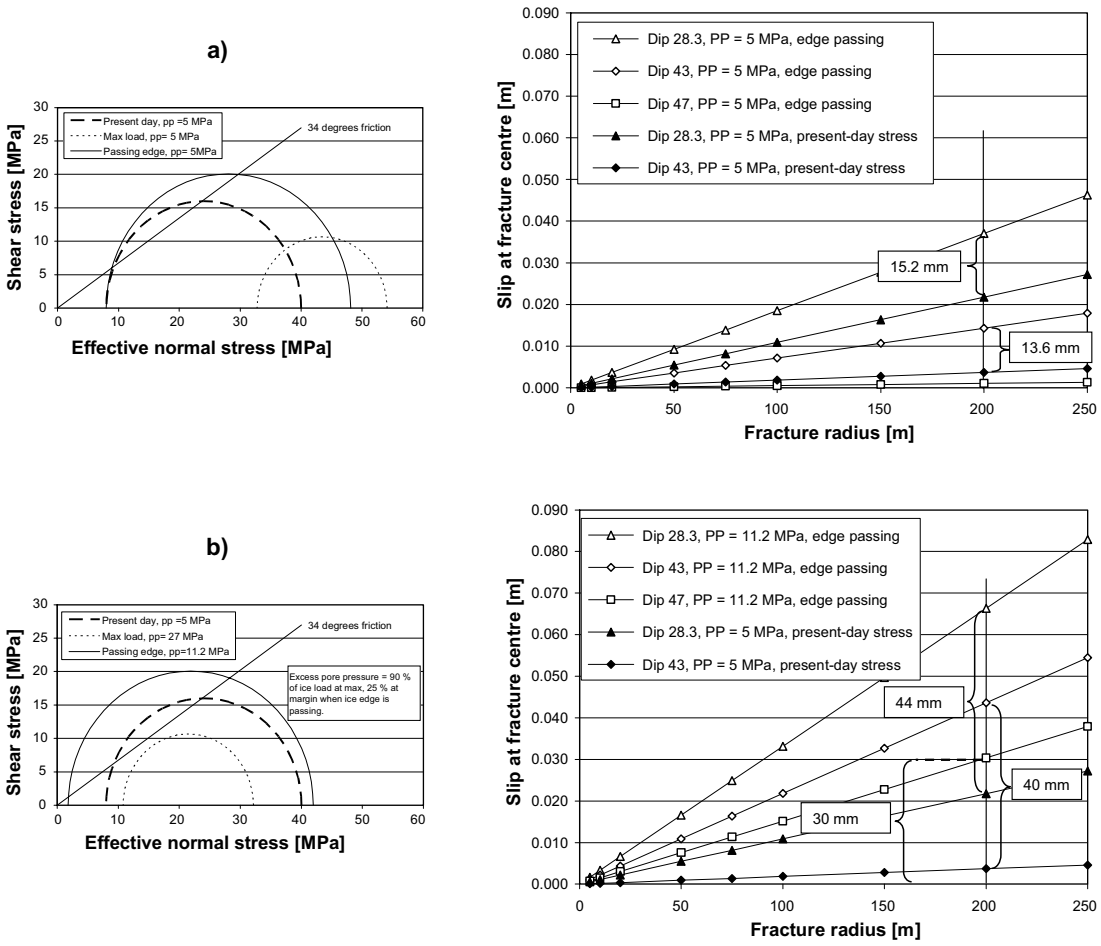

Figure 8-8. *Slip magnitude estimates.*

8.3.4 Effects of jacking and shearing on permeability

When jacking occurs, the fracture surfaces separate from each other and the fracture aperture may increase significantly. Jacking can be expected to continue as long as there are tensile conditions in the fracture. Except for horizontal or subhorizontal fractures close to the ground surface where the overlying rock slabs can potentially be lifted resulting in very large apertures, the maximum aperture resulting from the process is limited by the deformation potential of the rock mass surrounding the dilating fractures. Analytical equations exist for predicting fracture widths resulting from hydraulic fracturing operations in intact rock /e.g. Wallroth 1992/, but these are not directly applicable for estimating fracture widths resulting from hydraulic jacking occurring in a fractured crystalline rock mass. Numerical modelling with discrete fractures can be used for this purpose.

It is generally assumed that the normal dilation resulting from jacking is a reversible process, as long as there is no associated shear component and no solid particles are introduced by the fluid. At the edge of an ice sheet sediments can be expected to be transported into the fractures that are jacked open. In the Forsmark area such sediment-filled fractures have been observed down to a few tens of metres. These fractures show in some cases sediment fillings and apertures > 50 cm /SKB 2005b/.

As described in Chapter 2, during fracture shear movements the mechanical fracture aperture will change because of dilation. The associated change in transmissivity is a function of the shear displacement, but also dependent on the normal stress across the fracture. The latter implies that the higher the normal stress, the less dilation is expected.

8.4 DECOVALEX III glaciation benchmark test

8.4.1 Introduction

As part of the international DECOVALEX III project a benchmark test was designed to explore the mechanical and hydraulic response of a fractured crystalline rock mass to a cycle of glaciation/deglaciation /Chan et al. 2005ab/. A conceptual site-scale hydraulic-mechanical (H-M) model was assembled based primarily on site-specific geological, hydrogeological and rock mechanics data from the Whiteshell Research Area in the Canadian Shield. A large-scale ice sheet/drainage model was used to generate spatially and temporally variable hydraulic and mechanical surface boundary conditions for site-scale subsurface H-M modelling.

The H-M model domain encompassed a volume approximately 25 km × 37 km × 4 km (deep) and consisted of a sparsely fractured rock mass with a number of fracture zones with different orientations. The original structural model from the site was simplified to include 17 fracture zones of uniform thickness (20 m). Twelve of these zones coincided with the vertical boundaries of the model, so that only five zones were located in the interior of the numerical model. A hypothetical, rectangular repository (2 km × 2 km × 10 m) was located at approximately 500 m below the surface in the model. Various configurations and interconnectivity of the fracture zones were considered, the two shown in Figure 8-9 were selected for the simulations in 2-D. In both these configurations there was a horizontal fracture with large extension connected to a vertical zone at the model boundary. In the first case the horizontal zone was connected to the inclined fracture zone whereas in the other case the horizontal zone was dead-ended. The purpose of the latter case was to produce high water pressure in the fracture, to facilitate conditions for potential hydraulic jacking beyond the ice sheet front.

The case shown in Figure 8-9 illustrates a section in the general direction of ice sheet flow at the WRA site, assumed to correspond to the direction of major horizontal compression.

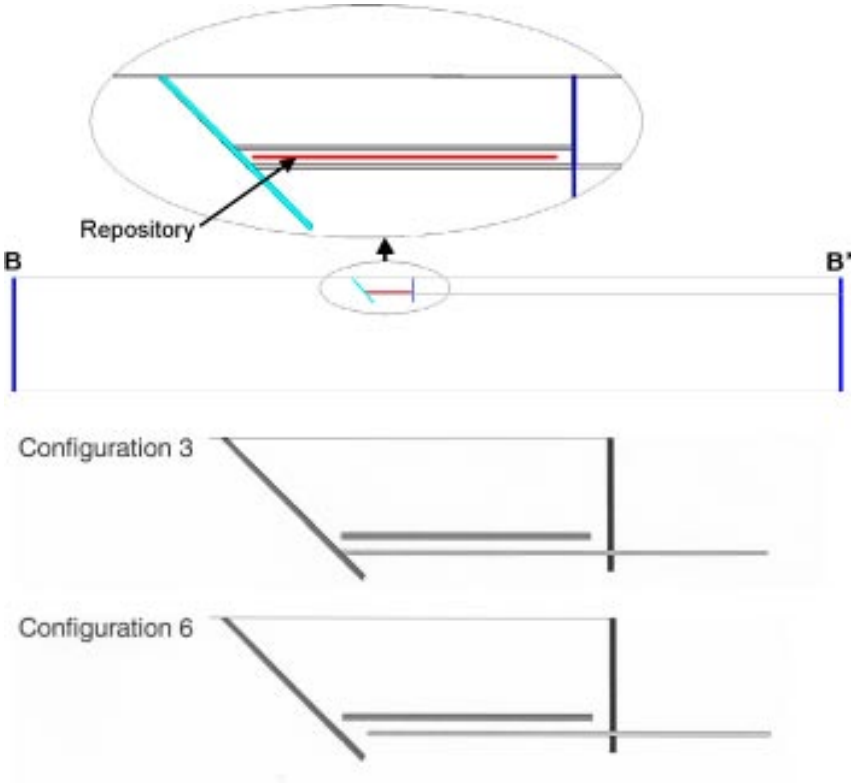

Figure 8-9. *Upper: Vertical model section with 4 fracture planes. Centre and bottom: Detail of two configurations. These particular configurations include only one of the two horizontal fracture zones. (Figures from /Chan et al. 2005a/).*

The transverse section, which was also simulated, is in the direction of the local topographic gradient, also corresponding to the direction of the minimum horizontal stress. The ambient in situ rock stresses at the site are very high, but in the numerical simulations the magnitudes were reduced to represent a mean of Canadian and Fennoscandian stresses.

The hydraulic properties of the rock mass were represented by 13 layers of different permeability, decreasing downwards. At depths greater than 750 m, the permeability was assumed to be as low as 10^{-21} m^2. The fracture zones were also assumed to have permeabilities decreasing with depth. The contrast between the permeability value in the fracture zones and the surrounding rock mass was up to 5 orders of magnitude. Mechanically, both fracture zones and rock mass were assumed to be homogeneous, isotropic and linear elastic.

Two teams carried out site-scale H-M modelling, both using finite element codes. The AECL team representing OPG in Canada, used the code MOTIF /Guvanasen and Chan 2000/. The team from Chalmers University of Technology representing SKB, used the commercial code ABAQUS. The teams performed both 2-D and 3-D modelling.

The bottom boundary of the model domain, at 4 km depth, was assumed to be a no-flow, zero-normal-displacement boundary. The vertical boundaries were assigned hydrostatic head values according to the head boundary conditions on the top surface boundary and given roller-boundary conditions.

The transient top boundary conditions used were produced by ice-sheet modelling carried out at the University of Edinburgh. Output data from this model consisted of ice thickness and hydraulic head due to ice melting during a cycle of glacial advance and retreat over the site, about 11 000 years. For the 2-D runs, these data were described along the two sections. Examples of boundary conditions at some specific times are shown in Figure 8-10 and Figure 8-11. Input data were generated for every 5 years.

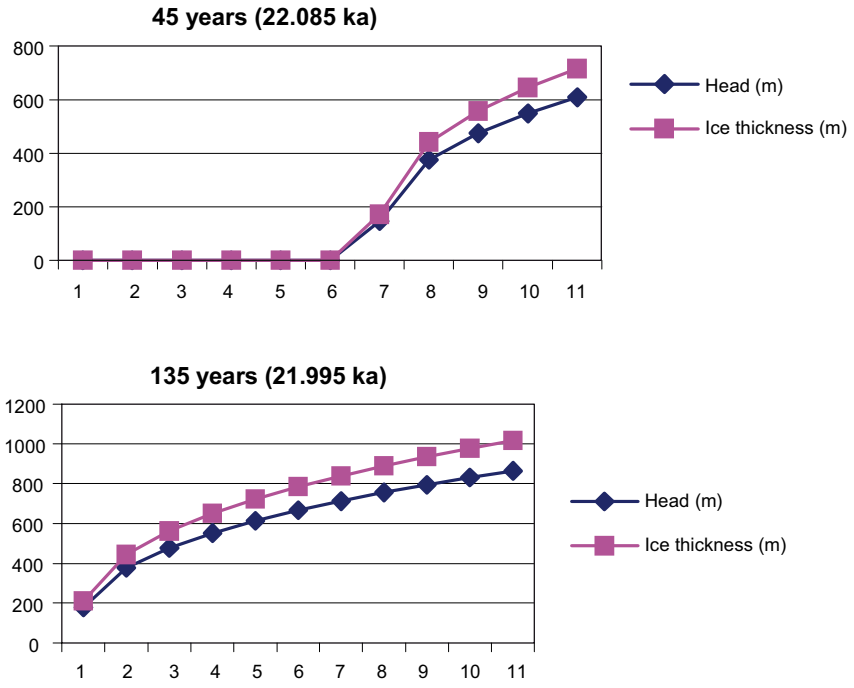

Figure 8-10. *Illustration of ice load and head boundary conditions for the section corresponding to the direction of ice sheet advance at two specific times. Model time zero is 22,130 BP. Distance is shown along the horizontal axis. Each point represents 5 km. /Wallroth et al. 2003/.*

Conceptually the glacial situation was viewed as a load caused by the additional weight of the ice-sheet overburden. Any permafrost was expected to melt when overridden by the ice sheet. A temperate ice sheet was expected to cause a large melt water recharge into the ground. This recharge was allowed to raise the groundwater pressure up to a limit where the groundwater pressure balanced the ice-sheet load. If the groundwater pressure exceeded the ice load the system was assumed to become unstable; forcing the creation of high-preferential flow passages in the form of tunnels along the interface between the ice sheet and the sub-surface (see Figure 8-11).

8.4.2 Rock mass hydraulic and mechanical response

During glaciation the evolution of the resulting hydrostatic head in the subsurface follows the growth and decay of the ice sheet. During ice sheet advance there are horizontal hydraulic gradients all the way to 4 km depth due to the mechanical-hydraulic effect of pore space compression by the ice load. At the time when the ice sheet covers the entire model domain the hydraulic head is high down to about 650 m. The head corresponds to the head boundary

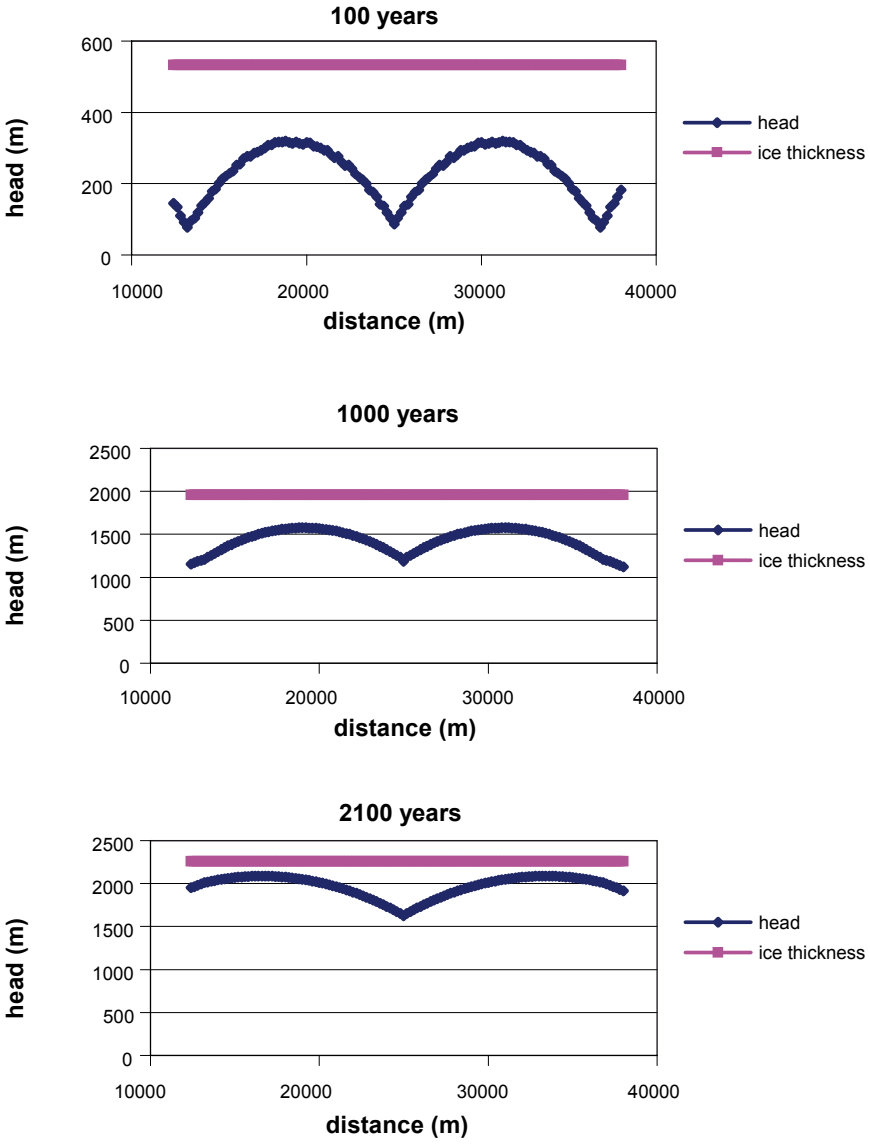

Figure 8-11. *Ice load and head boundary conditions for the transverse section at three specific times. The locations of ice tunnels can be seen in the head profiles. /Wallroth et al. 2003/.*

condition. Below this depth the permeability of the rock mass is much lower, which leads to a very large downward hydraulic gradient in the region of the model just below this depth. Below a depth of about 800–900 m the excess pore pressure built up during the time when the ice covers the site, results from consolidation only and is equivalent to about 1/3 of the ice load.

High subglacial hydraulic heads are rapidly transmitted down fracture zones. Hydraulic heads at repository depth increase rapidly, reaching values > 2,000 m as ice sheet thickness increases to 2,400 m in about 2 000 years. During ice-sheet advance, hydraulic head values in fracture zones can be 400–500 m higher than in the surrounding low permeability rock. Very high downward hydraulic gradients develop in local bedrock areas with large contrasts in permeability as the ice sheet advances across the model domain.

When the ice sheet decays and the mechanical load and hydraulic head decrease a reversal of the vertical hydraulic gradient is observed in the model results. In the permeable fracture zones this phenomenon can be observed for about 100 years, but in the low-permeable rock mass excess pressure remains for tens of thousands of years after the ice sheet has retreated from the studied model domain.

For the transverse section the hydraulic result of the ice tunnels is a flow towards the sinks created by the lower heads given as a top boundary condition.

The downward mechanical displacement of the rock mass follows ice-loading history. From contour plots for the transverse direction, it can be observed that the displacement is larger beneath the tunnels than elsewhere in the model. This is an effect of the higher effective stress due to drainage towards the tunnels and pore pressure reduction.

Plots of the development of rock stresses during the glaciation show that changes in effective stress are much smaller than changes in total stresses due to ice loading. The reason is the counter-balancing effect of load and hydraulic head. There were compressive effective stresses at all times also in the dead-ended fracture (see Figure 8-9). /Chan and Stanchell 2005/ reported, however, that during the rapid retreat of the ice sheet a large drop in the minimum effective stress occurred in the repository region (see Figure 8-12). This was explained as resulting from an almost instantaneous decrease in mechanical stress when the ice sheet disappears from the model domain, whereas the pore pressure dissipates very slowly through the low-permeable rock. The stress drop in Figure 8-12 relates to the effective stress in the intact porous rock, not the effective fracture normal stress, and is not directly applicable for estimating the risks of hydraulic shearing or hydraulic jacking.

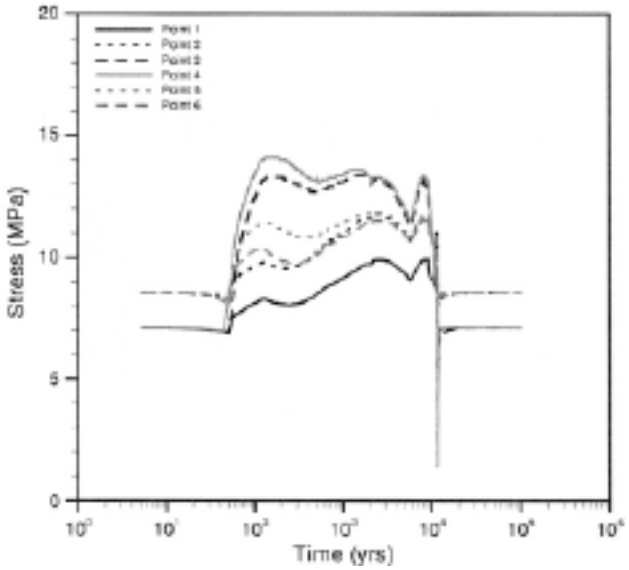

Figure 8-12. *Minimum principal stress development during glacial advance and retreat for six different points in the model, Configuration 6. /Chan and Stanchell 2005/.*

8.4.3 Conclusions about H-M effects

A number of conclusions concerning the hydro-mechanical couplings were drawn from the modelling exercises /Chan et al. 2005ab/:

- Neither of the two groundwater flow models used permits account to be taken of effective stress-dependent permeability. This limitation is likely to have had an impact on the hydraulic results.
- The potential occurrence of tensile failures was investigated in the site-scale H-M models by studying the evolution of the minimum effective stress for selected points. There was a significant compressive effective vertical stress in the horizontal fracture at about 500 m depth during the entire glacial cycle, i.e. no hydraulic jacking occurred. Due to the gentle slope of the ice sheet profile before the ice sheet reaches the bedrock surface directly above the disconnected end of the horizontal fracture zone, the increase in pore pressure (hydraulic head) in the horizontal fracture zone is too small to reduce the vertical effective stress to zero. Once the ice sheet over-rides the disconnected end of the horizontal fracture zone, the increase in vertical effective stress due to the mechanical loading of the ice generally exceeds the reduction due to the excess pore pressure.
- The model simulations have not included the possibility of reactivating deformation zones, so-called end-glacial faulting, during glacial retreat. However, the simulations have indicated residual, high groundwater pressures that may reactivate weak deformation zones near ground surface while trying to escape to the surface after deglaciation. Such excess pressures are likely to help to trigger reactivation of faults.
- Comparisons were made of coupled and uncoupled analyses. A purely mechanical analysis yields larger displacements and spatial and temporal stress variations qualitatively different from a coupled analysis. Without the counter-balancing effect of pore pressure, a mechanical stress analysis of glacial loading predicts the maximum/minimum principal stress ratio to be much closer to 1, which leads to a higher factor of safety, than the coupled H-M analysis.
- The isostatic movements of the Earth's crust due to glacial loading and unloading are primarily controlled by the viscous behaviour of the asthenosphere. The lithosphere (crust and upper mantle) can, in principle, be regarded as an elastic layer. Because of the high viscosity of the asthenosphere a large period of time is required before equilibrium is reached after loading or unloading by the ice sheet. In the site-scale H-M models, the bottom boundary at 4 km depth is rigid and the depression of the model domain caused by the ice load is solely a result of elastic compression of the 4 km thick rock mass. Large-scale changes in the state of stress induced by the ice sheet advance and retreat across the area are, therefore, not included in the results produced by the site-scale models. Even though this omission may not be crucial for the mechanical conditions at repository depth, it has definitely a great impact on the large-scale stability of the Earth crust. Whereas changes in vertical stress are almost all a consequence of the instantaneous application of the ice sheet load, changes in the horizontal stresses are primarily a function of the viscoelastic response of the mantle.
- The potential for hydraulic shearing was studied by assuming that the rock strength can be described by a Mohr-Coulomb failure criterion. The cohesion and friction angle were given different values for rock mass and fracture zone, respectively. In ABAQUS the Mohr-Coulomb criterion is always isotropic which means by necessity that the finite elements in the fracture zones can reach failure conditions for any plane with a critical ratio of shear to normal stress. To avoid this (and associated large strains and pore pressure changes) most analyses were made with purely elastic material models, excluding the plasticity option. By post-processing it was, however, possible to investigate for the specified fracture zones if the calculated effective stress tensor results in failure conditions according to the Mohr-Coulomb criterion /Vidstrand et al. 2003/. The factor of safety, calculated as the ratio of shear strength and shear stress for a total friction angle of 35°, was at all times during the glaciation period above 1.3 at the points where stress histories were studied. However, since the fracture zones were horizontal or dipping at 45°, the most critical planes with respect to shearing (see Section 8.3.2) were not included in the study.

8.5 Summary

Potential hydro-mechanical effects during glaciation include pore pressure increase and groundwater flow due to compaction, permeability changes due to the combined effect of load and fluid pressure, and hydraulically induced shear and tensile failures.

The modelling performed in the DECOVALEX benchmark test has illustrated the importance of flow due to pore-space compression by the ice sheet. However, the results are strongly dependent on the assigned permeability distribution versus depth. For a rock mass with relatively high permeability the hydraulic subsurface head created will depend on the top boundary hydraulic condition more than on the ice load. Furthermore, the flow caused by compression would be reduced if the permeability is described as depending on effective stresses.

One interesting observation in the model results was the residual excess pore pressures in the low-permeable parts of the rock mass after the ice sheet has retreated from the model domain area. This may be of importance for reactivation of faults.

The attempt in the DECOVALEX project to simulate a situation which promotes the development of hydraulic jacking was not successful. The increase in hydraulic head in the horizontal fracture extending beyond the edge of the ice sheet was not sufficiently large to overcome the vertical stress. Analytical calculations, as well as field observations, show, however, that there is a risk for hydraulic jacking at least to some tens of metres beneath the ground surface. Hydraulic jacking initiation, as well as the resulting transient effect in terms of enhanced fracture transmissivity, is of interest to study in order to create an increased understanding of glacial H-M effects.

The DECOVALEX modelling did not indicate any induced hydraulic shearing at the points where stress histories were studied. However, the orientations of fracture zones were not the most critical with respect to the stress directions. The modelling results as well as results from analytical calculations show that some hydraulic shearing is likely to occur during the sequence of advance and retreat of a melting ice sheet. However, it is not necessarily the case that such small-scale failures have any significant impact on the overall hydraulic conditions. Since the effective normal stresses across the fractures under glacial conditions are rather high when shear failures are induced shear dilation is likely to be of relatively small magnitude.

9 Conclusions and discussion

9.1 General

The two main issues addressed in the previous chapters are:

- The extent to which mechanical processes will change the hydraulic conditions in the geosphere;
- The possibility of stress-induced failures in the walls of deposition holes.

The issue of the hydraulic impact is relevant all times and at many scales. There are two concerns: Formation of an EDZ around the periphery of deposition tunnels, and changes in fracture transmissivity.

The issue of stress-induced failures around deposition holes is relevant during the construction and operational phase and during the first years of the heated phase.

The above issues have been addressed as described in the previous chapters in different ways.

- A set of numerical near-field 3DEC models was analyzed to find the mechanical response of the near-field rock to excavation of tunnels and deposition holes, development of swelling pressure in the deposition holes, restoration of the fracture pore pressure, thermal load and glacial load cycles. The model input was derived from the Forsmark, Simpevarp and Laxemar site-descriptive models, from general and site-specific layout descriptions and from results of ABAQUS ice-crust-mantle analyses. The 3DEC model output focused on here relates to stresses in the walls of deposition holes and deformations of near-field fractures.
- Large-scale transmissivity aspects were addressed using results from large-scale 3DEC models, from ABAQUS ice-crust-mantle analyses and from application of analytical expressions.

9.2 Near-field hydraulic conditions

9.2.1 EDZ

The width and the hydraulic properties of the EDZ are determined by the type of disturbance or damage done to the tunnel walls during excavation and depend on the excavation method. Effects of subsequent loading on the EDZ can be estimated to be small compared with the effects of the transition from undisturbed pre-mining conditions to the conditions immediately after excavation, i.e. the combined effects of excavation-induced stress redistribution and excavation damage.

For handling of the permeability aspects of the EDZ in the safety assessment, the following cases should be considered:

- Tunnels are excavated with the intent of limiting the EDZ, i.e. using the drill and blast techniques and the QA procedures described in /Olsson et al. 2004/. In this case, the EDZ is likely to be limited in spatial extent and discontinuous. The axial permeability may increase by half an order of magnitude in a zone of 0.3 m radial thickness. There will be 0.5 m breaks of undamaged rock between each blast round, due to uneven charge distribution in the blast design. However, in the flow modeling, the EDZ is cautiously assumed to be continuous, but of low permeability.

- A limiting case is to assume conventional drill-and-blast of the tunnel, without applying any special QA procedures for controlling the EDZ and without account of discontinuities between blast rounds. The permeability increases by two orders of magnitude in a region corresponding to the zone of damage found in the ZEDEX experiment, i.e. 0.3 m in the roof and walls and 0.8 m in the floor.

Compared with the differences in properties between the two possibilities, the impact of site differences can be ignored.

9.2.2 Near-field fracture transmissivities

General

The disturbance done to the near-field fracture system by the load sequence considered here gives some increase of the transmissivity of near-field fractures. The disturbances leading to transmissivity increases are:

- reductions of fracture normal stresses and
- fracture shear displacements.

For normal stress reductions, there are a number of quantitative relations that all give reasonably similar transmissivity results, as described in Chapter 2. For the effects of shear displacements, the fracture roughness and the fracture normal stress will be important and the uncertainties are greater.

Effects of normal stress variations

The majority of the fracture contact points that were monitored in the 3DEC near-field models were in increased compression throughout the analysis (cf Figure 5-1 through Figure 5-5). Because of the nature of the stress-transmissivity coupling, cf Chapter 2, the transmissivity results are significantly more sensitive to normal stress reductions than to stress increases. This explains why there are increased transmissivities rather than reduced ones.

The increases caused by normal stress reductions are modest for all fractures intersecting a deposition hole below 1.5 m under the tunnel floor. For these fractures, transmissivity increases were limited to small portions of the fracture planes. The maximum increase, a factor of about 25, was found in the low-stress Simpevarp Domain II model (Figure 5-4). In the Forsmark model, transmissivity increases were smaller (Figure 5-1 through Figure 5-3).

For fractures that are parallel with the tunnel floor or the tunnel walls, transmissivity effects are larger and more systematic. At distances smaller than 1.5 m from the periphery the fracture normal stresses may be sufficiently low that the transmissivity should be cautiously assumed to increase by two orders of magnitude.

Effects of shear displacements

For transmissivity effects of shear displacements there are uncertainties:

- The slip-transmissivity relation is uncertain. It was observed that the largest slip was on the order of 5 mm, and that this displacement can be estimated to increase the transmissivity by a factor of about 20, using findings from lab-scale experiments on *Ävrö granite* fractures (Figure 2-8). It was also observed that the laboratory-scale experiment was conducted at smaller normal stresses than those found for that particular fracture in the model, and that this indicates that the increase in transmissivity estimate is too large.
- The fracture geometry did not include fractures of larger extension than a few tens of metres. Larger fractures that intersect the near-field would slip more. Using the results in /Hakami and Olofsson 2002/, thermally driven fracture shear displacements along fractures of 250 m diameter can be estimated to be about 30–40 mm, if the fracture dips about 30°.

That displacement would take place under much higher normal stresses than those typically applied in laboratory-scale experiments such as the ones performed by /Olsson 1998/. The normal stress would be at least 20 MPa, i.e. 5 times higher than the largest stress applied in Olsson's experiment. The effects on the transmissivity would consequently be modest, certainly much less than the two-order-of magnitude increase found in the experiment. In the immediate surroundings of the openings where normal stresses may be low locally, i.e. in the grey-shaded regions shown in Figure 5-8, the increase should be higher.

Summary

The transmissivity changes suggested in Figure 5-8 were defined to account for as many of the results from the different 3DEC models as possible and to allow for expedient and simple handling in hydrological models. The two-order of magnitude increase is probably an over-estimate: none of the monitored individual results (contact point stress relaxation or slip) indicated larger transmissivity increases.

The suggestions in Figure 5-8 apply for the construction and operational phases and for the initial temperate period. The probably apply also for the glacial cycle, although this may have to be checked when results from more realistic ice-crust-mantle analyses are at hand.

9.3 Far-field fracture transmissivities

9.3.1 Construction and operational phase

During the construction and operational phase, there are no effects on fractures other than those in the near-field.

9.3.2 Temperate phase

Effects of normal stress variations

The results of the large–scale 3DEC thermo-mechanical models confirm the statements made in SR-97, i.e. that increases in the transmissivity of steeply dipping fractures will be found below the ground surface as a result of the thermal pulse, but that this region will not extend deeper than about two hundred metres.

- At depths smaller than 50–100 m, horizontal stresses will be zero or close to zero, meaning that transmissivity effects are potentially significant, but difficult to quantify.
- Between 100 m and 200 m depth there will be modest increases in transmissivity. The maximum increase found here corresponds to a factor of four in the upper part of this region (worst case strike; conservative stress-transmissivity relation, cf Figure 7-10).
- About 150 m above and below the repository horizon, horizontal stresses will be increased throughout the entire thermal period. This will give transmissivity reductions. However, because of the nature of stress-transmissivity relations for fractures in high compression these reductions are just a few percent.

Effects of shear displacements

The thermal load will generate shear displacements along large fractures, some of which may intersect the near-field. Fractures with dip angles of around 30 degrees will have the largest shear-to-normal stress ratios and move most. /Hakami and Olofsson 2002/ calculated thermally induced slip magnitudes in large-scale 2-D UDEC models. If their results are translated to 3-D, a fracture with 400 m diameter and a friction angle of 30° would slip by 30–40 mm at maximum (at the centre of the fracture after 200 years). Using large-scale thermo-mechanical 3DEC models, /Hakami et al. 1998/ estimated the maximum thermally induced shear displacements

of large fracture zones to be about 20 mm. Both analyses overestimated the heat load compared to the layout being considered now.

Irrespective of the fracture dip and size, thermally induced slip movements will take place under normal stresses that are, in general, significantly higher than those typically applied in lab-scale hydro-mechanical shear tests, for instance in those reported by /Olsson 1998/. For fractures in 4 MPa of compression, Olsson reported that transmissivities increased by a factor of about 20 (approximately) after about 5 mm of shear displacement and between 50 and 100 after 15 mm of shear displacement (Figure 2-8). For experiments carried out at 2 MPa of normal stress, corresponding transmissivities increased more and earlier. Considering that the effective normal stress in repository host rock will be at least 20 MPa for fractures with dip angles around 30 degrees, there is no reason to assume that thermally induced fracture shear displacements will give more than modest changes in transmissivity. For fractures that intersect the near-field just below the tunnel floor and just above the tunnel roof, normal stresses may be smaller, meaning that the transmissivities may increase locally in these regions (cf Chapter 5).

Summary

In summary, the regions of increased transmissivities suggested for near-field fractures (Figure 5-8) are estimated to be valid also for large fractures that intersect the near-field. The major uncertainty is in the conceptual understanding of transmissivity effects of shear displacement under high normal stresses. Here it has been estimated that dilation will be sufficiently suppressed and gouge production sufficiently promoted that there will be only insignificant transmissivity effects.

9.3.3 Glacial load

Effects of normal stress variations outside the ice margin

Around the margin of the ice and outside the margin there will be reductions in horizontal stresses after the retreat of the ice (cf Figure 7-11). For the ice load assumptions made here that stress reduction amounted to about 4 MPa at maximum.

- Depending on the initial, present-day stresses the 4 MPa stress reduction may give low or zero horizontal stresses in a 100-m thick region below the ground surface (cf Figure 7-12). Transmissivity increases for steeply dipping fractures will be considerable in this region, but are difficult to quantify.
- At depths between 200 m and 1,000 m, transmissivities may increase by factors ranging between 2 and 4 at maximum in Laxemar, and practically not at all in Forsmark.

The above illustrates the difference between the Forsmark and the Laxemar /Simpevarp sites. Because of the low initial Laxemar stresses, the transmissivity conditions in Laxemar are sensitive to horizontal stress variations. If the stress reduction outside the ice margin is larger than the present-day effective stress on steeply dipping fractures, the Laxemar site would see very significant transmissivity increases also down to the depth of the repository.

There is also the theoretical possibility of excess pore pressures outside the margins of the ice, i.e. pore pressures appearing without any corresponding ice overburden. If that pore pressure is larger than the mechanical stress, the effective normal stress may approach zero, giving hydraulic jacking (cf Chapter 8). A necessary condition for hydraulic jacking to occur is that high pore pressures can be transmitted horizontally without significant losses over long distances, i.e. from regions under direct mechanical load to regions without load. At shallow depths, e.g. some tens of metres, where the excess pore pressure needed to produce jacking is low, less than 1 MPa, jacking is theoretically possible and has also been observed in the field. For jacking to occur at depths of about 100 m, extreme connectivity and transmissivity conditions would be required. In the DECOVALEX simulations, it was not possible to produce any hydraulic jacking at repository depth.

Effects of normal stress variations under the ice

If there are only mechanical ice load effects, i.e. no increased pore pressures, all normal stresses increase under the ice cover, giving reduced transmissivities on all fractures.

There is, however, a possibility that there will be high pore pressures under the ice, approximately equal to the ice overburden pressure. Horizontal and subhorizontal fractures will experience only minor changes in effective stress and transmissivity. For steeply dipping fractures the horizontal stress additions will determine whether the effective stresses will increase or decrease. For the ice-stress models pictured in Figure 4-12, the horizontal stress additions are smaller than the ice overburden pressure and therefore smaller than the potential excess pore pressure. This will give transmissivity increases. For Forsmark, the consequences would be significant down to a depth of a little more little more than 200 m with large and uncertain transmissivity increases (Figure 8-2). Below 300 m depth the effects would be small. For Laxemar, the effects would be significant at much larger depths.

Ice stress model

The horizontal stress additions outside the ice margin (e.g. in the forebulge region) as well as below the ice are obviously important to the hydraulic conditions between the ground surface and the repository, in particular for Laxemar. The potential problems are that horizontal stress additions under the ice (increased compression) may be too small to balance the excess pore pressure, or too large in the forebulge region (reduced compression) in comparison to the present-day effective horizontal stress. The ice-stress models pictured in Figure 4-10 and Figure 4-12 are, however, all very schematic and based on oversimplified ice-crust-mantle analyses. Preliminary results from new and improved models analyzed with account of the crust compressibility and with realistic stiffness/depth relations /Lund 2006/ suggest that the above potential problems may not be important. The horizontal stress additions under the ice seem to be similar to, or just marginally smaller than, the ice overburden pressure, whereas the stress reductions in the forebulge region seem to be approximately those assumed here (cf Figure 7-11).

Effects of shear displacements

The potential for fracture slip can be assumed to be at maximum during the period when the retreating ice margin passes (cf Chapter 4). This is probably true irrespective of possible nuances in the ice-stress model. The slip magnitude estimates shown in Figure 8-8 (upper), i.e. about 15 mm for 400 m diameter fractures dipping about 30° in the direction of the major horizontal stress, are probably realistic. Similar to the thermally induced large-scale shear displacements, the fracture normal stress will be 4 or 5 times higher than the stress typically applied in hydro-mechanical laboratory-scale shear box tests (cf Figure 2-8). In the immediate surroundings of the repository openings, normal stresses may be low locally, which means that dilation, rather than aspenity damage and gouge production, is likely to determine the effects of shear on fracture transmissivity. This may give transmissivity increases of perhaps two orders of magnitude. Elsewhere, the high normal stress will suppress dilation and promote gouge production, giving much smaller transmissivity increases.

Summary

As of now, the results from the improved ice-crust-mantle models are not verified. The best estimate would be to assume that there will not be any transmissivity effects under the ice, and that the transmissivity effects in the forebulge region will be approximately those pictured in Figure 7-12. This means significant effects above 100 m depth for both Forsmark and Laxemar, no effects below that depth at Forsmark and transmissivities increased by a factor of about 3 at Laxemar.

Note that the same "worst case forebulge stresses" have been added to the stresses at the different sites schematically, without account of the different distances from the NW ice edge (cf Figure 7-11*)*.

In summary, the regions of increased transmissivities suggested for near-field fractures (Figure 5-8) are estimated to be valid also for large fractures that intersect the near-field. A possible exception may occur at Laxemar, where steeply dipping fractures striking in the major stress direction may lose some compression in a forebulge type of stress state. Transmissivities may increase by a factor of 3 for these fractures.

Apart from the general and important uncertainty in the ice stress model, the major uncertainty is in the conceptual understanding of transmissivity effects of shear displacement under high normal stresses. Here it has been estimated that dilation will be sufficiently suppressed and gouge production sufficiently promoted that there will be only insignificant transmissivity effects.

9.4 Extent of spalling

The results obtained from the 3DEC near-field models suggest that there will not be any spalling in the construction and operational phase at any of the sites other than Laxemar, provided that the spalling strength is 55% of the uniaxial compressive strength as suggested by preliminary evaluations of the APSE field test and in recent work on stability of underground openings at the different sites /Martin 2005/. There will be thermally induced spalling at all sites, possibly with exception of the low-stress Simpevarp stress Domain II subarea. Because of the sensitivity to uniaxial compression strength variations about the mean and to spalling strength assumptions, the uncertainties are, however, great as demonstrated in Table 6-3. In reality, the uncertainties are even greater:

- All models were analyzed using mean values of rock mass elastic property parameters, rock mass thermal volume expansion coefficients and initial stresses. In the site descriptions, there are uncertainties in these values. In addition, because of the tunnel EDZ, there will be a stress-relaxed zone under the tunnel floor.
- The spalling estimates were based on results of elastic models, i.e. without any disturbance of slipping fractures. Ignoring fracture slip does not mean that the spalling risk is systematically over- or under-estimated. Slipping fractures will cause stress relaxation in parts of the periphery of a deposition hole and increased stresses in other parts (cf Figure 6-1 through Figure 6-4).

Uncertainties in elastic properties are probably less important than initial stress uncertainties. These parameters (and the volume expansion coefficient) are not important to the stress in the construction and operational phase, only in the thermal phase. The uncertainty of the mean deformation modulus is less than 7% for the rock mass and even smaller for the intact rock /SKB 2005ab/. For the volume expansion coefficients, there are only small variations between the mean values of the different rock types, which may indicate that uncertainties in the mean values are small.

Stress magnitude uncertainties are potentially important as illustrated by the update of the minor horizontal stress in Forsmark (from 18 MPa to 35 MPa at 500 m depth, cf text under Table 4-1). The spalling risk does, however, not seem to be much affected by this particular change in the in situ stress description (cf text under Table 6-3).

The orientation of the major horizontal stress is obviously important. If the Forsmark and Simpevarp (I) in situ major stress tended to be more perpendicular to the tunnel axis, the stresses around the deposition holes would look different from those found in the 3DEC models analyzed here (with 15° between tunnel axis and major stress). The Simpevarp (I) initial stresses and the Laxemar initial stresses are approximately equal in magnitude, but (for the layouts

considered here) differently oriented in relation to the tunnels. Consequently, the maximum tangential stresses were higher in the Laxemar model (with the major in situ stress almost perpendicular to the tunnel cf Table 4-1). This is the reason why the Laxemar model results indicated spalling directly after excavation (as opposed to the results from the other models, cf Table 6-3). The Forsmark site description gives a 50° scatter of the stress orientation, which may mean that the angle between the tunnel axis and the major stress could be about 45°. This indicates that spalling may take place directly after excavation also at Forsmark (even if stress magnitudes and the spalling strength take on their reference (mean) values).

For spalling risk estimates, stress results from elastic models without explicit representation of fractures are probably relevant approximations. For the two points at deposition hole mid-height monitored in the Forsmark models, slipping fractures reduced the maximum stress by between 0% and 5% and by between 10% and 15%, respectively, depending on friction. For the monitored points 1 m below the tunnel floor, there were reductions (between 10% and 15%) as well increases (upwards of 50%). However, small regions of structurally controlled stress concentrations should not be considered relevant for spalling risk estimates, meaning that the elastic approximations should be sufficient.

The 3DEC models, with thermo-elastic representation of the continuum between fractures, can only predict the extent of the regions in which the nominal spalling strength may be exceeded. The true extent and shape of the failed regions, however, cannot be assessed by use of 3DEC models, or any other model that cannot explicitly represent brittle failure. For now, estimates must be based on empirical findings, for instance from the APSE experiment. These results indicate that the spalled zone, about 0.07 m deep and about 0.8 m in lateral extension, will extend vertically with increasing thermo-mechanical load, but not change in shape otherwise. The EDZ was not represented in the 3DEC models, but the APSE experience (and the heated failure test at AECL's URL /Martino and Read 1995/) implies that the stress-relaxed EDZ below the tunnel floor is likely to prevent spalling in the uppermost 0.5 m of the deposition holes.

In conclusion, without the support of any bentonite swelling pressure, it seems to be almost certain that there will be spalling after some time of heating at all sites, possibly with the exception of the low-stress Simpevarp II domain.

There is a possibility that pressures much smaller than the fully developed bentonite swelling pressure may be sufficient to suppress spalling /Cho et al. 2002/. This is also supported by a preliminary evaluation of the Äspö pillar stability experiment /Andersson and Eng 2005/. Filling the buffer-rock clearance with bentonite pellets at the time of deposition would give such a small pressure. Even if that pressure were not sufficient to prevent initiation of brittle failures altogether, it would help stabilize the walls and limit the growth of failures. The backfill material applied on top of the bentonite blocks at 1 m depth and up to the tunnel floor will probably interact mechanically with the rock walls more efficiently directly after deposition than the pellet filling in the gap between bentonite blocks and rock below 1 m. Together with the EDZ stress relaxation effects this will contribute to prevent thermally induced spalling in the upper parts of the deposition holes. This means that there is a good likelihood that spalling will be found only at depths larger than about 1 m.

10 References

Ageskog L, Jansson P, 1999. Heat propagation in and around the deep repository. Thermal calculations applied to three hypothetical sites: Aberg, Beberg and Ceberg. SKB TR-99-02. Svensk Kärnbränslehantering AB.

Andersson C, Eng A, 2005. Äspö Pillar Stability Experiment. Final experiment design, Monitored data and observations. SKB R-05-02. Svensk Kärnbränslehantering AB.

Bandis S, 1980. Experimental studies of scale effects on shear strength and deformation of rock joints. Ph. D. Thesis. Dept. of Earth Sciences, University of Leeds.

Bandis S, Lumsden A, Barton N, 1983. Fundamentals of rock joint deformation. Int. J. Rock Mech. Min. Sci. and Geomech. Abstr. 20: 244–268.

Barton N, Choubey V, 1977. The shear strength of rock joints in theory and practice. Rock Mechanics, 10. pp. 1–54.

Barton N, 1982. Modelling rock joint behaviour from in situ block tests: Implications for nuclear waste repository design. Technical Report ONWI-308, Office of Nuclear Waste Isolation, Columbus, Ohio.

Boulton G S, Caban P E, van Gijssel K, 1995. Groundwater flow beneath ice sheets: part 1 – large scale patterns. Q. Sci. Rev. 14: 545–562.

Boulton G S, Caban P, 1995. Groundwater flow beneath ice sheets: part II – its impact on glacier tectonic structures and moraine formation. Q. Sci. Rev. 14: 563–587.

Brantberger M, Zetterqvist A, Arnbjerg-Nielsen T, Olsson T, Outters N, Syrjärnen P, 2006. Final repository for spent nuclear fuel – Underground design Forsmark, Layout D1. SKB R-06-34. Svensk Kärnbränslehantering AB.

Bäckblom G, Munier R, 2002. Effects of earthquakes on the deep repository for spent nuclear fuel in Sweden based on case studies and preliminary model results. SKB TR-02-24. Svensk Kärnbränslehantering AB.

Bäckblom G, Christiansson R, Lagerstedt L, 2004. Choice of rock excavation methods for the Swedish deep repository for spent nuclear fuel. SKB R-04-62. Svensk Kärnbränslehantering AB.

Case J B, Kelsall P C, 1987. Modification of rock mass permeability in the zone surrounding a shaft in welded tuff. Nevada Nuclear Waste Storage Investigation Project. Contractor Report SAND86 7001.

Chan T, Stanchell F W, 2005. Subsurface hydro-mechanical (HM) impacts of glaciation: Sensitivity to transient analysis, HM coupling, fracture zone connectivity and model dimensionality. Int. J. Rock Mech. Min. Sci., 42, 828–849.

Chan T, Christiansson R, Boulton GS, Ericsson LO, Hartikainen J, Jensen MR, Mas Ivars D, Stanchell FW, Vidstrand P, Wallroth T, 2005a. DECOVALEX III BMT 3/BENCHPAR WP4. Report of BMT3/WP4 – The thermo-hydro-mechanical responses to a glacial cycle and their potential implications for deep geological disposal of nuclear fuel waste in a fractured crystalline rock mass. SKI Report 2005:28.

Chan T, Christiansson R, Boulton GS, Ericsson LO, Hartikainen J, Jensen MR, Mas Ivars D, Stanchell FW, Vidstrand P, Wallroth T, 2005b. DECOVALEX III BMT 3/BENCHPAR WP4: The thermo-hydro-mechanical responses to a glacial cycle and their potential implications for deep geological disposal of nuclear fuel waste in a fractured crystalline rock mass. Int. J. Rock Mech. Min. Sci., 42, 805–827.

Cho N, Martin C D, Christiansson R, 2002. Suppressing fracture growth around underground openings. In Proc. 5th North American Rock Mechanics Symposium and 17th Tunnelling Association of Canada Conference NARMS/TAC 2002, Toronto (Ed. R. Hammah, W. Baden, J. Curran, M Telesnicki), vol. 2, pp 1151–1158, University of Toronto Press.

Claesson J, Probert T, 1996. Thermoelastic stress due to a rectangular heat source in a semi-infinite medium. SKB TR 96-13. Svensk Kärnbränslehantering AB.

Dershowitz W, Wallman O, Kindred S, 1991. Discrete Fracture Modelling for the Stripa Site Characterization and Validation Drift Inflow Predictions. Stripa Project Technical Report 91–16, SKB. Svensk Kärnbränslehantering AB.

EC, 2004. European Commision, CLUSTER EDZ, Impact of the Excavation Disturbed Zone on the performance of radioactive waste geological repositories. Proceedings of an EC CLUSTER Conference and Workshop, Luxembourg, Nuclear Science and Technology, EUR 2108 EN, in preparation.

Emsley S, Olsson O, Stenberg L, Alheid H-J, Falls S, 1997. ZEDEX-A study of damage and disturbance from tunnel excavation by blasting and tunnel boring. SKB TR-97-30. Svensk Kärnbränslehantering AB.

Fälth B, Hökmark H, 2006a. Seismically induced slip on rock fractures. Results from dynamic discrete fracture modeling. SKB R-06-48. Svensk Kärnbränslehantering AB.

Fälth B, Hökmark H, 2006b. Mechanical and thermo-mechanical discrete fracture near-field analyses based on preliminary data from the Forsmark, Simpevarp and Laxemar sites. SKB R-06-89. Svensk Kärnbränslehantering AB.

Goodman R, 1976. Methods of geological engineering in discontinuous rock. West, New York,. p. 472.

Guvanasen V, Chan T, 2000. A three-dimensional numerical model for thermo-hydro-mechanical deformation with hysteresis in a fractured rock mass. Int. J. Rock Mech. Mining Sci. 37, 89–106.

Hakami E, Olofsson S-O, Hakami H, Israelsson J, 1998. Global thermo-mechanical effects from a KBS-3 type repository. SKB TR-98-01. Svensk Kärnbränslehantering AB.

Hakami E, Olofsson S-O, 2002. Numerical modelling of fracture displacements due to a thermal load from a KBS-3 repository. SKB TR-02-08. Svensk Kärnbränslehantering AB.

Hansson H, Stephansson O, Shen B, 1995. SITE-94. Far-field Rock Mechanical Modelling for Nuclaer Waste Disposal. SKI Report 95:4, Swedish Nuclear Power Inspectorate.

Hökmark H, 1990. Distinct Element Method Modeling of Fracture Behavior in Near Field Rock. Stripa Project Technical Report 91-01, SKB. Svensk Kärnbränslehantering AB.

Hökmark H, 2003. Canister positioning. Influence of fracture system on deposition hole stability. SKB R-03-19. Svensk Kärnbränslehantering AB.

Hökmark H, Fälth B, 2003. Thermal dimensioning of the deep repository. Influence of canister spacing, rock thermal properties and nearfield design on the maximum canister temperature. SKB TR-03-09. Svensk Kärnbränslehantering AB.

Hökmark H, Claesson J, 2005. Use of an anlytical method for calcuating tempertures in repository host rock. Engineering Geology 81 pp 353–364.

Itasca, 1992. UDEC, Universal Distinct Element Code. Ver 1.8 users manual. Itasca Consultants inc. Minneapolis.

Itasca, 2003. 3DEC, 3-Dimensional Distinct Element Code. Ver 3.0 users manual. Itasca Consultants inc. Minneapolis.

Ikonen K, 2003. Thermal analyses of nuclear fuel repository. Posiva report 2003-04.

Janson T, Magnusson J, Bergvall M, Olsson R, Cuisiat F, Skurtveit E, Grimstad E, 2006. Final repository for spent nuclear fuel – Underground design Laxemar, Layout D1. SKB R-06-36. Svensk Kärnbränslehantering AB.

Jupe A J, Green A S P, Wallroth T, 1992. Induced microseismicity and reservoir growth at the Fjällbacka hot dry rock project. Int. J. Rock Mech. Min. Sci. & Geomech. Abstr., 29, 343–354.

La Pointe P R, Cladouhos T, Follin S, 1999. Calculation of of displacements of fractures intersecting canisters induced by earthquakes: Aberg, Beberg and Ceberg examples. SKB TR-99-03. Svensk Kärnbränslehantering AB.

Lindblom U, 1997. Hydromechanical instability of a crystalline rock mass below a glaciation front. SKB Utveckling Project report U-97-13.

Liu Hui-Hai, Rutqvist J, Zhou Q, Bodvarsson G S, 2003. Upscaling of normal stress-permeability relationships for fracture networks obeying fractional Levy motion. In GeoProc 2003 International Conference on Coupled T-H-M-C processes in Geo-systems: Fundamentals, Modelling, Experiments & Applications. Royal Institute of Technology. Dept. of Water Resources Engineering, Stockholm.

Lund B, 2005. Effects of deglaciation on the crustal stress field and implications for endglacial faulting: A parametric study of simple earth and ice models. SKB TR-05-04. Svensk Kärnbränslehantering AB.

Lund B, 2006. Stress variations during a glacial cycle at 500 m depth in Forsmark and Oskarshamn: Earth model effects. SKB R-report in print. Svensk Kärnbränslehantering AB.

Löfman J, 2005. Simulation of the hydraulic disturbances caused by the decay heat of the repository in Olkiltuoto. Posiva report 2005-07.

Martin D, Kaiser P, McCreath D, 1999. Hoek-Brown parameters for predicting the depth of brittle failure around tunnels. Can. Geotechnical Journal, 36(1):136–151.

Martin D, Christiansson R, Söderhäll J, 2001. Rock stability considerations for siting and constructing a KBS-3 repository. Based on experiences from Äspö HRL, AECL's URL, tunneling and mining. SKB TR-01-38. Svensk Kärnbränslehantering AB.

Martin D, 2005. Preliminary assessment of potential underground stability (wedge and spalling) at Formark, Simpevarp and Laxemar sites. SKB R-05-71. Svensk Kärnbränslehantering AB.

Martino J, Read R, 1995. Mine-By Experiment Phase III –Heated Failure Tests. Technical Progress Report and Summary of Stage3. AECL, Whiteshell Laboratories, Pinnawa, Manitoba.

Munier R, Hökmark H, 2004. Respect distances. Rationale and means of computation. SKB R-04-17. Svensk Kärnbränslehantering AB.

Olsson M, Niklasson B, Wilson L, 2004. Äspö HRL. Experiences of blasting of the TASQ tunnel. SKB R-04-73. Svensk Kärnbränslehantering AB.

Olsson R, 1998. Mechanical and Hydromechanical Behaviour of Hard Rock Joints. A laboratory study. Ph.D. thesis, Chalmers University of Technology, Dept of Geotechnical Engineering, Göteborg.

Patterson W S B, 1994. The Physics of Glaciers. Pergamon Press. Elsevier, Oxford. 480 p.

Pine R J, Batchelor A S, 1984. Downward migration of shearing in jointed rock during hydraulic injections. Int. J. Rock Mech. Min. Sci. & Geomech. Abstr. Vol 21, No. 5, pp 249–263.

Probert T, Claesson J, 1997a. Temperature field due to time dependent heat sources in large rectangular grid. Application for the KBS-3 repository. SKB TR-97-27. Svensk Kärnbränslehantering AB.

Probert T, Claesson J, 1997b. Thermoelastic stress due to a rectangular heat source in a semi-infinite medium. Application for the KBS-3 repository. SKB TR-97-26. Svensk Kärnbränslehantering AB.

Pusch R, 1990. Radionuclide transport paths in the nearfield- a KBS-3 concept study. SKB TR-90-32. Svensk Kärnbränslehantering AB.

Pusch R, Börgesson L, Knutsson S 1990. Origin of silty fracture fillings in crystalline bedrock. Geol. Fören. Stockholm Förh., 112, 209–213.

Pusch R, Stanfors R, 1992. The zone of disturbance around blasted tunnels at depth. Int. J. Rock Mech. Min. Sci. & Geomech. Abstr. Vol 29, No.5 pp 447–456.

Raven K G, Gale J E, 1985. Water flow in natural rock fractures as a function of stress and sample size. Int. J. Rock Mech. Min. Sci. & Geomech. Abstr. Vol 22. pp. 251–261.

Rosengren L, Stephansson O, 1990. Distinct element modelling of the rock mass response to glaciation at Finnsjön, Central Sweden. SKB TR-90-40. Svensk Kärnbränslehantering AB.

Shen B, Stephansson O, 1996. SITE-94. Modelling of Rock Fracture Propagation for Nuclear Waste Disposal. SKI Report 96-18. Swedish Nuclear Power Inspectorate.

SKB, 1999. SR 97. Processes in the repository evolution. SKB TR-99-06. Svensk Kärnbränslehantering AB.

SKB, 2001. First TRUE Stage – Transport of solutes in an interpreted single fracture. Proceedings from the 4th International Seminar Äspö, September 9–11, 2000. SKB TR-01-24. Svensk Kärnbränslehantering AB.

SKB, 2002. Deep repository for spent nuclear fuel. Facility description – Layout E. SKB TR-02-23. Svensk Kärnbränslehantering AB.

SKB, 2004a. Interim main report of the safety assessment SR-Can. SKB TR-04-11. Svensk Kärnbränslehantering AB.

SKB, 2004b. Deep repository. Underground design premises. SKB R-04-60. Svensk Kärnbränslehantering AB.

SKB, 2005a. Preliminary site description. Simpevarp subarea –version 1.2. SKB R-05-08. Svensk Kärnbränslehantering AB.

SKB, 2005b. Preliminary site description. Forsmark area –version 1.2. SKB R-05-18. Svensk Kärnbränslehantering AB.

SKB, 2005c. SR-Can report on external conditions.

SKB, 2006a. Preliminary site description. Laxemar subarea –version 1.2. SKB R-06-10. Svensk Kärnbränslehantering AB.

SKB, 2006b. Final repository for spent nuclear fuel – Underground design Simpevarp, Layout D1. SKB R-06-35. Svensk Kärnbränslehantering AB.

SKB, 2006c. Climate and climate related issues for the safety assessment SR-Can. SKB TR-06-23. Svensk Kärnbränslehantering AB.

SKB, 2006d. Data report for the safety assessment SR-Can. SKB TR-06-25. Svensk Kärnbränslehantering AB.

Stephansson O, Dahlström L-O, Bergström K, Myrvang A, Fjeld O K, Hanssen T H, Särkkä P, Väätäinen A, 1987. Fennoscandian Rock Stress Data Base – FRSDB. Technical Report 1987:06. Div. of Rock Mechanics, Luleå Univ. of Technology.

Sundberg J, Back P-E, Bengtsson A, Ländell M, 2005a. Thermal modelling. Preliminary site description. Simpevarp subarea – version 1.2. SKB R-05-24. Svensk Kärnbränslehantering AB.

Sundberg J, Back P-E, Bengtsson A, Ländell M, 2005b. Thermal modelling. Preliminary site description. Formark area – version 1.2. SKB R-05-31. Svensk Kärnbränslehantering AB.

Talbot CJ, 1999. Ice ages and nuclear waste isolation. Engineering Geology 52, 177–192.

Thunvik B, Braester C, 1980. Hydrothermal conditions around a radioactivewaste repository. SKBF/KBS TR-80-19.

Tsang C-F, Bernier F, Davies C, 2005. Geohydromechanical processes in the Excavation Damaged Zone in crystalline rock, rock salt, and indurated and plastic clays – in the context of radioactive waste disposal. Int. J. Rock Mech. Mining Sci. 42, 109–125.

Vidstrand P, Wallroth T, Ericsson L O, Hernelind J, 2003. Benchpar WP4/Decovalex III BMT III, Phase III. Progress Report. Dept of Geology, Chalmers University of Technology, Publ B511.

Vik G, Barton N, 1988. Stage I Joint Characterization and Stage II Preliminary Prediction using Small Core Samples. Stripa Project Technical Report 88-08, SKB. Svensk Kärnbränslehantering AB.

Wallroth T, 1992. Hydromechanical breakdown of crystalline rock. Ph.D. thesis. Dept of Geology, Chalmers Univ of Techn and Univ of Göteborg, Publ A71, 195 pp.

Wallroth T, Jupe A J, Jones R H, 1996. Characterisation of a fractured reservoir using microearthquakes induced by fluid injections. Marine and Petroleum Geology, 13, 447–455.

Wallroth T, Ericsson L O, Hernelind J, 2003. Benchpar WP4/Decovalex III BMT III, Phase II. Progress Report. Dept of Geology, Chalmers University of Technology, Publ B507.

Winberg A, 1991. The role of the disturbed rock zone in radioactive waste repository safety and performance assessment. A topical discussion and international review. SKB TR-91-25. Svensk Kärnbränslehantering AB.